

REPORT DOCUMENTATION PAGE			1 Form Approved OMB NO. 0704-0188		
<p>The public reporting burden for this collection of information is estimated to average 1 hour per response, including the time for reviewing instructions, searching existing data sources, gathering and maintaining the data needed, and completing and reviewing the collection of information. Send comments regarding this burden estimate or any other aspect of this collection of information, including suggestions for reducing this burden, to Washington Headquarters Services, Directorate for Information Operations and Reports, 1215 Jefferson Davis Highway, Suite 1204, Arlington VA, 22202-4302. Respondents should be aware that notwithstanding any other provision of law, no person shall be subject to any penalty for failing to comply with a collection of information if it does not display a currently valid OMB control number.</p> <p>PLEASE DO NOT RETURN YOUR FORM TO THE ABOVE ADDRESS.</p>					
1. REPORT DATE (DD-MM-YYYY) 21-09-2014		2. REPORT TYPE Ph.D. Dissertation		3. DATES COVERED (From - To) -	
4. TITLE AND SUBTITLE Characterization of HgCdTe and related materials and substrates for third generation infrared detectors			5a. CONTRACT NUMBER W911NF-09-2-0064		
			5b. GRANT NUMBER		
			5c. PROGRAM ELEMENT NUMBER 611102		
6. AUTHORS Jae Jin Kim			5d. PROJECT NUMBER		
			5e. TASK NUMBER		
			5f. WORK UNIT NUMBER		
7. PERFORMING ORGANIZATION NAMES AND ADDRESSES Arizona State University PO Box 876011  Tempe, AZ 85287 -6011			8. PERFORMING ORGANIZATION REPORT NUMBER		
9. SPONSORING/MONITORING AGENCY NAME(S) AND ADDRESS (ES) U.S. Army Research Office P.O. Box 12211 Research Triangle Park, NC 27709-2211			10. SPONSOR/MONITOR'S ACRONYM(S) ARO		
			11. SPONSOR/MONITOR'S REPORT NUMBER(S) 54657-EL.13		
12. DISTRIBUTION AVAILABILITY STATEMENT Approved for public release; distribution is unlimited.					
13. SUPPLEMENTARY NOTES The views, opinions and/or findings contained in this report are those of the author(s) and should not be construed as an official Department of the Army position, policy or decision, unless so designated by other documentation.					
14. ABSTRACT HgCdTe is currently the dominant material for infrared sensing and imaging, and is usually grown on lattice-matched bulk CdZnTe (CZT) substrates. There have been significant recent efforts to identify alternative substrates to CZT as well as alternative detector materials to HgCdTe. In this dissertation research, a wide range of transmission electron microscopy (TEM) imaging and analytical techniques was used in the characterization of epitaxial HgCdTe and related materials and substrates for third generation IR detectors. <del>ZnTe layers grown on Si substrates are considered to be promising candidates for lattice matched large area and</del>					
15. SUBJECT TERMS HgCdTe, infrared detectors, HgCdTe/CdTe/GaAs (211)B, CdTe/GaAs (211)B					
16. SECURITY CLASSIFICATION OF:			17. LIMITATION OF ABSTRACT UU	15. NUMBER OF PAGES	19a. NAME OF RESPONSIBLE PERSON David Smith
a. REPORT UU	b. ABSTRACT UU	c. THIS PAGE UU			19b. TELEPHONE NUMBER 480-965-4540

## Report Title

Characterization of HgCdTe and related materials and substrates for third generation infrared detectors

### ABSTRACT

HgCdTe is currently the dominant material for infrared sensing and imaging, and is usually grown on lattice-matched bulk CdZnTe (CZT) substrates. There have been significant recent efforts to identify alternative substrates to CZT as well as alternative detector materials to HgCdTe. In this dissertation research, a wide range of transmission electron microscopy (TEM) imaging and analytical techniques was used in the characterization of epitaxial HgCdTe and related materials and substrates for third generation IR detectors.

ZnTe layers grown on Si substrates are considered to be promising candidates for lattice-matched, large-area, and low-cost composite substrates for deposition of II-VI and III-V compound semiconductors with lattice constants near 6.1 Å. After optimizing MBE growth conditions including substrate pretreatment prior to film growth, as well as nucleation and growth temperatures, thick ZnTe/Si films with high crystallinity, low defect density, and excellent surface morphology were achieved. Changes in the Zn/Te flux ratio used during growth were also investigated.

Small-probe microanalysis confirmed that a small amount of As was present at the ZnTe/Si interface.

A microstructural study of HgCdTe/CdTe/GaAs (211)B and CdTe/GaAs (211)B heterostructures grown using MBE was carried out. High quality MBE-grown CdTe on GaAs(211)B substrates was demonstrated to be a viable composite substrate platform for HgCdTe growth. In addition, analysis of interfacial misfit dislocations and residual strain showed that the CdTe/GaAs interface was fully relaxed. In the case of HgCdTe/CdTe/GaAs(211)B, thin HgTe buffer layers between HgCdTe and CdTe were also investigated for improving the HgCdTe crystal quality.

A set of ZnTe layers epitaxially grown on GaSb(211)B substrates using MBE was studied using high resolution X-ray diffraction (HRXRD) measurements and TEM characterization in order to investigate conditions for defect-free growth. HRXRD results gave critical thickness estimates between 350 nm and 375 nm, in good agreement with theoretical predictions. Moreover, TEM results confirmed that ZnTe layers with thicknesses of 350 nm had highly coherent interfaces and very low dislocation densities, unlike samples with the thicker ZnTe layers.

CHARACTERIZATION OF HgCdTe AND RELATED MATERIALS AND  
SUBSTRATES FOR THIRD GENERATION INFRARED DETECTORS

by

Jae Jin Kim

A Dissertation Presented in Partial Fulfillment  
of the Requirements for the Degree  
Doctor of Philosophy

Approved November 2012 by the  
Graduate Supervisory Committee:

David J. Smith, Chair  
Martha R. McCartney  
Terry L. Alford  
Peter A. Crozier

ARIZONA STATE UNIVERSITY

December 2012

## ABSTRACT

HgCdTe is currently the dominant material for infrared sensing and imaging, and is usually grown on lattice-matched bulk CdZnTe (CZT) substrates. There have been significant recent efforts to identify alternative substrates to CZT as well as alternative detector materials to HgCdTe. In this dissertation research, a wide range of transmission electron microscopy (TEM) imaging and analytical techniques was used in the characterization of epitaxial HgCdTe and related materials and substrates for third generation IR detectors.

ZnTe layers grown on Si substrates are considered to be promising candidates for lattice-matched, large-area, and low-cost composite substrates for deposition of II-VI and III-V compound semiconductors with lattice constants near  $6.1 \text{ \AA}$ . After optimizing MBE growth conditions including substrate pretreatment prior to film growth, as well as nucleation and growth temperatures, thick ZnTe/Si films with high crystallinity, low defect density, and excellent surface morphology were achieved. Changes in the Zn/Te flux ratio used during growth were also investigated. Small-probe microanalysis confirmed that a small amount of As was present at the ZnTe/Si interface.

A microstructural study of HgCdTe/CdTe/GaAs (211)B and CdTe/GaAs (211)B heterostructures grown using MBE was carried out. High quality MBE-grown CdTe on GaAs(211)B substrates was demonstrated to be a viable composite substrate platform for HgCdTe growth. In addition, analysis of interfacial misfit dislocations and residual strain showed that the CdTe/GaAs interface was fully relaxed. In the case of HgCdTe/CdTe/ GaAs(211)B, thin HgTe

buffer layers between HgCdTe and CdTe were also investigated for improving the HgCdTe crystal quality.

A set of ZnTe layers epitaxially grown on GaSb(211)B substrates using MBE was studied using high resolution X-ray diffraction (HRXRD) measurements and TEM characterization in order to investigate conditions for defect-free growth. HRXRD results gave critical thickness estimates between 350 nm and 375 nm, in good agreement with theoretical predictions. Moreover, TEM results confirmed that ZnTe layers with thicknesses of 350 nm had highly coherent interfaces and very low dislocation densities, unlike samples with the thicker ZnTe layers.

Dedicated to my wife, Mikyung,  
and my sons, Junhyun and Junhwi.

## ACKNOWLEDGMENTS

I would like to thank all people who have helped and inspired me during my doctorate study. Especially, I would like to express my gratitude to my advisor, Regents' Professor David J. Smith, for his continued support, guidance, and encouragement. His expertise and enthusiasm in electron microscopy has motivated me to become 'just' an electron microscopist. His technical and editorial advice was essential to the completion of this dissertation. I am also deeply grateful for Professor Martha R. McCartney for her support and encouragement. It has been a great honor and memorable experience for me to become a member of their TEM group.

I would like to thank Professors Terry L. Alford and Peter A. Crozier for serving on my dissertation committee. And, I would like to express appreciation to Professor Christopher J. Kiely and Dr. Shohei Nakahara at Lehigh University for their kind guidance and friendship.

I am grateful for the opportunity to use facilities in the John M. Cowley Center for High Resolution Electron Microscopy. I thank Mr. Karl Weiss, Dr. Zhenquan Liu, Mr. Grant Baumgardner, Mr. Gordon Tam, Mr. Sisouk Phrasavath, and Mr. Jason Ng for their technical support and useful discussion throughout my research.

I would like to extend my deep appreciation to Dr. Yuanping Chen and Dr. Gregory Brill in U.S. Army Research Laboratory, Dr. Randy Jacobs in Night Vision and Electronic Sensors Directorate, and Professor Tom Myers and

colleagues from Texas State University-San Marcos for their collaboration and providing the samples used for investigation in this dissertation.

Particular thanks to our research group members for their help during my graduate study. I want to thank Dr. David Cullen, Dr. Kai He, Dr. Luying Li, Dr. Lu Ouyang, Dr. Wenfeng Zhao, and Dr. Lin Zhou for their discussion, assistance, and friendship. My best wishes to Michael, Aram, Sahar, Dinghao, Zhaofeng, Desai, Xiaomeng, Jing, Allison, Ajit, and Thomas for success in their degree programs.

Many school friends from Lehigh University and Arizona State University, and many church friends from Provo Korean Ward (UT), Bethlehem Ward (PA), and Corona 1st Ward (AZ) have helped me and my family since I came to the United States. Their support and friendship helped me overcome difficult time and stay on the right path during my graduate study. I am very lucky to have wonderful people around me and my family.

Finally, I would like to express my most sincere appreciation towards my lovely wife, Mikyung, and my precious sons, Junhyun and Junhwi, for their love and encouragement, and their confidence in me. I also owe my parents for their unconditional love throughout my life. My Ph.D. would not have been possible without their support. My appreciation is beyond description.



## TABLE OF CONTENTS

	Page
LIST OF TABLES.....	ix
LIST OF FIGURES .....	x

CHAPTER	Page
1 INTRODUCTION.....	1
1.1 Energy band structure of HgCdTe .....	1
1.2 Material properties of HgCdTe .....	4
1.2.1 Lattice parameter .....	5
1.2.2 Coefficient of thermal expansion.....	6
1.3 Molecular beam epitaxy .....	8
1.4 Substrates for HgCdTe growth.....	9
1.5 Overview of dissertation.....	12
References .....	14
2 EXPERIMENTAL PROCEDURES .....	16
2.1 MBE growth .....	16
2.1.1 MBE growth of ZnTe films on Si substrates .....	18
2.1.2 MBE growth of HgCdTe/CdTe or CdTe grown on GaAs substrates .....	19
2.1.3 MBE growth of ZnTe films on GaSb(211)B substrates...	20
2.2 TEM sample preparation .....	21
2.3 Electron microscopy .....	25

CHAPTER	Page
2.3.1 High resolution transmission electron microscopy .....	25
2.3.2 Scanning transmission electron microscopy and energy- dispersive x-ray spectroscopy .....	27
References .....	31
3 CHARACTERIZATION OF ZnTe/Si COMPOSITE	
SUBSTRATES .....	33
3.1 Introduction.....	33
3.2 Experimental details .....	36
3.3 Results and discussion.....	39
3.3.1 Growth of ZnTe(211)/Si(211).....	39
3.3.2 TEM characterization of ZnTe(211)/Si(211) .....	45
3.3.3 Growth of ZnTe(100)/Si(100).....	57
3.3.4 TEM characterization of ZnTe(100)/Si(100) .....	62
3.4 Conclusions.....	66
References .....	68
4 MICROSTRUCTURAL CHARACTERIZATION OF HgCdTe/CdTe GROWN ON GaAs(211)B SUBSTRATES .....	70
4.1 Introduction.....	70
4.2 Experimental details .....	72
4.3 Results and discussion.....	74
4.3.1 TEM characterization of CdTe/GaAs(211)B .....	74
4.3.2 TEM characterization of HgCdTe/CdTe/GaAs(211)B ....	82

CHAPTER	Page
4.4 Conclusions.....	90
References .....	91
5 CRITICAL THICKNESS STUDY OF ZnTe/GaSb(211)B GROWN BY MOLECULAR BEAM EPITAXY .....	94
5.1 Introduction.....	94
5.2 Experimental details .....	96
5.3 Results and discussion .....	98
5.3.1 Calculations of theoretical thickness .....	98
5.3.2 Critical thickness measurement by HRXRD.....	100
5.3.3 TEM characterization of ZnTe/GaSb(211)B.....	103
5.4 Conclusions.....	108
References .....	110
6 SUMMARY AND FUTURE WORK.....	112
6.1 Summary .....	112
6.2 Future work.....	114
6.2.1 Improvement of MBE-grown HgCdTe and substrates ..	114
6.2.2 MBE growth of HgCdSe and HgSe as alternatives to HgCdTe .....	114
6.2.3 Column-by-column analysis of ZnTe/Si and ZnTe/GaSb interfaces.....	116
References .....	118

## LIST OF TABLES

Table	Page
1.1 Summary of material properties of $\text{Hg}_{1-x}\text{Cd}_x\text{Te}$ ternary alloys.....	4
1.2 Lattice parameter correction factor $B(T)$ in equation (1.4) at various temperatures... ..	6
1.3 Some characteristics of CZT, Si, and GaAs substrates... ..	11
2.1 Detail setup of Allied MultiPrep polishing system used at each stage when lapping diamond film for the first specimen side.....	23
2.2 Detail setup of Allied MultiPrep polishing system at each thickness of diamond lapping film for polishing the second side of CdTe/GaAs and HgCdTe/CdTe/GaAs samples... ..	25
4.1 Lattice constants and coefficients of thermal expansion (CTE) of selected semiconductor materials... ..	71

## LIST OF FIGURES

Figure	Page
1.1	The band gap structure of $\text{Hg}_{1-x}\text{Cd}_x\text{Te}$ near the $\Gamma$ -point for three different values of the forbidden energy gap..... 3
1.2	(a) CTE values for MCT (black circle) and CZT (open circle) as a function of Cd concentration $x$ and Zn concentration $y$ , respectively. (b) The difference of CTE between MCT samples and CZT substrates. .... 8
2.1	Top view of a simple MBE chamber showing the essential growth sources, shutters, beam flux detector, and the reflection-high-energy electron diffraction (RHEED) system used for monitoring surface structure during growth..... 17
2.2	Schematic showing procedures used for TEM specimen preparation. .... 22
2.3	Schematic showing the essential components associated with the scanning transmission electron microscopy technique..... 30
3.1	Energy gap versus lattice parameter for several semiconductor material systems. The shaded region highlights semiconductors that have lattice parameters near $6.1\text{\AA}$ . .... 35
3.2	XRD FWHM (right axis), and dislocation density (left axis), of as-grown ZnTe/Si(211) layers as a function of nucleation temperature between $260^\circ\text{C}$ and $340^\circ\text{C}$ ..... 40
3.3	Nomarski optical micrographs for as-grown ZnTe(211) films on Si (211) substrates for various nucleation temperatures between $260^\circ\text{C}$ and $340^\circ\text{C}$ . .... 41

Figure	Page
3.4	XRD FWHM (right axis) and dislocation density (left axis) of as-grown ZnTe (211)/Si(211) layers as a function of growth temperature in the range 260 °C to 340 °C ..... 42
3.5	Nomarski optical micrographs for as-grown ZnTe(211) films on Si(211) substrates at growth temperatures in the range 260 °C to 360 °C ..... 43
3.6	XRD FWHM (right axis); and dislocation density (left axis); and (b) optical microscopy images, of as-grown ZnTe(211)/Si(211) layers nucleated and grown at 300 °C with different Zn/Te flux ratios of 0.5, 1, and 2..... 45
3.7	Cross-sectional electron micrographs of as-grown ZnTe(211)/Si(211) layers nucleated and grown at 300 °C with different Zn/Te flux ratios; (a) Zn/Te = 0.5 (Te-rich), (b) Zn/Te = 1 (equal Zn and Te fluxes), and (c) & (d) Zn/Te = 2 (Zn-rich)..... 47
3.8	Ball-and-stick model of the Si(211) and Si(311) stepped surfaces and their relationship to the Si(111) bulk lattice..... 48
3.9	High-resolution electron micrographs of: (a) ZnTe(211)/Si(211) interface grown under the Te-rich condition; and (b) sample grown under the condition of equal Zn and Te flux ratio ..... 50
3.10	High-resolution electron micrographs of: (a) ZnTe(211)/Si(211) interface grown under the Te-rich condition; and (b) sample grown under the condition of equal Zn and Te flux ratio ..... 51
3.11	Diffractograms of TEM images in Figures 2.9 (a) and (b), respectively.... 52

Figure	Page
3.12 (a) Enlarged image of Figure 2.9 (a), showing atomic structure at the ZnTe(211)/Si(211) interface region; (b) inverse FFT image displaying $\bar{1}\bar{1}1$ planes and (c) inverse FFT image displaying (111) planes .....	54
3.13 (a) Enlarged image of Figure 2.9 (b), showing atomic structure at the ZnTe(211)/Si(211) interface region; (b) inverse FFT image displaying $\bar{1}\bar{1}1$ planes and (c) inverse FFT image displaying (111) planes .....	55
3.14 (a) HAADF image showing region used for EDXS analysis; (b) elemental profile along line indicated in (a); (c) individual spectra taken in turn at three different positions, as marked with numbers 1, 2, and 3 .....	57
3.15 (a) XRD FWHM; and (b) Nomarski optical micrographs, of as-grown ZnTe(211)/ Si(211) layers nucleated and grown at 300 °C with different pre-nucleation treatments (Zn-, Te-, and no-treatment) .....	60
3.16 (a) XRD FWHM; and (b) Nomarski optical micrographs, of as-grown ZnTe(211)/ Si(211) layers nucleated and grown at 300 °C under with different Zn/Te flux ratios of 0.5, 1, and 2 .....	61
3.17 Cross-sectional electron micrographs of as-grown ZnTe(100)/Si(100) layers nucleated and grown at 300 °C with different Zn/Te flux ratios; (a) & (b) Zn/Te = 0.5 (Te-rich), (c) & (d) Zn/Te = 1 (equal Zn and Te fluxes), and (e) & (f) Zn/Te = 2 (Zn-rich).....	63
3.18 High-resolution electron micrographs of ZnTe(100)/Si(100) interface grown under the Te-rich condition in (a) and (b), one grown under the condition of	

Figure	Page
equal Zn and Te flux ratio in (c) and (d), and one grown under the Zn-rich condition in (e) and (f) .....	65
3.19 (a) HAADF image showing region used for EDXS analysis; (b) elemental profile along line indicated in (a).....	66
4.1 Cross-sectional electron micrographs: (a) entire CdTe layer grown on GaAs(211)B; and (b) region close to CdTe/GaAs(211)B interface. ....	75
4.2 High-resolution electron micrograph of CdTe/GaAs(211)B interface. ....	76
4.3 (a) Digitized lattice image of the CdTe/GaAs(211)B interface: inset shows FFT pattern of image; (b) Inverse FFT image obtained by selecting {111} diffraction spots marked by circles; (c) Inverse FFT image obtained by selecting {111} diffraction spots marked by triangles.....	79
4.4 (a) High-resolution electron micrograph of pit region of the CdTe/GaAs(211)B interface; (b) Inverse FFT image obtained by selecting ( $\bar{1}11$ ) and ( $1\bar{1}\bar{1}$ ) diffraction spots; (c) Inverse FFT image obtained by selecting ( $111$ ) and ( $\bar{1}\bar{1}\bar{1}$ ) diffraction spots.....	80
4.5 (a) High-resolution electron micrograph near the top surface of CdTe layer, and (b) enlargement of CdTe layer from the boxed region indicated in (a). .....	81
4.6 (a) HAADF image showing region used for analysis; (b) EDXS elemental profile along the arrow region indicated in (a); (c) individual spectra taken at CdTe and GaAs. ....	82



Figure	Page
4.7	Cross-sectional electron micrographs showing: (a) whole HgCdTe layer on CdTe; and (b) HgCdTe/CdTe interface..... 83
4.8	Cross-sectional electron micrograph showing microstructure near the top surface of HgCdTe epilayer grown on CdTe/GaAs(211)B composite substrate..... 84
4.9	Cross-sectional electron micrographs showing HgCdTe/CdTe heterostructure..... 86
4.10	Cross-sectional electron micrograph (a) and HAADF image (b), showing thin HgTe buffer layer between HgCdTe and CdTe..... 87
4.11	(a) HAADF image showing region used for EDXS analysis; (b) elemental profile along line indicated in (a); (c) intensity profile along the box indicated in (a)..... 89
5.1	HRXRD $\omega$ - $2\theta$ measurements of ZnTe grown for (a) 100 nm, (b) 350 nm, (c) 375 nm, and (d) 2100 nm.. 100
5.2	FWHM of the $\omega$ - $2\theta$ ZnTe(422) peak at different thicknesses. Inset shows the same plot on a log-log scale.. 101
5.3	Peak separation ( $\Delta\omega$ ) between ZnTe(422) and GaSb(422) $\omega$ - $2\theta$ HRXRD peaks and the measured out-of-plane lattice parameter for ZnTe films of different epilayer thicknesses..... 102
5.4	Low magnification cross-sectional TEM images, (a) and (b), showing highly-separately misfit dislocations at ZnTe/GaSb interface..... 103

Figure	Page
5.5 (a) HREM image establishing the highly coherent nature of the ZnTe/GaSb interface (arrowed); (b) inverse FFT images obtained by selecting pairs of {111} diffraction spots.....	104
5.6 (a) HAADF image showing the region used EDXS analysis, and (b) individual EDXS spectra taken from the ZnTe epilayer and GaSb substrate, respectively.....	105
5.7 Low magnification cross-sectional TEM images for (a) 375 nm and (b) 400 nm ZnTe epilayers on GaSb substrates, respectively. Arrows indicates the thickness of ZnTe layer. ....	107
5.8 Low magnification cross-sectional TEM images for (a) 500 nm and (b) 1,000 nm ZnTe epilayers on GaSb substrates, respectively. ....	108
6.1 Cross-sectional electron micrographs of HgCdSe/ZnTe [(a), (b), and (c)] and HgSe (d).....	116

## Chapter 1

### INTRODUCTION

Mercury cadmium telluride (MCT,  $\text{HgCdTe}$  or  $\text{Hg}_{1-x}\text{Cd}_x\text{Te}$ ) has been a dominant material for infrared (IR) sensing and imaging ever since its synthesis was first reported by the group at the Royal Radar Establishment in Malvern, England.<sup>1</sup> MCT is a pseudo-binary semiconductor alloy with the zincblende crystal structure. Mixed alloys of the two zincblende compounds,  $\text{HgTe}$  and  $\text{CdTe}$ , can cover all important IR ranges from 1 to 30  $\mu\text{m}$ , simply by changing the Cd and Hg ratio. Additionally, the MCT lattice constant varies by only 0.3 % over the entire stoichiometric range of  $\text{Hg}_{1-x}\text{Cd}_x\text{Te}$  from  $x = 0$  to 1. Consequently, it is possible to grow high quality MCT heterostructures for all compositions. Since it was first introduced, MCT has been highly successful as the most widely applicable IR material. This success has been the result of both the unique features of its energy band structure and its technologically favorable material properties. MCT is the third most studied semiconductor after Si and GaAs.<sup>2</sup>

#### 1.1 Energy band structure of $\text{HgCdTe}$

The energy band structure of MCT has three key features that enable it to serve as a nearly ideal IR detector<sup>2</sup>: (i) tailorable energy band gap over the 1–30  $\mu\text{m}$  range; (ii) large optical absorption coefficients that enable high quantum efficiencies; and (iii) favorable inherent recombination mechanisms that lead to

long carrier lifetimes, low thermal generation rates, and high operating temperatures.

Figure 1.1 illustrates the band gap structure of  $\text{Hg}_{1-x}\text{Cd}_x\text{Te}$  as a function of Cd concentration  $x$  at temperatures of 77 K and 300 K.<sup>2</sup> Energy band gap is defined as the difference between the  $\Gamma_6$  and  $\Gamma_8$  band extrema at  $\Gamma = 0$ . CdTe has a normal semiconductor band structure with positive band gap, while HgTe is a negative band gap semiconductor with the conduction band edge ( $\Gamma_6$ ) underneath the valence band edge ( $\Gamma_8$ ).  $\text{Hg}_{1-x}\text{Cd}_x\text{Te}$  alloys of the two fully miscible compounds, HgTe and CdTe, can be produced over the entire composition range. As the Cd concentration  $x$  decreases, the energy band gap of  $\text{Hg}_{1-x}\text{Cd}_x\text{Te}$  alloys narrows from 1.5 eV for CdTe down to -0.26 eV for HgTe. The band gap becomes zero at room temperature when the Cd concentration  $x$  is 0.165 and at 77 K when  $x$  is 0.11, as shown in Figure 1.1.

The most widely used functional form for the temperature-dependent band gap was developed by Hansen *et al.*<sup>4</sup> by fitting a large set of values measured for lower Cd concentration. The band gap in eV is given by:

$$E_g(x, T) = -0.302 + 1.930x + 5.35 \times 10^{-4}T(1 - 2x) - 0.810x^2 + 0.832x^3 \quad (1.1)$$

A supplemental data set with energy band gap for Cd-rich alloys was later added by Laurenti *et al.*<sup>5</sup> The resulting expression for band gap in eV is:

$$E_g(x, T) = -0.303(1 - x) + 1.606x - 0.132x(1 - x) + [6.3(1 - x) - 3.25x - 5.92x(1 - x)] \times 10^{-4}T^2 / (11(1 - x) + 78.7x + T) \quad (1.2)$$

The cutoff wavelength  $\lambda_c(x, T)$ , defined as the wavelength at which the response has dropped to 50 % of its peak value, is shown in Figure 1.1. The energy band gap range available with varying composition of  $\text{Hg}_{1-x}\text{Cd}_x\text{Te}$  enables MCT IR detectors to span an extremely wide range of the IR spectrum including short wavelength IR (SWIR: 1-3  $\mu\text{m}$ ), middle wavelength IR (MWIR: 3-5  $\mu\text{m}$ ), long wavelength IR (LWIR: 8-14  $\mu\text{m}$ ), and very long wavelength (VLWIR: 14-30  $\mu\text{m}$ ).

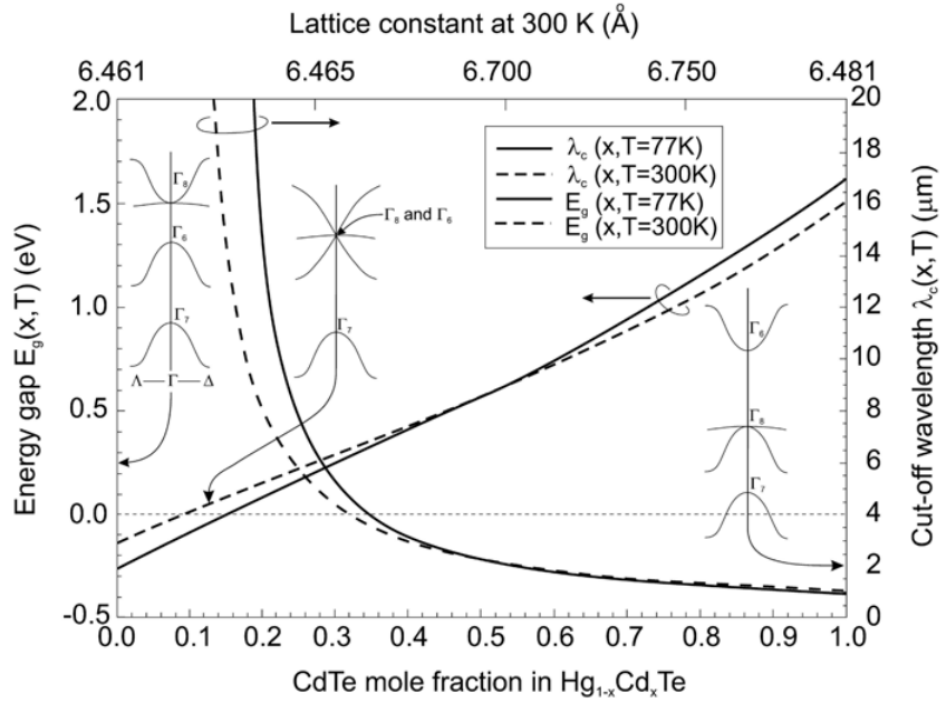


Figure 1.1 The band gap structure of  $\text{Hg}_{1-x}\text{Cd}_x\text{Te}$  near the  $\Gamma$ -point for three different values of the forbidden energy gap.<sup>2</sup>

## 1.2 Material properties of HgCdTe

The technically favorable material properties of HgCdTe include the following<sup>3</sup>: (i) band-gap engineered films with low etch pit density (EPD) ( $<1 \times 10^5 \text{ cm}^{-2}$ ) and excellent lateral uniformity; (ii) several available epitaxial growth methods including liquid phase epitaxy (LPE), molecular beam epitaxy (MBE), and metal-organic vapor phase epitaxy (MOVPE); (iii) convenient  $n$ -type and  $p$ -type dopants; (iv) versatile methods for forming mesas, planar homojunctions and heterojunctions; and (v) a small change (0.3%) in lattice constant over the entire alloy composition range. Key material properties of  $\text{Hg}_{1-x}\text{Cd}_x\text{Te}$  ternary alloys are compiled in Table 1.1.<sup>2</sup>

Property	HgTe	$\text{Hg}_{1-x}\text{Cd}_x\text{Te}$						CdTe
$x$	0	0.194	0.205	0.225	0.31	0.44	0.62	1.0
$a$ (Å)	6.461	6.464	6.464	6.464	6.465	6.468	6.472	6.481
	77 K	77 K	77 K	77 K	140 K	200 K	250 K	300 K
$E_g$ (eV)	-0.261	0.073	0.091	0.123	0.272	0.474	0.749	1.490
$\lambda_c$ (μm)	—	16.9	13.6	10.1	4.6	2.6	1.7	0.8
$n_i$ (cm <sup>-3</sup> )	—	$1.9 \times 10^{14}$	$5.8 \times 10^{13}$	$6.3 \times 10^{12}$	$3.7 \times 10^{12}$	$7.1 \times 10^{11}$	$3.1 \times 10^{10}$	$4.1 \times 10^5$
$m_c/m_0$	—	0.006	0.007	0.010	0.021	0.035	0.053	0.102
$g_c$	—	-150	-118	-84	-33	-15	-7	-1.2
$\epsilon_s/\epsilon_0$	20.0	18.2	18.1	17.9	17.1	15.9	14.2	10.6
$\epsilon_\infty/\epsilon_0$	14.4	12.8	12.7	12.5	11.9	10.8	9.3	6.2
$n_r$	3.79	3.58	3.57	3.54	3.44	3.29	3.06	2.50
$\mu_e$ (cm <sup>2</sup> V <sup>-1</sup> s <sup>-1</sup> )	—	$4.5 \times 10^5$	$3.0 \times 10^5$	$1.0 \times 10^5$	—	—	—	—
$\mu_{hh}$ (cm <sup>2</sup> V <sup>-1</sup> s <sup>-1</sup> )	—	450	450	450	—	—	—	—
$b = \mu_e/\mu_\eta$	—	1000	667	222	—	—	—	—
$\tau_R$ (μs)	—	16.5	13.9	10.4	11.3	11.2	10.6	2
$\tau_{A1}$ (μs)	—	0.45	0.85	1.8	39.6	453	$4.75 \times 10^3$	—
$\tau_{\text{typical}}$ (μs)	—	0.4	0.8	1	7	—	—	—
$E_p$ (eV)	—	—	—	19	—	—	—	—
$\Delta$ (eV)	—	—	—	0.93	—	—	—	—
$m_{hh}/m_0$	—	—	—	0.40–0.53	—	—	—	—
$\Delta E_v$ (eV)	—	—	—	0.35–0.55	—	—	—	—

$\tau_R$  and  $\tau_{A1}$  calculated for n-type HgCdTe with  $N_d = 1 \times 10^{15} \text{ cm}^{-3}$ . The last four material properties are independent of or relatively insensitive to alloy composition.

Table 1.1 Summary of material properties of  $\text{Hg}_{1-x}\text{Cd}_x\text{Te}$  ternary alloys.<sup>2</sup>

### 1.2.1 Lattice parameter

The lattice mismatch between available substrates and epitaxial MCT layers is one of the key issues in MCT epitaxial growth because it can result in significant degradation of device performance due to the formation of dislocations and strain. Moreover, the electrical properties are likely to be affected by compressive or tensile stress. The lattice parameter of MCT alloys, shown in Figure 1.1 and Table 1.1, is relatively constant over the entire range of Cd concentration  $x$ , thus making the epitaxial growth of MCT heterostructures possible. However, the brittleness of MCT with even very small lattice mismatch between layers can cause the generation of significant crystalline defects.

In order to correlate the variation of lattice parameter of MBE-grown  $\text{Hg}_{1-x}\text{Cd}_x\text{Te}$  on  $\text{Cd}_{1-y}\text{Zn}_y\text{Te}$  (CZT), Skauli and Colin<sup>6</sup> measured the lattice constants of both  $\text{Hg}_{1-x}\text{Cd}_x\text{Te}$  epilayers and CZT substrates simultaneously using high-resolution X-ray diffraction. It was found that the unstrained lattice parameter of  $\text{Hg}_{1-x}\text{Cd}_x\text{Te}$  as a function of Cd concentration  $x$  at room temperature obeyed Vegard's law, with the following relationship for the lattice constant,  $a$ :

$$a(x) = 6.4815x + 6.46152(1 - x) \quad (1.3)$$

with an error estimate of better than  $\pm 20$  ppm.

Temperature dependence of lattice parameter,  $a(T)$ , of MCT can be calculated using:

$$a(T) = a(300 \text{ K}) + B(T) (\text{\AA}) \quad (1.4)$$

where  $T$  is the temperature in K,  $a(300\text{ K})$  is the lattice parameter at room temperature, and  $B(T)$  has the values given in Table 1.2.<sup>7</sup>

Thus, the lattice parameter of  $\text{Hg}_{1-x}\text{Cd}_x\text{Te}$  is relatively constant over the entire range of Cd concentration  $x$ , and obeys Vegard's law for stoichiometric and unstrained  $\text{Hg}_{1-x}\text{Cd}_x\text{Te}$ . Hence, the change of MCT lattice parameter with Cd concentration provides a means to determine material composition simply using lattice parameter measurements.<sup>2</sup>

$T$	100	200	300	400	500	600	700	800
$B(T)$	-0.007	-0.004	0.0	0.003	0.006	0.01	0.014	0.019

Table 1.2 Lattice parameter correction factor  $B(T)$  in equation (1.4) at various temperatures.<sup>7</sup>

### 1.2.2 Coefficient of thermal expansion

The coefficient of thermal expansion (CTE) of MCT epitaxial layers and its variation with temperature play critical roles in IR applications. The CTE mismatch between MCT layers and the supporting substrate or other neighboring MCT layers from high growth temperature to low operating temperature can lead to severe device degradation or even failure due to the formation of excessive thermal strain. The magnitude of the strain leading to device failure does not need to be large since MCT alloys are considered to be very soft materials with low



mechanical strength. This CTE mismatch problem becomes more severe in the case of large-area focal plane arrays.

There have been several reports of CTE values for MCT at room temperature as a function of Cd concentration  $x$ .<sup>2</sup> The most comprehensive experimental data was provided by Skauli et al.<sup>8</sup> The CTE measurements were performed on MBE-grown  $\text{Hg}_{1-x}\text{Cd}_x\text{Te}$  ( $0 \leq x \leq 0.7$ ) epilayers grown on lattice-matched  $\text{Cd}_{1-y}\text{Zn}_y\text{Te}$  ( $0 \leq y \leq 0.05$ ) substrates, again based on the measurement of lattice constants using high-resolution X-ray diffraction.

Figure 1.2 (a) illustrates the CTE values of MCT and CZT at room temperature as a function of Cd concentration  $x$  and Zn concentration  $y$ , respectively. The CTE of MCT at room temperature is relatively constant over the entire range of MCT alloy composition, having a weak positive correlation of CTE with Cd concentration  $x$ . Figure 1.2 (b) shows the difference of CTE between MCT samples and CZT substrates. For other growth techniques such as LPE and MOCVD which involve higher growth temperatures than MBE growth, differential thermal expansion becomes correspondingly more significant.

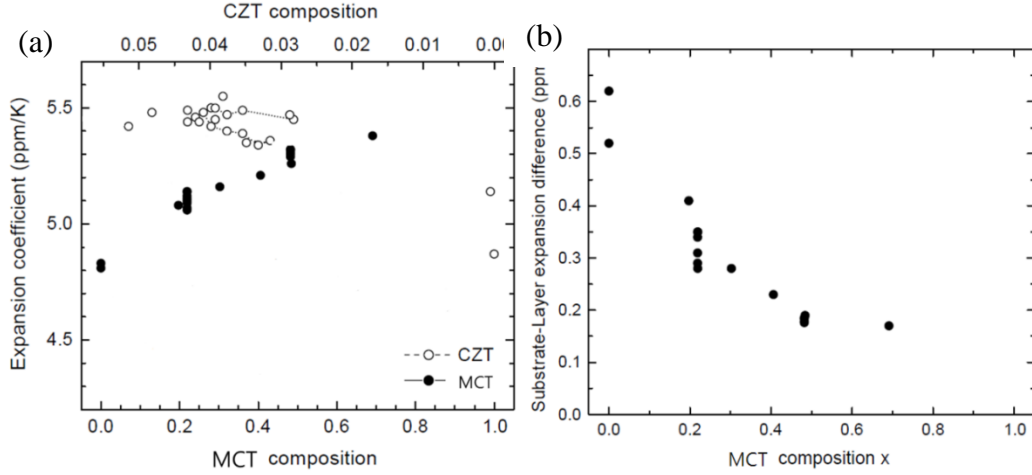


Figure 1.2 (a) CTE values for MCT (black circle) and CZT (open circle) as a function of Cd concentration  $x$  and Zn concentration  $y$ , respectively. (b) The difference of CTE between MCT samples and CZT substrates.<sup>8</sup>

### 1.3 Molecular beam epitaxy

MBE is one of the major growth techniques used by the semiconductor industry. MBE has led the way in the fabrication of novel film structures due to its unique combination of: (i) ultrahigh-vacuum conditions; (ii) low growth temperatures; (iii) precisely controllable sources of the film constituents; and (iv) *in situ* surface analysis tools such as reflection high-energy electron diffraction (RHEED) and spectroscopic ellipsometry (SE).<sup>9</sup> Since the first epitaxial growth of HgCdTe on CdTe substrate by MBE was demonstrated,<sup>10</sup> considerable progress in reducing defects and improving growth and doping control has been achieved, thus improving the performance of IR electro-optical devices. As focal-plane arrays (FPAs) have moved to second and third generations, MBE has become the

technology of choice for growth of HgCdTe on large-area substrates.<sup>11</sup> Moreover, MBE allows the growth of complex layered structures such as double- and triple-layer heterostructures as well as graded layers, because of its capability to precisely control composition, doping, and interfacial profile.

#### 1.4 Substrates for HgCdTe growth

The golden rule for epitaxial growth is to use a lattice-matched substrate. In the mid-1980s, bulk  $\text{Cd}_{0.96}\text{Zn}_{0.04}\text{Te}$  (CZT) substrates replaced CdTe which had the drawback of lattice mismatch of a few per cent with MCT for LWIR and MWIR applications.<sup>7</sup> However, CZT substrates have severe shortcomings related to the lack of large areas as well as high fabrication costs. Moreover, the difference of CTE between CZT substrates and Si readout integrated circuits (ROIC) and recent interest in large-area IR FPAs ( $1\text{ k} \times 1\text{ k}$  and  $2\text{ k} \times 2\text{ k}$ ) have greatly restricted CZT substrates for IR FPA applications. At present, the largest commercially available bulk CZT substrate is  $7 \times 7\text{ cm}^2$ .<sup>13</sup> At this size, the wafers used for growth are unable to accommodate more than eight  $2\text{ k} \times 2\text{ k}$  FPAs.

There have been significant efforts over the past three decades to identify substrate materials alternative to lattice-matched CZT. As a result, composite substrates consisting of epilayers of CdTe or CZT grown on Si, GaAs, InSb, sapphire, and Ge substrates have been investigated because of greater robustness, lower cost, higher thermal conductivity, greater lateral uniformity, and larger

possible area compared with bulk CZT substrates.<sup>14</sup> Table 1.3 provides a comparison of key attributes of bulk CZT, GaAs, and Si substrates.

Past efforts have focused on using an Si-based composite substrate technology, especially CdTe/Si, for MCT materials development,<sup>13</sup> because Si-based substrates offer many benefits over other materials. These advantages for Si include: (i) commercial availability of larger area substrates; (ii) perfect thermal match to the ROIC; (iii) lowest material cost; (iv) high material quality; (v) well-developed technologies for Si device fabrication; (vi) material robustness and durability (less breakage and higher device yields); (vii) high thermal conductivity (the highest lateral uniformity of the MBE growth temperature and hence of the MCT composition and thickness); (viii) lowest level of impurity migration into MCT, and (ix) lowest density of surface defects.<sup>3</sup> In contrast, however, Si has the worst lattice and thermal mismatches with MCT of any practical substrate material. The lattice parameter of MCT ( $\sim 6.46 \text{ \AA}$ ) is 19 % larger than that of Si ( $\sim 5.43 \text{ \AA}$ ) at room temperature. This extreme lattice mismatch requires the use of buffer layers such as CZT,  $\text{Cd}_{0.96}\text{Se}_{0.04}\text{Te}$ ,  $\text{Cd}_{0.96}\text{Zn}_{0.04-y}\text{Se}_y\text{Te}$ , and CdTe for the growth of MCT.<sup>3</sup> Even though the first three of these possible buffer layers are almost perfectly lattice-matched to MCT, their use has been restricted because of the difficulty of obtaining epilayers of sufficient crystalline quality. Even the best CdTe buffer layers exhibit  $\text{EPD} > 5 \times 10^4 \text{ cm}^{-2}$ , leading to dislocation densities for MBE-grown MCT on CdTe/Si composite substrates in the mid-to-high  $10^6$

$\text{cm}^{-2}$  range, which is about two orders of magnitude higher than that of MCT grown on bulk lattice-matched CZT substrates.<sup>13</sup> It has been demonstrated that this higher dislocation level results in deterioration in device performance, especially in the LWIR region.<sup>13</sup> Thus, ongoing efforts focus on either reducing the dislocation density of MCT grown on CdTe/Si substrates or rendering the dislocations electrically inactive.<sup>16-18</sup>

	$\text{Cd}_{1-y}\text{Zn}_y\text{Te}$ ( $y = 0.04$ )	GaAs	Si
Cost ( $\text{cm}^{-2}$ )	US \$ 400 (high-pressure Bridgman growth)	US \$ 0.71 (vertical gradient freeze growth; US \$ 28.00 w/CdTe buffer)	US \$ 0.02 (Czochralski growth; US \$ 1–3 w/CdTe buffer)
Largest commercially available size	49.0 $\text{cm}^2$ square	182.4 $\text{cm}^2$ circular	706.9 $\text{cm}^2$ circular
Robustness of material	Brittle	Moderately robust	Strong
Vickers hardness ( $\text{kg mm}^{-2}$ at 300 K)	60	360	1150–1330
Thermal conductivity ( $\text{mW cm}^{-1} \text{K}^{-1}$ )	55	500	1235
Surface preparation	Difficult, sometimes poor	Standardized by large III–V industry	Standardized by large Si industry
Substrate surface defect density ( $\text{cm}^{-2}$ )	$10^4$	$5 \times 10^3$ ( $10^5$ on CdTe buffer)	$10^2$ ( $10^5$ on CdTe buffer)
Lattice mismatch with HgCdTe ( $x = 0.2$ at 300 K)	<0.1%	13.6% (<1% w/CdTe)	19.47% (<1% w/CdTe)
Substrate etch pit density ( $\text{cm}^{-2}$ )		<500 on CdTe buffer	<5000 on CdTe buffer
Thermal mismatch with HgCdTe ( $x = 0.2$ at 300 K)	3.53%	27.04% (1.85% w/CdTe)	51.85% (1.85% w/CdTe)
Valence issues	None	Minor with CdTe buffer	Severe but solved
Other	Impurities, crystalline defects, compositional uniformity problem, large thermal mismatch with Si ROIC.	<i>In situ</i> surface preparation may cause contamination.	Allows monolithic integration. Requires buffer layer

Table 1.3 Some characteristics of CZT, Si, and GaAs substrates.<sup>15</sup>

## 1.5 Outline of dissertation

The research in this dissertation has involved using transmission electron microscopy (TEM) techniques to characterize microstructural properties of MBE-grown HgCdTe alloys and related materials as well as substrates, being used or considered for HgCdTe growth. The materials investigated have included ZnTe epilayers ( $\sim 6 \mu\text{m}$ ) grown on Si(211) or Si(100) substrates, HgCdTe/CdTe or CdTe layers grown on GaAs(211)B substrates, and ZnTe epilayers grown on GaSb(211)B substrates.

In chapter 2, the details of experimental procedures involved in this dissertation are summarized. MBE growth methods for HgCdTe alloys and related materials are briefly described. Cross-sectional TEM specimen preparation methods and TEM techniques essential for characterization are also described.

In chapter 3, the MBE growth conditions for thick ZnTe epilayers grown on Si(211) and Si(100) substrates are investigated, and X-ray diffraction (XRD), dislocation density, surface morphology, and TEM results are described. Comparisons between ZnTe(211)/Si(211) and ZnTe(100)/Si(100) interfaces using high resolution electron microscopy and small-probe microanalysis are also summarized.

In chapter 4, the microstructural characterization of CdTe/GaAs(211)B epilayers grown by MBE as a platform of HgCdTe growth is described. The microstructure of MBE-grown HgCdTe layers on CdTe/GaAs(211)B composite

substrates was characterized using a wide range of TEM imaging and analytical techniques. The amount of residual strain at the CdTe/GaAs(211)B interface was also estimated using digital image processing.

In chapter 5, issues relating to the critical thickness for MBE-grown ZnTe epilayers on GaSb(211)B substrates are described. Theoretical predictions of the critical thickness from three models were used for comparisons with experimental data from high resolution x-ray diffraction as well as TEM.

In chapter 6, the major results of this dissertation research are summarized, and possible future studies of alternative materials to HgCdTe as well as expectations for state-of-art TEM techniques are briefly described.

## REFERENCES

- <sup>1</sup> W. D. Lawson, S. Nielson, E. H. Putley, and A. S. Young, *J. Phys. Chem. Solids* 9, 325 (1959).
- <sup>2</sup> A. Rogalski, *Rep. Prog. Phys.* 68, 2267 (2005).
- <sup>3</sup> P. Capper, J. Garland, and S. Kasap, *Mercury Cadmium Telluride: Growth, Properties and Applications*, John Wiley & Sons (2010).
- <sup>4</sup> G. L. Hansen, J. L. Schmit, and T. N. Casselman, *J. Appl. Phys.* 53, 7099 (1982).
- <sup>5</sup> J. P. Laurenti, J. Camassel, A. Bouhemadou, B. Toulouse, R. Legros, and A. Lusson, *J. Appl. Phys.*, 67, 6454 (1990)
- <sup>6</sup> T. Skauli, and T. Colin, J., *Cryst. Growth*, 222, 719–725 (2001).
- <sup>7</sup> P. Capper, *Properties of Narrow Gap Cadmium-based Compounds*, INSPEC (1994).
- <sup>8</sup> T. Skauli, R. Haakenaasen, and T. Colin, *J. Cryst. Growth*, 241, 39–44 (2002).
- <sup>9</sup> J. R. Arthur, *Surf. Sci.*, 500, 189 (2002).
- <sup>10</sup> J. P. Faurie, and A. Million, *J. Cryst. Growth* 54, 582 (1981).
- <sup>11</sup> M. Reddy, J. M. Peterson, D. D. Lofgreen, J. A. Franklin, T. Vang, E. P. G. Smith, J. G. A. Wehner, I. Kasai, J. W. Bangs, and S. M. Johnson, *J. Electron. Mater.* 37, 1274 (2008).
- <sup>12</sup> R. Triboulet, A. Tromson-Carli, D. Lorans, and T. Nguyen Duy, *J. Electron. Mater.* 22, 827–834 (1993).



- <sup>13</sup> G. Brill, Y. Chen, P. Wijewarnasuriya, and N. Dhar, Proc. SPIE 7419 74190L-1 (2009).
- <sup>14</sup> M. A. Kinch, J. Electron. Mater. 39, 1043 (2010).
- <sup>15</sup> J. W. Garland and G. Dhanaraj, Molecular Beam Epitaxial Growth of HgCdTe, Springer Handbook of Crystal Growth, Springer-Verlag (2010).
- <sup>16</sup> Y. Chen, S. Farrell, G. Brill, P. Wijewarnasuriya, and N. Dhar, J. Cryst. Growth, 310, 5303 (2008).
- <sup>17</sup> L. A. Almeida, M. Groenert, J. Molstad, J. Markunas, J. Dinan, M. Carmody, D. Edwall, J. Pasko, J. Arias, Proc. of the 24th Army Science Conference, (2004).
- <sup>18</sup> G. Brill, S. Farrell, Y. Chen, P. Wijewarnasuriya, Mulpuri V. Rao, J. Benson, N. Dhar, J. Electron. Mater. 39, 967 (2010).

## Chapter 2

### EXPERIMENTAL PROCEDURES

This chapter first presents a brief overview of the methods used by our collaborators for materials growth using molecular beam epitaxy (MBE). Sample preparation methods suitable for electron microscopy examination of ZnTe films grown on Si or GaSb substrates, and HgCdTe/CdTe/GaAs or CdTe/GaAs heterostructures are then described in detail. Finally, transmission electron microscopy (TEM) techniques, including high resolution transmission electron microscopy (HREM), scanning transmission electron microscopy (STEM), and energy-dispersive x-ray spectroscopy (EDXS), which are heavily used in the experimental studies described in the later chapters, are summarized.

#### 2.1 MBE growth

Extensive reviews about the MBE growth technique can be found elsewhere.<sup>1,2</sup> Figure 2.1 provides a schematic of a typical MBE growth chamber. The following provides a brief summary of the technique. The sources of the growth constituents are localized beams of atoms or molecules maintained in an ultrahigh-vacuum environment to minimize substrate contamination. These atoms and molecules travel in nearly collision-free paths until arriving at the substrate which is usually kept at a moderate temperature to provide enough thermal energy

for arriving atoms to migrate along the surface. Shuttering allows the beams to be turned on or off almost instantly, allowing the composition of the arriving stream of atoms to be changed in times that can be much shorter than the growth time for a single atomic layer.

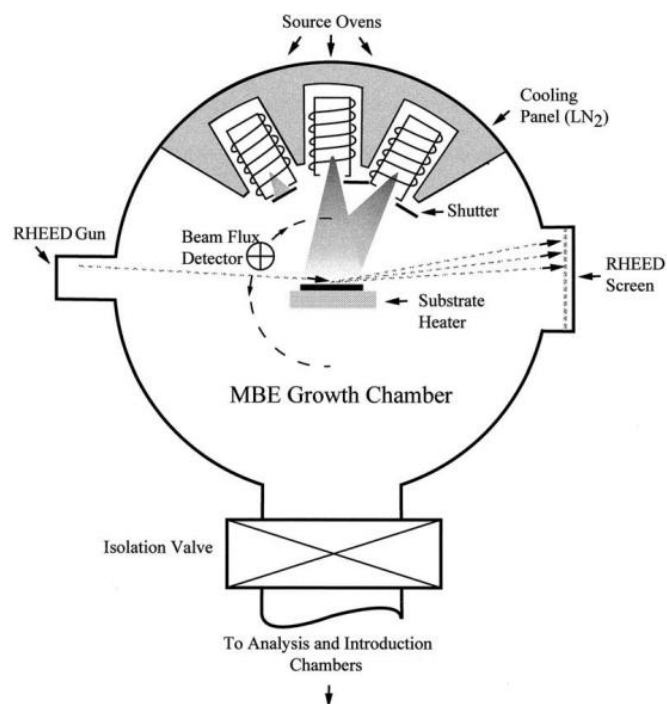


Figure 2.1 Top view of a simple MBE chamber showing the essential growth sources, shutters, beam flux detector, and the reflection-high-energy electron diffraction (RHEED) system used for monitoring surface structure during growth.<sup>1</sup>

Because the typical growth rates are as low as about 1 to 3 monolayers/sec or even less, partial pressures of approximately  $10^{-12}$  torr of the background species would be required in order to keep their arrival rate at  $10^{-6}$  of the growth rate. However, most background species have low sticking coefficients, so that such a high vacuum is not required. For HgCdTe growth, the background pressure is between  $10^{-7}$  and  $10^{-8}$  torr, about 100 times higher than for normal III–V growth because of high Hg partial pressures. Substrates are typically loaded into the growth chamber via a load-lock chamber, where they are outgassed before insertion into the major MBE chamber.

The growth chamber contains source ovens, beam shutters, actuating mechanisms, substrate holder and heater, *in situ* characterization tools, beam-flux monitors, and cryo-panels to act as cryo-pumps. The chamber must be designed to minimize outgassing, to keep the substrate at a uniform temperature, to provide well controlled fluxes to the substrate, and to avoid any temperature transients on the growth surface from shuttering and unshuttering of the source beams. Variations in the flux ratios and the temperature of the growing surface easily lead to compositional variations, which can impair overall crystalline quality.

### 2.1.1 MBE growth of ZnTe films on Si substrates

The samples of ZnTe films on Si substrates described in a later chapter were grown using an MBE system manufactured by DCA Instruments, and equipped

with a 3.25-inch substrate heater.<sup>3</sup> The growth of ZnTe on 3-inch Si(211) or Si(100) substrates was initiated with a seeding layer of thin ZnTe nucleated at approximately 300 °C utilizing migration-enhanced epitaxy (MEE) with elemental Zn and Te sources, in which the Zn and Te cell shutters were alternately opened for 10 seconds with a 10 second pause between each opening. After nucleation, the seed layer was then annealed at 420 °C under Te flux for 10 minutes, followed by deposition of a thick (~6 µm) ZnTe layer onto the seed layer using a ZnTe compound source with additional Te or Zn or neither, depending on the experimental parameters of choice. The growth rate of ZnTe was approximately 0.6 µm/h. During ZnTe growth, the layer was periodically annealed at 460 °C under Te overpressure. This flash annealing improved the ZnTe layer quality. The microscopy studies reported later focused on the substrate pretreatment prior to film growth, as well as the nucleation and growth temperatures for ZnTe, and changes in the Zn/Te flux ratio used during growth.

#### 2.1.2 MBE growth of HgCdTe/CdTe or CdTe grown on GaAs substrates

Commercially available 3-inch GaAs(211)B substrates were loaded into the MBE chamber and heated to the native oxide desorption temperature (580 °C) under an As<sub>4</sub> overpressure.<sup>4</sup> The substrates were then cooled for a low-temperature CdTe nucleation step followed by annealing. In an effort to encourage interaction and annihilation of threading dislocations, subsequent

annealing cycles were implemented at regular intervals throughout the remainder of the CdTe growth. A typical growth cycle consisted of deposition of 1  $\mu\text{m}$  of CdTe followed by Te-stabilized annealing for 5 min. Ramp rates were typically 0.5°C/min. The CdTe thickness typically ranged from 9  $\mu\text{m}$  to 13  $\mu\text{m}$ . After CdTe buffer growth, the CdTe/GaAs composite substrate was transferred *in vacuo* to a second MBE chamber for the HgCdTe growth.

Initiation of HgCdTe growth took place after a brief anneal at  $\sim 300^\circ\text{C}$ . The purpose of this step was to eliminate any species that might have adsorbed on the CdTe surface during vacuum transfer. A 1- $\mu\text{m}$ - to 1.5- $\mu\text{m}$ -thick HgCdTe buffer layer was then grown, followed by a  $\sim 6\text{-}\mu\text{m}$ - to 8- $\mu\text{m}$ -thick  $\text{Hg}_{0.77}\text{Cd}_{0.23}\text{Te}$  absorber layer. The intent of the HgCdTe buffer layer was to provide a material with an intermediate lattice parameter between the CdTe buffer and  $\text{Hg}_{0.77}\text{Cd}_{0.23}\text{Te}$  absorber layers. Finally, a 0.5- $\mu\text{m}$ -thick protective cap layer ( $x \approx 0.3$ ) was grown. Spectroscopic ellipsometry was used during HgCdTe growth for control of composition and temperature. The nominal HgCdTe growth temperature was  $185^\circ\text{C}$ .

### 2.1.3 MBE growth of ZnTe films on GaSb(211)B substrates

The ZnTe layers were deposited on GaSb(211)B substrates using a DCA MBE system after removal of the surface oxides from the GaSb wafer by exposure to atomic hydrogen for 20 min at  $400^\circ\text{C}$ .<sup>5</sup> Migration-enhanced epitaxy

was employed to nucleate the ZnTe epilayers. With the substrate temperature kept at 320 °C, the surface was exposed to Zn for 60 s followed by a sequence of ten periods of alternating exposures of Zn and Te simultaneously for 5 s and followed by Zn exposure for 60 s. The ZnTe layers were subsequently deposited to thicknesses in the range from 50 nm to 2,000 nm by conventional MBE where both the Zn and Te shutters were simultaneously opened for the remaining growth time.

## 2.2 TEM specimen preparation

The specimens intended for cross-sectional TEM observation were prepared using standard mechanical polishing and ion-milling procedures with the sample held at liquid-nitrogen temperature to avoid ion-milling artefacts.<sup>6</sup> Figure 2.2 illustrates all of the major procedures normally used for making cross-sectional TEM specimen.

First, a piece of Si or GaSb wafer on which ZnTe layers were to be grown, was mounted on a glass slide and placed on a hot plate set to 160 °C using crystal wax. It was then sliced into small pieces using a diamond blade cutter. Those two small pieces were then glued with film layers face-to-face using M-bond adhesive. The samples had to be gently pressed with a specimen clamp to remove excess glue from the two pieces. The specimens were then placed into an oven for curing with a temperature of no greater than 90 °C for a period of about 60 minutes.

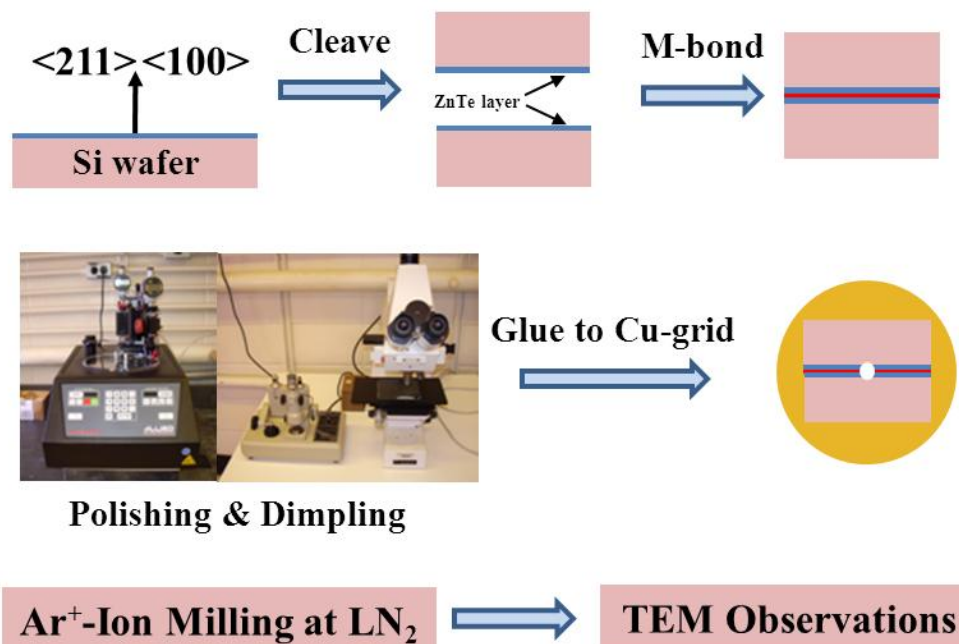


Figure 2.2 Schematic showing procedures used for TEM specimen preparation.

After curing, standard mechanical polishing and dimpling were applied for further thinning of the specimen. The first side of the specimen was gently polished using the Allied MultiPrep polishing system. Table 2.1 shows detailed setups including platen speed and pressure as well as lubricant used with the Allied MultiPrep polishing system at each thickness of diamond lapping film. In addition, the thicknesses that have to be polished at each diamond lapping film step are also given.



<b>Diamond lapping film (<math>\mu\text{m}</math>)</b>	<b>Platen speed (rpm) /Platen pressure</b>	<b>Thickness to be polished (<math>\mu\text{m}</math>)</b>	<b>Lubricant</b>
30	100/3	200	Water
15	100/3	100	Water
6	75/3	50	Water
3	75/2	20	Water
1	50/1	10	Green lube
0.5	35/0.5	3~5	Green lube
0.1	25/0.5	1~2	Green lube

Table 2.1 Detail setup of Allied MultiPrep polishing system used at each stage when lapping diamond film for the first specimen side.

If there were any visible scratches remaining around the target area of interest after finishing polishing with 0.1  $\mu\text{m}$  diamond lapping film, the polishing steps from 1  $\mu\text{m}$  to 0.1  $\mu\text{m}$  would be repeated. The specimen was wiped with a Q-tip dipped in micro-organic soap by gently rolling the Q-tip onto the polished surface of the specimen, and it was then rinsed with deionized water. The specimen was then flipped over and the second side was polished down to a total thickness of  $\sim 100$   $\mu\text{m}$ , using 30  $\mu\text{m}$  to 3  $\mu\text{m}$  diamond lapping films. This treatment was followed by dimpling with a Cu-wheel and a cloth-wheel until the thickness of the specimen was less than  $\sim 10$   $\mu\text{m}$ . For Si substrates, the color of the dimpled Si gives a hint about when to stop dimpling. Si substrate specimen

was dimpled until its color became orange, indicating the thickness of the specimen is less than 10  $\mu\text{m}$ .

Conventional mechanical polishing with a Gatan dimpler for the CdTe or HgCdTe/CdTe layers grown on GaAs substrates caused the thickness of the CdTe or HgCdTe/CdTe layers to be about 10  $\mu\text{m}$  thinner than GaAs substrates after final cloth dimpling. Therefore, after ion-milling, it was very difficult to observe the interface region between thin CdTe and GaAs using TEM. Moreover, it was still challenging to find thin enough areas that showed an entire heterostructure including the top surfaces of the CdTe or HgCdTe layers as well as the GaAs substrates during TEM observation.

In an effort to overcome this problem, the Allied MultiPrep polisher was used to polish both sides of CdTe/GaAs and HgCdTe/CdTe/GaAs samples without any dimpling. The first side of the sample was polished by following the procedure outlined in Table 2.1, and then the second side was polished more gently, as shown in Table 2.2.

The specimen was then glued onto a copper grid with M-bond since the specimen was still on a glass stub. After curing in a low temperature oven (90°C), the specimen would be placed in fresh acetone for about an hour to remove the glass stub from the specimen. The specimen was finally argon-ion-milled at 2.5 keV and 7 degree, while held at liquid nitrogen temperature using Gatan Model 691 PIPS system until hole perforation was achieved. Low-angle (6 degree), low-

energy (approximately 1.8 keV) milling was often used for final thinning to minimize the formation of any amorphous surface or interfacial layers.

<b>Diamond lapping film (<math>\mu\text{m}</math>)</b>	<b>Platen speed (rpm) /Platen pressure</b>	<b>Thickness (<math>\mu\text{m}</math>) of the sample after polishing</b>	<b>Lubricant</b>
30	100/2	250	Water
15	100/2	150	Water
6	75/1	75	Water
3	75/1	35	Water
1	50/0.5	5 ~ 10	Green lube
0.1	25/0.2	5 ~ 10	Green lube

Table 2.2 Detail setup of Allied MultiPrep polishing system at each thickness of diamond lapping film for polishing the second side of CdTe/GaAs and HgCdTe/CdTe/GaAs samples.

## 2.3 Electron microscopy

### 2.3.1 High resolution transmission electron microscopy

Conventional TEM uses amplitude contrast (diffraction contrast) with a small objective aperture for image formation from crystal grains of different structure, phase, or orientation, distortion induced by particles and dislocations, and variations of the scattering amplitude by stacking faults and grain boundaries.

On the other hand, HREM imaging uses phase contrast with a large objective aperture (even with no objective aperture) resulting from the interference of several electron beams over a wide range of scattering angles. HREM images are sensitive to many factors, including specimen thickness, specimen orientation, and atomic scattering factors, and are also strongly affected by properties of the imaging system, such as variations in the focus and spherical aberration of the objective lens.<sup>7</sup>

HREM allows imaging of the crystal structure of thin specimens at the atomic scale, and thus individual atom columns can be resolved. The applications of HREM to diverse materials, such as semiconductors, metals, oxides and ceramics, and to the study of dislocations, interfaces and surfaces have been reported at many scientific conferences and many journal articles.<sup>8</sup>

Most of the electron microscopy observations reported here were carried out using a JEOL JEM-4000EX high-resolution electron microscope, operated at 400keV, and equipped with a double-tilt, top-entry-type sample holder. The top-entry-type sample holder provides high stability against sample drift, which is essential for high resolution. All of the high-resolution images were taken under similar microscope operating conditions and the microscope was always corrected for objective-lens astigmatism and axial coma before final image recording took place. Both phase-contrast and diffraction-contrast imaging were used to characterize the thin-film samples. Specimens were usually oriented for TEM

observation along the common  $\langle 110 \rangle$  projection. Digital image processing based on lattice-fringe images was performed using Gatan DigitalMicrograph software.

### 2.3.2 Scanning transmission electron microscopy and energy-dispersive x-ray spectroscopy

A schematic illustrating major components of a STEM is shown in Figure 2.3. A field-emission gun provides a high-coherence source of electrons, which are usually accelerated between 100 and 300 keV. These energies are sufficient for electrons to penetrate TEM samples up to 100 nm thick without significant beam spreading. A series of electron lenses before the sample focuses the beam down to Ångstrom-scale dimensions, which is often smaller than the spacing between the projected atomic columns. The focused beam passes through the sample, and is scattered in all directions, so that a wide range of different signals is possible.

The transmitted electrons collected at relatively small angles (smaller than  $\sim 10$  mrad) with respect to the optic axis are used to form bright-field diffraction contrast images. On the other hand, incoherent electrons scattered at relatively high angles (larger than  $\sim 50$  mrad) are used to form high-angle annular-dark-field (HAADF) images using an ADF detector, as first developed by Crewe and colleagues.<sup>10</sup> HAADF imaging is usually referred to as “Z-contrast” imaging, because electrons reaching the HAADF detector give contrast roughly

proportional to the mean square of the atomic number.<sup>11-13</sup> A major advantage of HAADF imaging is that the image is free of contrast reversal over a large range of thicknesses and defocus, thereby possibly providing direct identification of the atomic arrangements at heterostructure interfaces by overcoming the image-interpretation problems of HREM imaging that are caused by dynamical diffraction.<sup>13-15</sup>

The EDXS technique is used to analyze distributions of sample composition, which is especially useful at sample interfaces. The electron beam incident on a sample excites electron from inner shells, leaving vacancies in the original shell. Electrons from higher-energy, outer shells then fill the holes, together with emission of X-rays. The corresponding energies of the emitted X-rays carry characteristic information about the chemical species present in the specimen. The spatial resolution of the EDXS signal is mainly determined by the probe size and the interaction volume within the sample. In addition, transmitted electrons that have lost measurable amounts of energy when passing through the sample can be analyzed using the technique of electron-energy-loss spectroscopy (EELS) to extract further information about local variations in sample composition.

In this research, HAADF imaging and EDXS were carried out using a 200 keV JEOL 2010F, equipped with a field-emission electron gun, double-tilt sample holder, charge-coupled-device (CCD) electron camera, ADF detector, EDX and EELS detectors. This microscope has a structural resolution of 1.9 Å in TEM

imaging mode and an instrumental resolution of 1.4 Å in ADF-STEM mode. In this work, HAADF images were usually obtained using a focused probe diameter of ~0.2 nm and the camera length of 6cm, while elemental composition profiles were obtained with a probe size of ~1 nm as the electron probe was scanned across the region of interest.

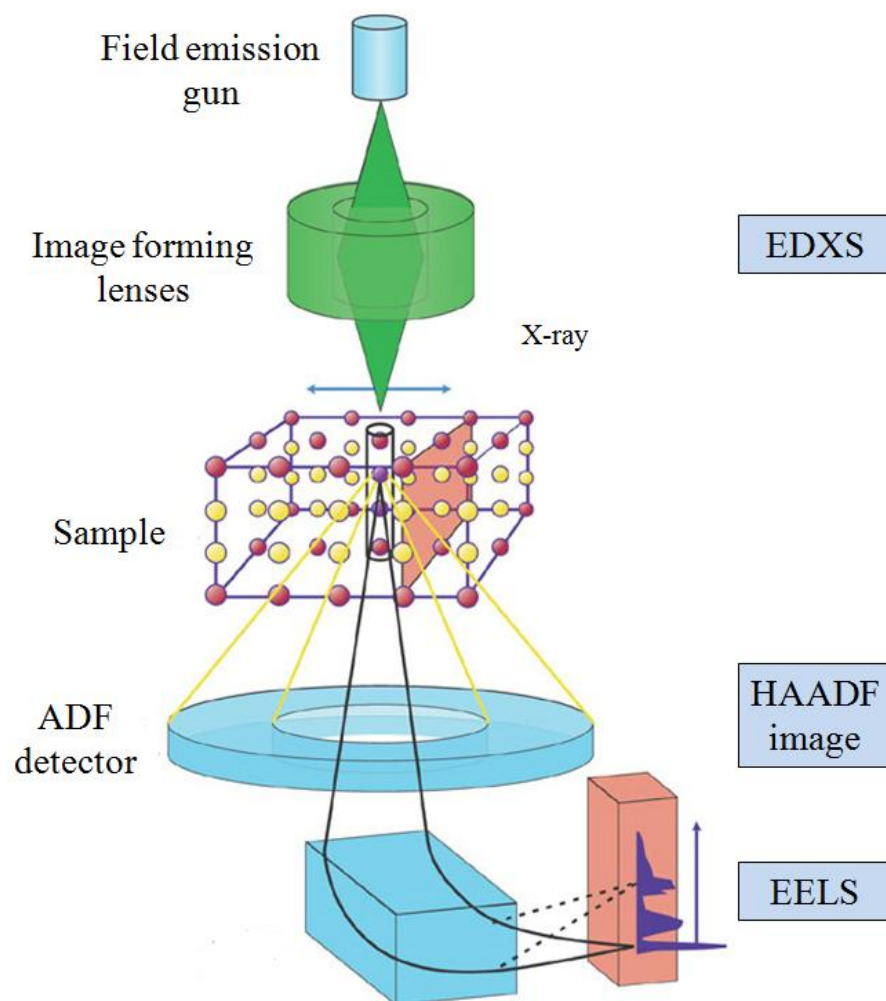


Figure 2.3 Schematic showing the essential components associated with the scanning transmission electron microscopy technique.<sup>9</sup>



## REFERENCES

- <sup>1</sup> J. R. Arthur, Surf. Sci., 500, 189 (2002).
- <sup>2</sup> J.Y. Tsao, Materials Fundamentals of Molecular Beam Epitaxy, Academic Press, Boston (1993).
- <sup>3</sup> Y. Chen, S. Simingalam, G. Brill, P. Wijewarnasuriya, N. Dhar, J. J. Kim, and D. J. Smith, J. Electron. Mater. 41, 10(2012).
- <sup>4</sup> J. J. Kim, R. N. Jacobs, L. A. Almeida, M. Jaime-Vasquez, C. Nozaki, J.K. Markunas, J. D. Benson, and D. J. Smith, J. Electron. Mater. (2012). *submitted*.
- <sup>5</sup> J. Chai, O. C. Noriega, J. H. Dinan, and T. H. Myers, J. Electron. Mater. 41, 3001(2012).
- <sup>6</sup> C. Wang, D. J. Smith, S. Tobin, T. Parodos, J. Zhao, Y. Chang and S. Sivananthan, J. Vac. Sci. Technol. A **24**, 995 (2006).
- <sup>7</sup> D. B. Williams, and C. B. Carter, Transmission Electron Microscopy, Springer (1996).
- <sup>8</sup> D. J. Smith, Rep. Prog. Phys. 60, 1513 (1997).
- <sup>9</sup> D.A. Muller, Nature Mater. **8**, 263 (2009).
- <sup>10</sup> A. V. Crewe, and J. Wall, J. Mol. Biol. 48, 375 (1970).
- <sup>11</sup> J. Wall, J. Langmore, M. Isaacson and A.V. Crewe, Proc. Natl Acad. Sci. **71**, 1 (1974).
- <sup>12</sup> A. Howie, J. Microsc. **17**, 11 (1979).
- <sup>13</sup> E. J. Kirkland, R. F. Loane and J. Silcox, Ultramicroscopy **23**, 77 (1987).

<sup>14</sup> J. Fertig and H. Rose, *Optik* **59**, 407 (1981).

<sup>15</sup> R.F. Loane, E. J. Kirkland and J. Silcox, *Acta Crystallogr. A* **44**, 912 (1988).

## Chapter 3

## CHARACTERIZATION OF ZnTe/Si COMPOSITE SUBSTRATES

This chapter describes the characterization of MBE-grown ZnTe/Si composite substrates. The samples were provided by Dr. Yuanping Chen and colleagues at U.S. Army Research Laboratory (Adelphi, MD). My role has been the microstructural characterization using electron microscopy. Some of the major results of this collaborative research have already been published elsewhere.<sup>1</sup>

## 3.1 Introduction

Although HgCdTe (MCT) has been a dominant material in IR FPA applications, the difficulties in MCT growth caused by segregation between CdTe and HgTe and the high vapor pressure of Hg have stimulated the investigation of alternative materials over the last half century.<sup>2</sup> Moreover, a barrier to the use of MCT grown on scalable substrates such as CdTe/Si composite substrates is its dislocation density which is one to two orders of magnitude higher than for MCT grown on bulk lattice-matched CdZnTe substrates. A number of possibly competitive alternative systems to MCT have been developed, including PbSnTe, type-II superlattices (T2-SLs) (InAs-GaSb and related alloys), quantum-well IR photodetectors (QWIPs) (especially GaAs/AlGaAs multiple-quantum-well detectors), and Hg-based materials.<sup>2</sup> However, none of these has so far been successful in displacing MCT as the dominant choice for IR applications.

Type-II InAs/GaSb strained-layer superlattices<sup>3</sup> and HgCdSe<sup>4</sup> alloys have been recently revisited for LWIR applications. These compound semiconductor systems have lattice constants close to  $6.1 \text{ \AA}$ , as shown in Figure 3.1. Furthermore, they can be grown on closely lattice-matched and commercially available GaSb substrates. Although GaSb substrates seem to be suitable, there are drawbacks to their use, such as the limited size of commercially available substrates (currently up to 4-inch diameter), relatively high cost (about  $\$88/\text{cm}^2$ ), and the difficulty of growing HgCdSe on GaSb, due to potential interface mixing and/or autodoping.<sup>1</sup> Thus, it is desirable to develop an alternative low-cost and scalable substrate with lattice constant very near  $6.1 \text{ \AA}$ , which can be tuned to lattice-match any configured T2-SLS system or HgCdSe alloy. For these various reasons, Ze(Se)/Te/Si composite substrates represent promising candidates for both systems because they can provide a lattice-matched, large-area, low-cost substrate for II-VI and III-V compound semiconductors with lattice constants near  $6.1 \text{ \AA}$  simply by adding Se into a ZnTe matrix.

The development of thin ZnTe buffer layers grown on Si substrates has accelerated the development of a CdTe/Si composite substrate to replace bulk CZT substrates for MCT growth because it bridges the mismatch of lattice constants ( $\sim 19 \%$ ) between CdTe and Si. However, the growth of ZeTe on Si substrate is still highly challenging due to the large lattice mismatch ( $\sim 12\%$ ). At present, most studies of ZnTe growth on Si have focused on the nucleation of the

thin ZnTe buffer layer, aiming for high quality CdTe/Si.<sup>5</sup> Little work has been reported in the literature for thick, high quality ZnTe/Si or ZnSeTe/Si composite substrates.

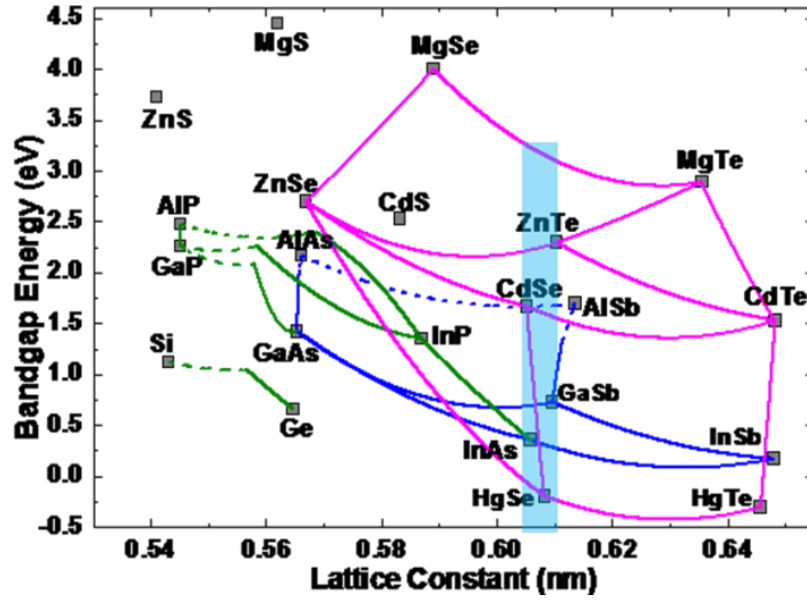


Figure 3.1 Energy gap versus lattice parameter for several semiconductor material systems. The shaded region highlights semiconductors that have lattice parameters near  $6.1 \text{ \AA}$ .<sup>1</sup>

The results reported here demonstrate that by using molecular beam epitaxy (MBE), growth can be optimized to obtain thick ZnTe(211)/Si(211) and ZnTe(100)/Si(100) films with high crystallinity, low defect density, and excellent surface morphology. Moreover, optimized MBE growth of ZnTe/Si will also help

to obtain lattice-matched ZnSeTe with the slight addition of Se into the ZnTe matrix, analogous to the successful MBE growth of CdSeTe on Si by employing an optimized growth process for CdTe on Si.<sup>6</sup>

### 3.2 Experimental details

The samples of ZnTe films on Si substrates were grown using an MBE system manufactured by DCA Instruments, and equipped with a 3.25-inch substrate heater.<sup>1</sup> Three-inch Si(211) or Si(100) wafers were used as substrates, held by indium-free mounting during growth of the ZnTe films. The modified RCA process was used to clean the Si wafers prior to growth, leaving an approximately 12 Å-thick, uniform oxide layer on the Si surface.<sup>7</sup> This oxide layer was easily removed in the growth chamber through thermal decomposition at approximately 850 °C. After oxide removal, the Si substrates were cooled under molecular arsenic (As<sub>4</sub>) flux to 400 °C. During the oxide desorption process, reflection-high-energy-electron diffraction (RHEED) patterns were used to monitor the Si surface. Desorption of oxide from the Si surface was indicated through the change of the RHEED patterns caused by the Si surface reconstruction. Finally, the sample was cooled to the nucleation temperature under Te flux, Zn flux, or no flux, depending on the experimental condition of interest.

The growth of ZnTe on the Si substrate was initiated with a seeding layer of thin ZnTe nucleated at approximately 300 °C utilizing migration-enhanced epitaxy (MEE)<sup>8</sup> with elemental Zn and Te sources, in which the Zn and Te cell shutters were alternately opened for 10 seconds with a 10 second pause between each opening. After nucleation, the seed layer was then annealed at 420 °C under Te flux for 10 minutes, followed by deposition of a thick (~6 µm) ZnTe layer onto the seed layer using a ZnTe compound source with additional Te or Zn or neither, depending on the experimental parameters of choice. The growth rate of ZnTe was approximately 0.6 µm/h. During ZnTe growth, the layer was periodically annealed at 460 °C under Te overpressure. This flash annealing improved the ZnTe layer quality. The studies reported here were focused on the substrate pretreatment prior to film growth, as well as the nucleation and growth temperatures for ZnTe, and changes in the Zn/Te flux ratio used during growth.

As-grown ZnTe/Si layers were evaluated for overall crystalline quality by utilizing a PANalytical X'pertProMPD X-ray diffractometer with Cu K $\alpha$  radiation ( $\lambda = 1.5406 \text{ \AA}$ ) and conventional  $\theta$ -2 $\theta$  XRD. The surface morphologies of the as-grown layers were recorded using a phase-contrast optical microscope equipped with a digital camera, and defect densities were determined through direct observation and counting. To determine the dislocation densities of the ZnTe/Si layers, a chemical decoration etch developed by Benson was used to reveal the dislocations.<sup>9</sup> The resulting etch pits, which were associated with the dislocations

generated during growth, were observed and counted using an automated counting program that detected changes in grayscale due to pit presence against the non-pitted surface.

The specimens for cross-sectional transmission electron microscopy (TEM) observation were prepared using standard mechanical polishing and ion-milling procedures with the sample held at liquid-nitrogen temperature to avoid ion-milling artefacts. High-resolution images were recorded with a JEM-4000EX, operated at 400 keV with a structural resolution of  $\sim 1.7$  Å and equipped with a double-tilt, top-entry-type sample holder. Specimens were oriented for TEM observation along the common  $\langle 110 \rangle$  projection. High-angle annular-dark-field (HAADF) imaging and energy-dispersive x-ray spectroscopy (EDXS) were carried out using a JEOL 2010F, equipped with a field-emission electron gun and operated at 200 keV. In this work, the HAADF images were obtained using a focused probe diameter of  $\sim 0.2$  nm, and elemental composition profiles were obtained by operating the microscope in STEM mode with a probe size of  $\sim 1$  nm while scanning the electron probe across the region of interest.



### 3.3 Results and discussion

#### 3.3.1 Growth of ZnTe(211)/Si (211)

For MBE growth, growth temperature is one of the key parameters controlling the quality and morphology of the epilayer. Since ZnTe films were grown on Si substrates using a two-step growth process, i.e., a thin ( $\sim 5$  nm) ZnTe nucleation layer and a thick ( $\sim 6$   $\mu\text{m}$ ) ZnTe epilayer, both the nucleation temperature and the growth temperature were optimized independently. In addition, the Zn/Te flux ratio used during growth of the ZnTe epilayers was also an important parameter. Experiments were designed to change only one variable at a time. Multiple ZnTe/Si layers were grown and analyzed using X-ray full-width at half-maximum (FWHM) to measure overall crystalline quality, etch pit density (EPD) measurements of dislocation density using the Benson etch,<sup>9</sup> and optical microscopy observations of the surface morphology.

##### 3.3.1.1 Optimal nucleation temperature for ZnTe(211)/Si(211)

Figure 3.2 plots the FWHM (right axis) of XRD diffraction spots from (422) planes, and dislocation density (left axis), of as-grown ZnTe(211)/Si(211) layers as a function of the nucleation temperature. All layers nucleated at various temperatures between 260 and 340 °C used the MEE growth process with elemental Zn and Te fluxes, followed by a thick ( $\sim 6$   $\mu\text{m}$ ) ZnTe epilayer growth at

300 °C using a ZnTe compound source. The results indicate that the XRD FWHM of the ZnTe/Si layer is insensitive to the nucleation temperature, but the dislocation density according to EPD measurements suggests an optimal nucleation temperature window of 280 to 320 °C.

Nomarski optical micrographs shown in Figure 3.3 confirm similar relationships between surface morphology and nucleation temperature; in particular, ZnTe/Si nucleated at 300 °C has the best surface morphology. These XRD, EPD, and optical image results point to an optimal nucleation temperature of 300 °C for ZnTe(211) grown on Si(211) substrates by MBE.

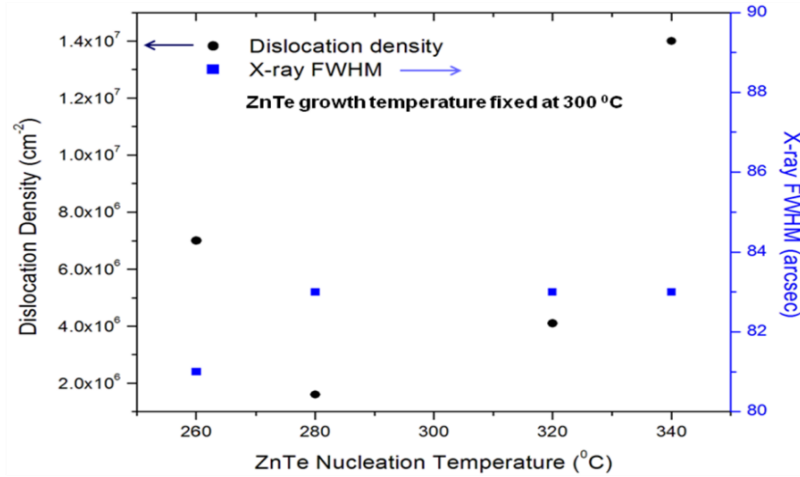


Figure 3.2 XRD FWHM (right axis), and dislocation density (left axis), of as-grown ZnTe/Si(211) layers as a function of nucleation temperature between 260 °C and 340 °C.<sup>1</sup>

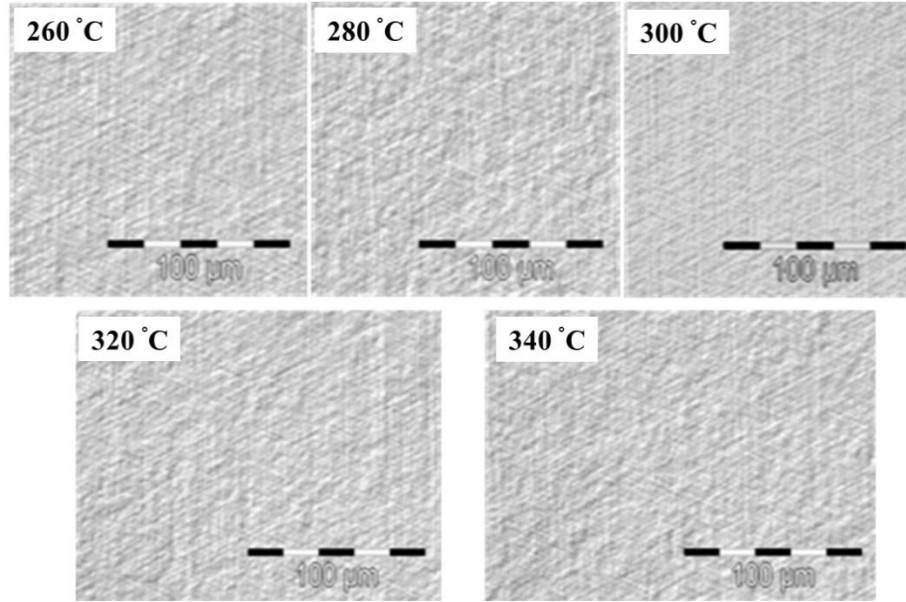


Figure 3.3 Nomarski optical micrographs for as-grown ZnTe(211) films on Si(211) substrates for various nucleation temperatures between 260 °C and 340 °C.<sup>1</sup>

### 3.3.1.2 Optimal growth temperature for ZnTe(211)/Si(211)

The temperature for growth of the ZnTe epilayer on the thin ZnTe nucleation layers was optimized after fixing the nucleation temperature at 300 °C. Thick (~6 μm) ZnTe epilayers were grown on thin (~5 nm) ZnTe layers, which were nucleated at 300 °C on Si substrates, at six different growth temperatures that were changed incrementally by 20 °C from 260 °C to 360 °C. The crystalline quality of the as-grown ZnTe/Si layers as a function of growth temperature was

then evaluated using XRD FWHM and dislocation density, as shown in Figure 3.4, and surface morphology, as shown in Figure 3.5.

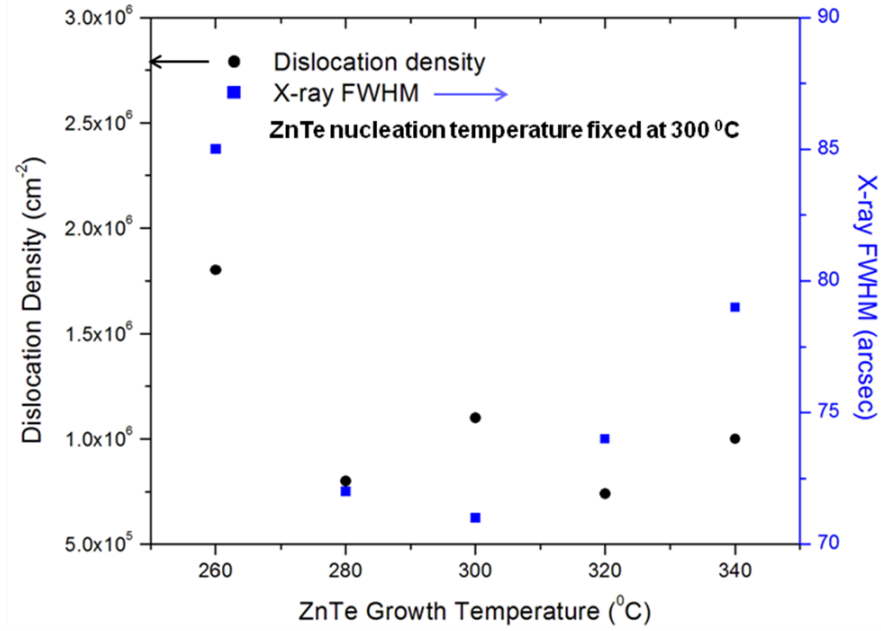


Figure 3.4 XRD FWHM (right axis), and dislocation density (left axis), of as-grown ZnTe(211)/Si(211) layers as a function of growth temperature in the range 260 °C to 340 °C.<sup>1</sup>

The results clearly define an optimal window of growth temperature between 280 and 320 °C. Outside that range, the ZnTe/Si layers display much rougher surfaces and broader XRD FWHM values, indicating the poorer crystallinity of the layers. The surface roughening occurring at both the low end and the high end

of the growth temperature window is probably due to lack of diffusivity at lower temperatures, which promotes a disordered lattice arrangement, and a decrease of the sticking coefficient at higher temperature, which tends to lead to faceting.<sup>1</sup>

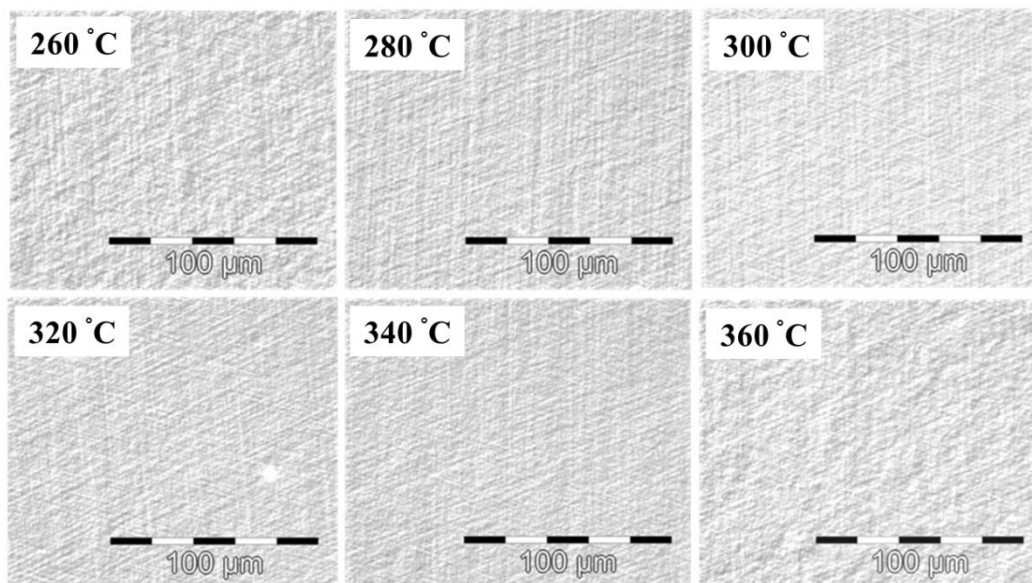


Figure 3.5 Nomarski optical micrographs for as-grown ZnTe(211) films on Si(211) substrates at growth temperatures in the range 260 °C to 360 °C.<sup>1</sup>

### 3.3.1.3 Optimal Zn/Te flux ratio for ZnTe(211)/Si(211)

For heteroepitaxy of binary II-VI compounds, optimized growth conditions are usually achieved with a specific ratio of the II/VII compounds due to different desorption coefficients of the group II and VI elements.<sup>10</sup> In the case of ZnTe,

which is a compound of period 4 (Zn) and period 5 (Te) in the Periodic Table, increased imbalance in the thermodynamic properties of Zn and Te probably leads to increased sensitivity of the surface morphology and crystalline quality of ZnTe layer to the Zn/Te flux ratio. For heteroepitaxial growth of ZnTe(100) on III-V substrates, it was found that the optimized growth conditions were achieved in a Zn-rich growth environment.<sup>8, 11</sup>

The influence of Zn/Te flux ratio on surface morphology and crystalline quality of ZnTe(211)/Si(211) was investigated. All ZnTe layers were nucleated and grown at approximately 300 °C in three consecutive runs under three different II/VI flux ratios of 0.5, 1, and 2, using the growth procedures described previously. Figure 3.6 shows XRD FWHM (right axis) and dislocation density (left axis) as well as the surface morphologies of these three ZnTe(211)/Si(211) layers. The results indicate that ZnTe(211)/Si(211) layers grown under either Zn/Te = 0.5 (Te-rich) or Zn/Te = 1 (equal Zn and Te fluxes) conditions have better crystal quality than those grown under Zn/Te=2 (Zn-rich) condition. In addition, every ZnTe(211) layer grown under the Zn-rich condition exhibits a very hazy surface morphology visible to the unaided eye and they show very broad XRD FWHMs which are a factor of four higher than those of layers grown under Te-rich conditions, as shown in Figure 3.6.

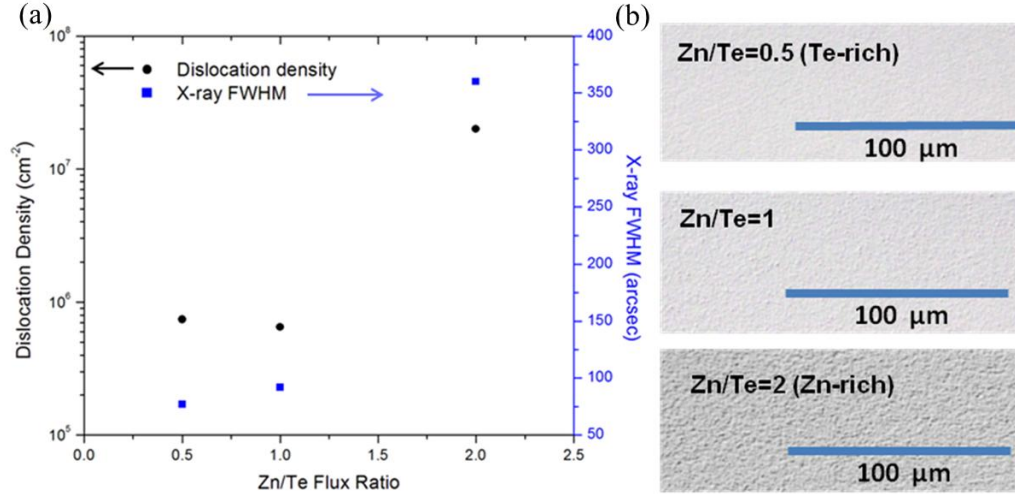


Figure 3.6 (a) XRD FWHM (right axis); and dislocation density (left axis); and (b) optical microscopy images, of as-grown ZnTe(211)/Si(211) layers nucleated and grown at 300 °C with different Zn/Te flux ratios of 0.5, 1, and 2.<sup>1</sup>

### 3.3.2 TEM characterization of ZnTe(211)/Si(211)

The transmission electron microscope (TEM) is a powerful instrument that provides a range of imaging and analytical techniques that are well suited for determining the microstructure and chemistry of ZnTe/Si composite substrates down to the atomic scale. First, the impact of the Zn/Te flux ratio on ZnTe/Si was investigated using TEM, then the microstructure of the interface between ZnTe and Si was also studied using HREM as well as HAADF imaging with EDXS.

### 3.3.2.1 Impact of Zn/Te flux ratio on ZnTe(211)/Si(211)

The impact of Zn/Te flux ratio on ZnTe(211)/Si(211) substrate was studied from cross-sectional electron micrographs, as shown in Figure 3.7. Images from ZnTe(211)/Si(211) under conditions of Te-rich and equal Zn and Te fluxes showed that the misfit dislocation density due to the large lattice mismatch (12.3 %) between ZnTe and Si was high near the ZnTe/Si interface, and then drastically decreased over  $\sim 1 \mu\text{m}$  toward the ZnTe top surface, as shown in Figures 3.7 (a) and (b), respectively. In contrast, the poor film quality of the ZnTe(211) film grown under Zn-rich condition is further evidenced by cross-sectional TEM images. Figures 3.7 (c) and (d) show that there are many lamellar twins in addition to cracks parallel to the growth direction of ZnTe films grown under Zn/Te flux ratio of 2, causing poor crystal quality and surface morphology.



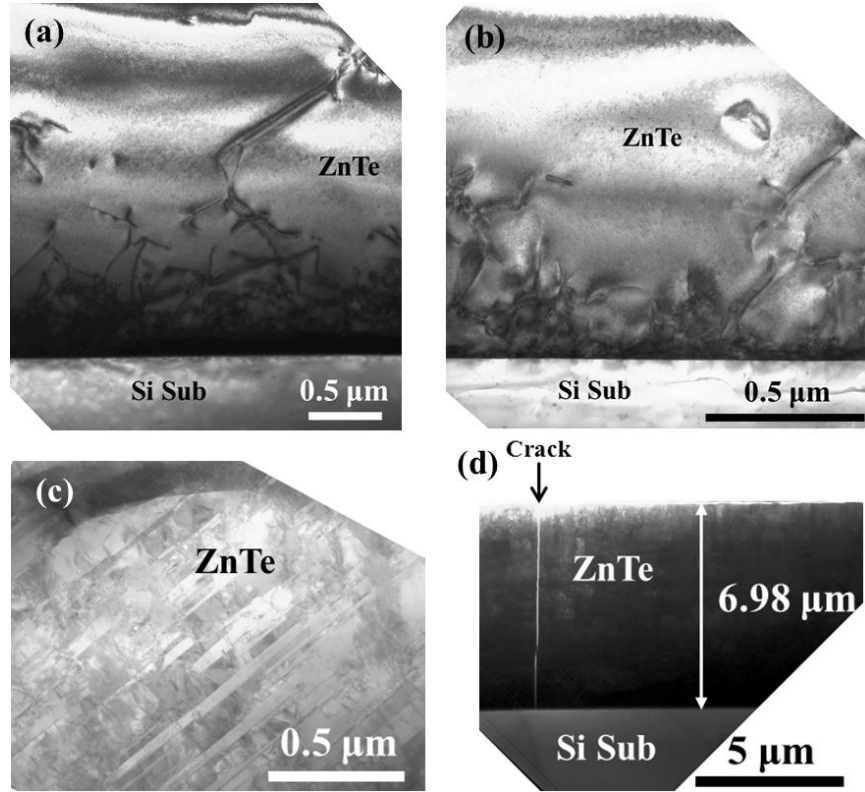


Figure 3.7 Cross-sectional electron micrographs of as-grown ZnTe(211)/Si(211) layers nucleated and grown at  $300\text{ }^{\circ}\text{C}$  with different Zn/Te flux ratios; (a) Zn/Te = 0.5 (Te-rich), (b) Zn/Te = 1 (equal Zn and Te fluxes), and (c) & (d) Zn/Te = 2 (Zn-rich).

### 3.3.2.2 Characterization of ZnTe(211)/Si(211) interface

The higher-index Si surfaces such as Si(211) and Si(311) contain a large number of step-edge sites caused by the large tilt of the misoriented Si surface away from flat (111) terrace planes. For example, a Si(211) surface has two atoms

on (111) terraces for every atom on (100) steps because it is tilted by  $19.4^\circ$  away from the Si (111) surface, as shown in Figure 3.8. The change of this tilt angle directly corresponds with the step density of the surface.

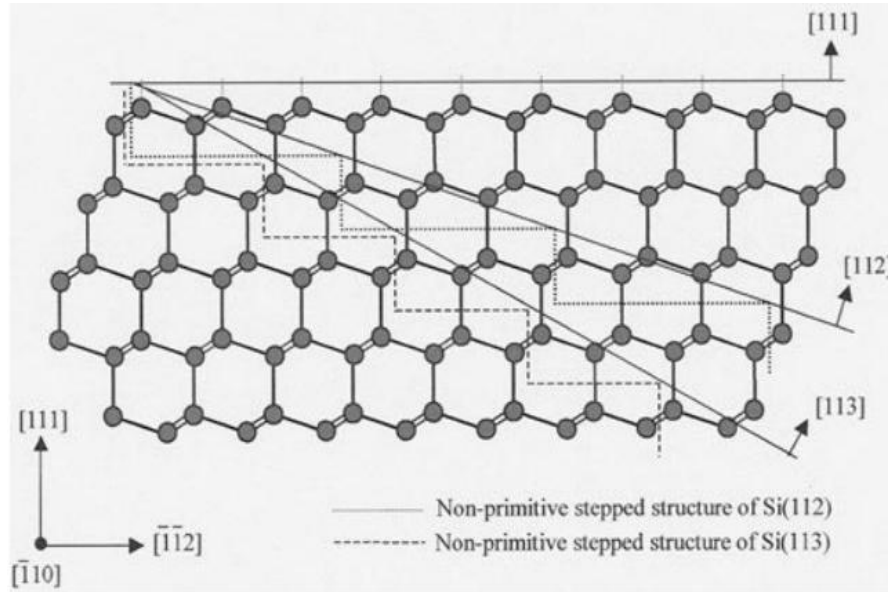


Figure 3.8 Ball-and-stick model of the Si(211) and Si(311) stepped surfaces and their relationship to the Si(111) bulk lattice. The solid and dashed curves representing the Si(211) surface and the Si(113) surface, respectively, have been offset slightly near the top of Si (111). Note that the terrace width decreases as the tilt angle from the (111) plane increases.<sup>12</sup>

Figures 3.9 (a) and (b) show high-resolution electron micrographs of ZnTe(211)/Si(211) interface for growth flux ratios of  $\text{Zn/Te} = 0.5$ , and  $\text{Zn/Te} = 1$ , respectively. The step-shaped interface between ZnTe and Si confirms the features of terraces and steps on the Si(211) surface. Note that the stepped interface will be more clearly observed in the enlarged images of Figures 3.9 (a) and (b), as shown later in Figure 3.12 (a) and Figure 3.13 (b), respectively. Furthermore, Figures 3.9 (a) and (b) illustrate that some regions of the interface seem free of any defects, while Figure 3.10 (a) shows parallel stacking faults visible just above the ZnTe/Si interface and Figure 3.10 (b) shows short structural defects, mostly consisting of  $\{111\}$ -type stacking faults, originating at the Si substrate and typically terminating within less than 50nm. These defects at the interface help to reduce the strain that is caused by the large misfit between ZnTe and Si.

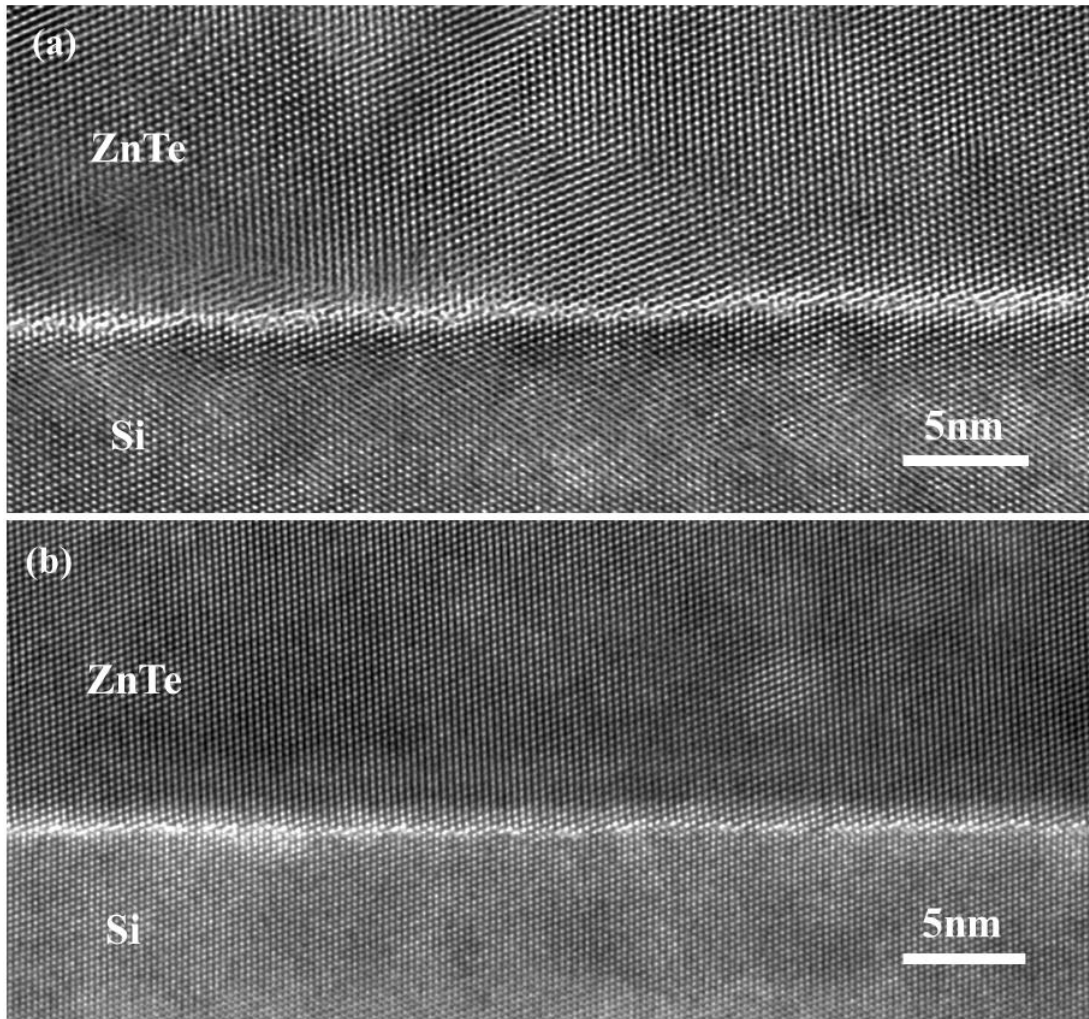


Figure 3.9 High-resolution electron micrographs of: (a) ZnTe(211)/Si(211) interface grown under Te-rich condition; and (b) sample grown under condition of equal Zn and Te flux ratio. Both images show interface regions free from any defects.

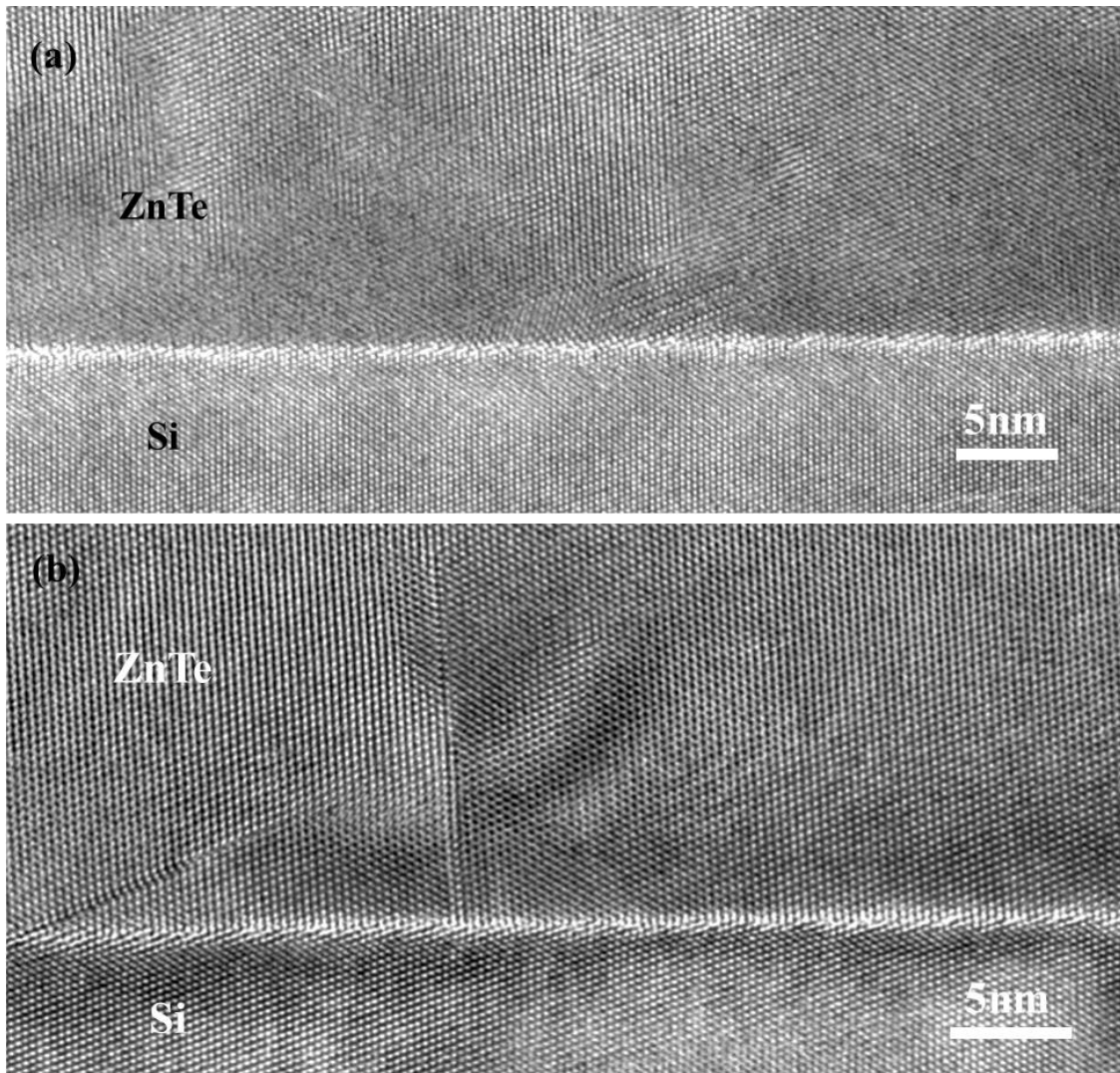


Figure 3.10 High-resolution electron micrographs of: (a) ZnTe(211)/Si(211) interface grown under Te-rich condition; and (b) sample grown under condition of equal Zn and Te flux ratio. Both images show short {111}-type stacking faults originating at the interface.

Diffractograms of the TEM images in Figure 3.9 (a) and (b), respectively, are shown in Figure 3.11. All of the diffracted spots except the central transmitted beam spot appear as a pair. Every inner spot of each pair is from ZnTe having a larger lattice constant than Si, while every outer spot of each pair is from Si. The TEM images in Figure 3.9 were taken at the  $[110]$  zone axis, and diffraction spots, corresponding to specific crystal planes, neighboring the central spot were indexed, as shown in Figure 3.11 (a). Moreover, these diffractograms reveal rotation angles of  $\sim 2.3^\circ$  between the ZnTe epilayer and the Si substrate, measured by the alignment of two (422) diffracted spots with the central spot.

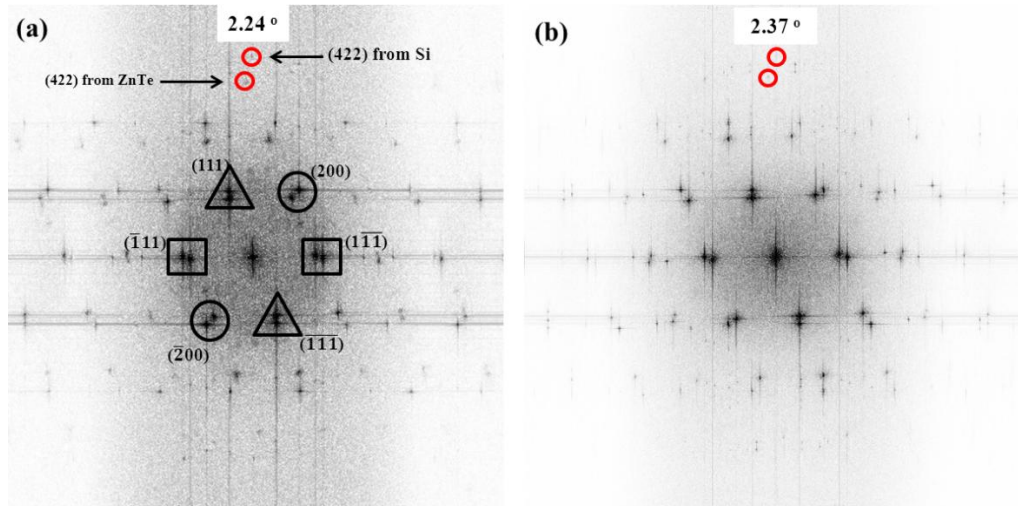


Figure 3.11 Diffractograms of TEM images in Figures 3.9 (a) and (b), respectively.

Figure 3.12 (a) and Figure 3.13 (a) are enlargements of Figure 3.9 (a) and Figure 3.9 (b), respectively, showing atomic structure at the interface between the ZnTe epilayer and the Si substrate. These show the stepped nature of the Si(211) surface and many continuous  $\{111\}$  fringes across the interface. The fast Fourier transform (FFT) technique was used to filter Figure 3.12 (a) and Figure 3.13 (a) to highlight specific lattice fringes and misfit dislocations. Only the  $\{111\}$  reflections marked by the triangles and rectangles in Figure 3.10 (a) were used to obtain the corresponding inverse FFT image. When  $(\bar{1}11)$  and  $(1\bar{1}\bar{1})$  reflections were used by blanking them with masking tools, Figure 3.12 (b) and Figure 3.13 (b) were obtained, with fringes consisting of  $(\bar{1}11)$  planes. They clearly exhibit misfit dislocations identified by the position of the ends of extra half-planes from the Si substrate, as indicated with red arrows. These are distributed evenly along the ZnTe(211)/Si(211) interface, with separations that correspond to the  $\sim 12\%$  lattice mismatch between ZnTe and Si. Thus, these misfit dislocations at the interface relax the strain caused by large lattice mismatch. When  $(111)$  and  $(\bar{1}\bar{1}\bar{1})$  were used in the FFT filtering, Figure 3.12 (c) and Figure 3.13 (c) were obtained, with fringes corresponding to  $(111)$  planes. These show that there are no misfit dislocations on these  $(111)$  fringes because the  $(111)$  planes of both materials are aligned across the interface notwithstanding the large lattice mismatch.



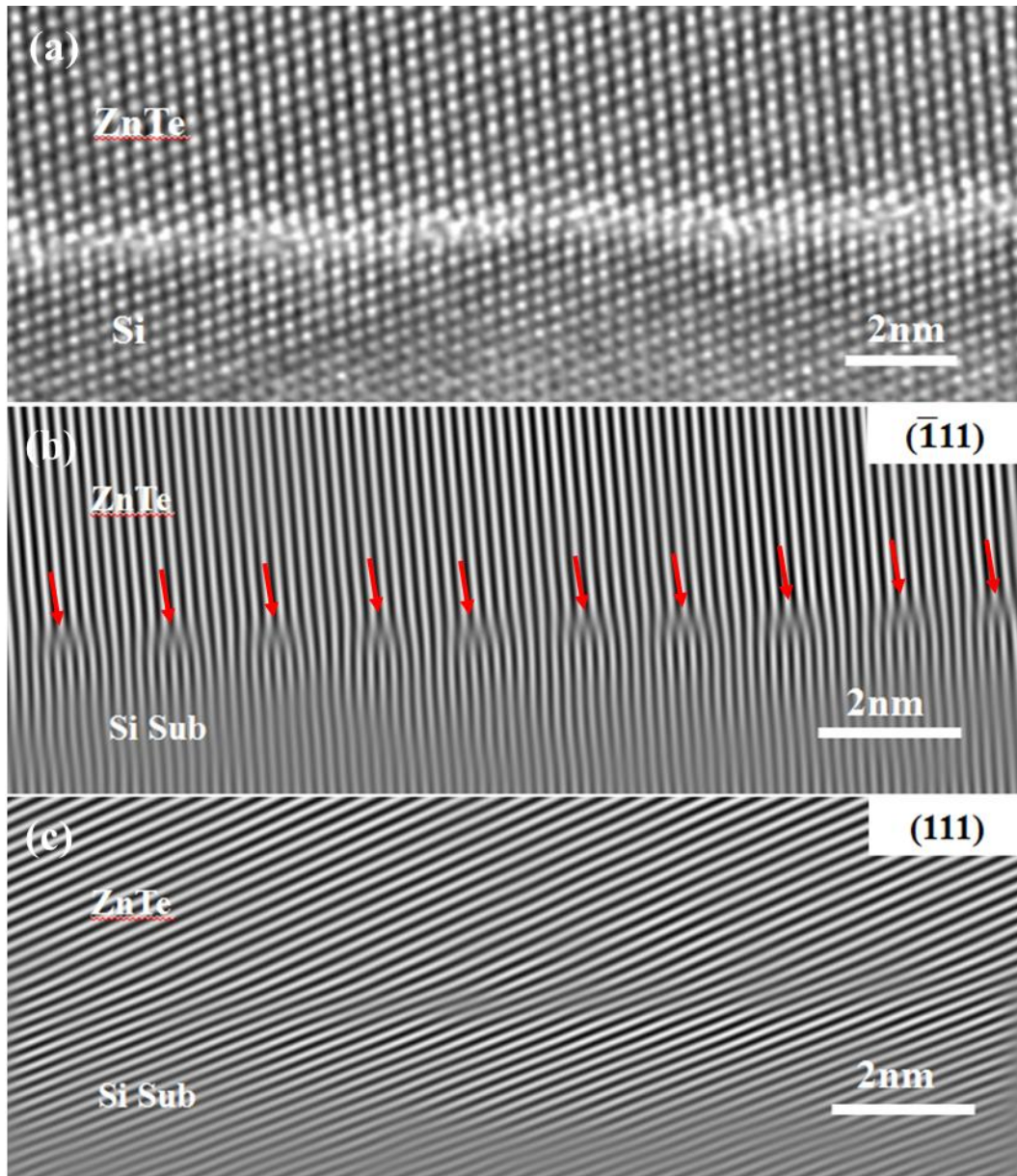


Figure 3.12 (a) Enlarged image of Figure 3.9 (a), showing atomic structure at the ZnTe(211)/Si(211) interface region; (b) inverse FFT image displaying  $(\bar{1}11)$  planes and (c) inverse FFT image displaying  $(111)$  planes.



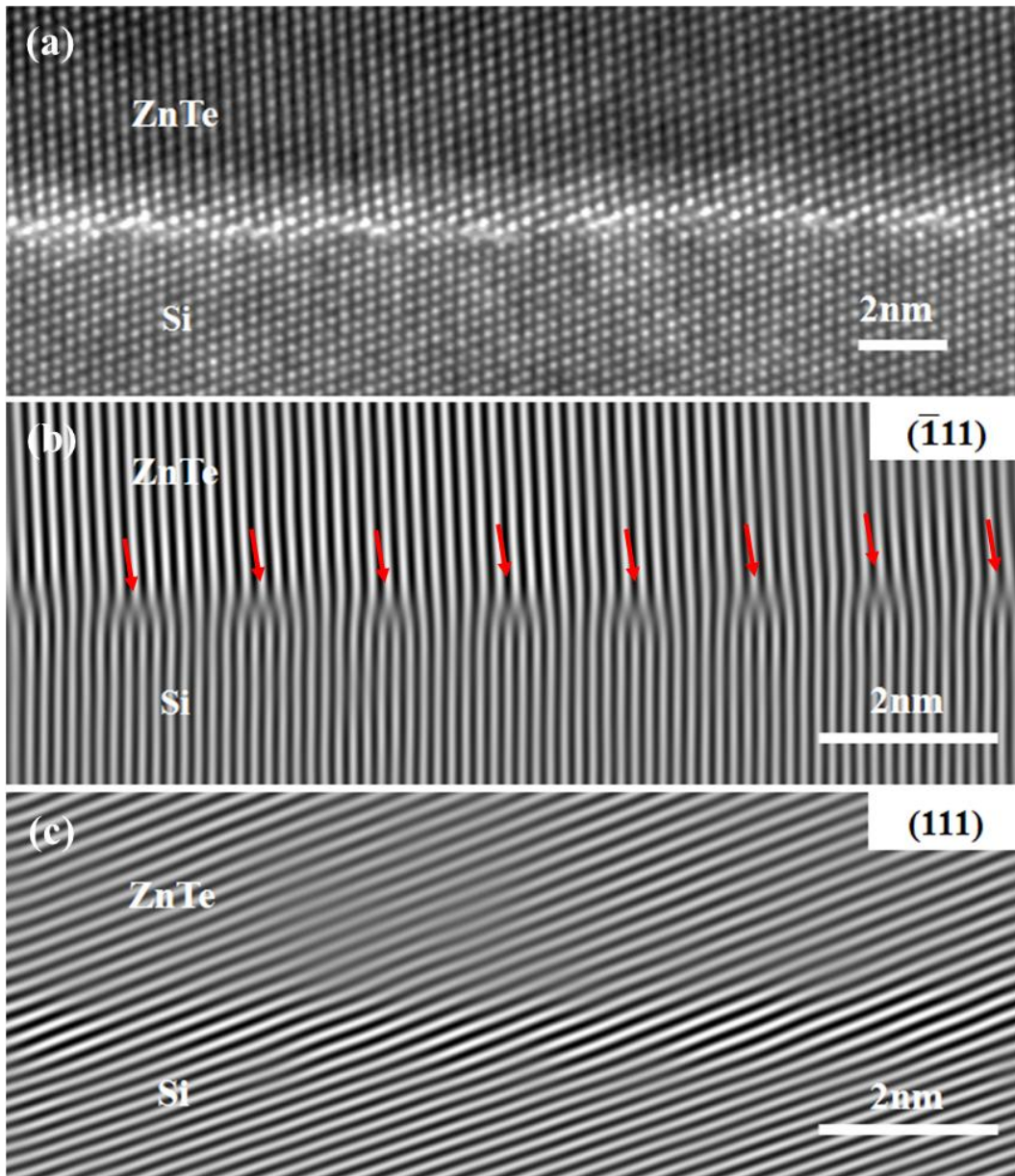


Figure 3.13 (a) Enlarged image of Figure 3.9 (b), showing atomic structure at the ZnTe(211)/Si(211) interface region; (b) inverse FFT image displaying  $(\bar{1}11)$  planes and (c) inverse FFT image displaying  $(111)$  planes.

Compositional analysis was used to determine elemental profiles across the interfaces. Figure 3.14 (a) is an HAADF image for the interface of ZnTe(211)/Si(211) grown under Te-rich conditions, showing the stepped nature of the interface and a much brighter ZnTe epilayer compared with the Si substrate due to the Z-contrast difference. Figure 3.14 (b) shows an EDXS line profile from the arrowed region and Figure 3.14 (c) shows individual spectra taken in turn from three different regions: ZnTe epilayer, ZnTe/Si interface, and Si substrate, as indicated by the numbers 1, 2, and 3. It is clear from the EDXS results that a small amount of residual As is still present at the ZnTe/Si interface, and that As does not diffuse into ZnTe epilayer.

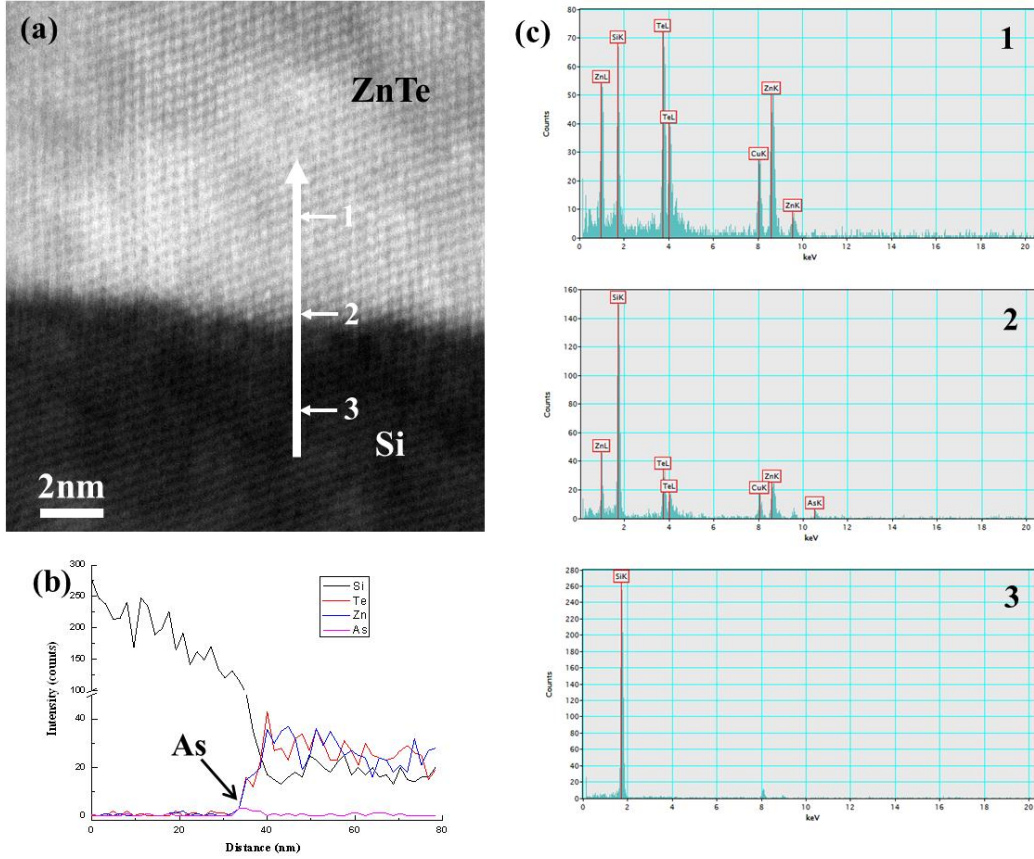


Figure 3.14 (a) HAADF image showing region used for EDXS analysis; (b) elemental profile along line indicated in (a); (c) individual spectra taken in turn at three different positions, as marked with numbers 1, 2, and 3.

### 3.3.3 Growth of ZnTe(100)/Si (100)

It is necessary to develop a baseline growth process for ZnTe(100)/Si(100) since this ZnTe/Si composite substrate could be considered as a potential alternate substrate for T2-SLs, which are currently grown on GaSb(100) substrates.<sup>12</sup> Little

attention has been given to the growth of ZnTe(100) on Si(100) substrates in the past, although there are some limited studies of MBE-grown ZnTe(100) on GaAs as well as other III-V substrates.<sup>13</sup> Analogous to the study of ZnTe(211)/Si(211) reported above, the investigation of ZnTe(100)/Si(100) again started with optimization of the growth parameters by focusing on the impact of pre-nucleation treatment prior to ZnTe nucleation, and the Zn/Te flux ratio used during the growth of ZnTe epilayers. Experiments were again planned to systematically vary just one variable at a time. Multiple ZnTe/Si layers were grown and analyzed using optical microscopy observations of the surface morphology and XRD FWHM was again used to measure overall crystallinity.

#### 3.3.3.1 Optimal pre-nucleation treatment for ZnTe(100)/Si(100)

In order to have a high quality polar epilayer grown on a non-polar substrate, such as ZnTe(100)/Si(100), it is very important to establish a suitable epitaxial template. For this reason, the Si(100) substrates were treated by three pre-nucleation processes (Te flux, Zn flux, and no flux) before the growth of ZnTe nucleation layers were investigated, and the impact of the pre-nucleation treatment on the ZnTe epilayers was studied. Three consecutive MBE runs were carried out under identical nucleation and growth conditions to grow ZnTe(100) layers on Si(100) substrates pre-treated with Zn, Te, or no flux, respectively,

before the growth of ZnTe nucleation layers on Si substrates was initiated. As-grown ZnTe(100)/Si(100) wafers were then evaluated, and the results are illustrated in Figure 3.15.

Figures 3.15 (a) and (b) show XRD FWHM and surface morphology, respectively, indicating that ZnTe(100) layers grown on Si(100) substrates with either Zn or no pretreatment result in very rough surfaces and poor crystalline quality. On the other hand, a ZnTe(100) layer grown with the Te pretreatment shows a much smoother surface and better quality. However, the surface morphology is dominated by dense hillock structures, as shown in Figure 3.15 (b), implying that the growth conditions have still not been optimized. Moreover, the ZnTe(211)/Si(211) layer nucleated and grown at 300 °C can be compared with the ZnTe(100)/Si(100) layer without any pre-nucleation treatment because there is no pre-nucleation treatment on ZnTe(211)/Si(211) layers reported here. XRD FWHM for the ZnTe(100)/Si(100) layer shown in Figure 3.15 (a) is more than three times larger than that for the ZnTe(211)/Si(211) layer shown in Figure 3.4, suggesting that the ZnTe(211)/Si(211) layer has much better crystallinity than the ZnTe(100)/Si(100) layer.

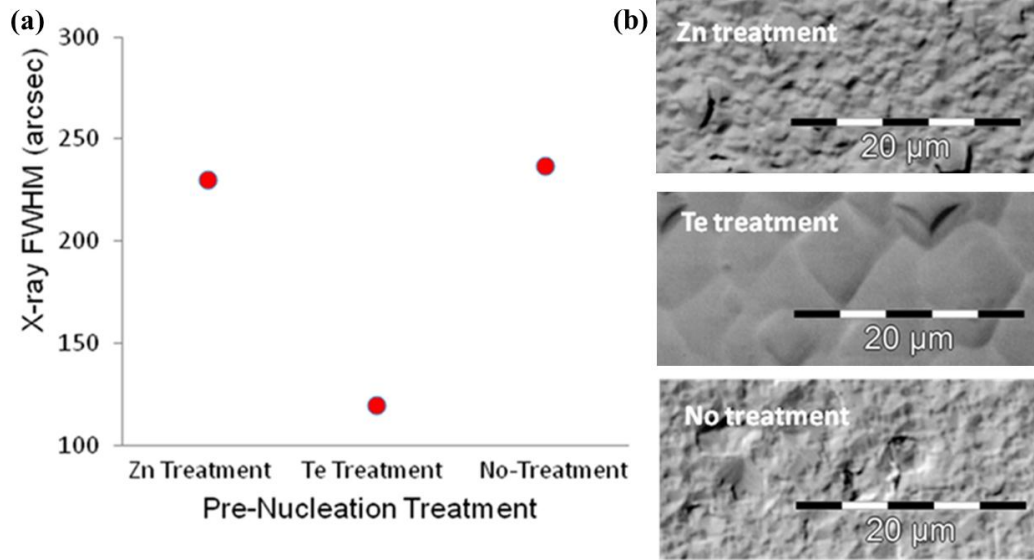


Figure 3.15 (a) XRD FWHM; and (b) Nomarski optical micrographs, of as-grown ZnTe(211)/ Si(211) layers nucleated and grown at 300 °C with different pre-nucleation treatments (Zn-, Te-, and no-treatment).<sup>1</sup>

### 3.3.3.2 Optimal Zn/Te flux ratio for ZnTe(100)/Si(100)

The impact of Zn/Te flux ratio on crystalline quality and surface morphology of ZnTe(100)/Si(100) was studied using the same approach used for ZnTe(211)/Si(211). Three ZnTe(100) layers were grown at 300 °C on Si(100) substrates which were pretreated with Te flux before the growth of ZnTe nucleation layer at 300 °C. Three different Zn/Te flux ratios of 0.5, 1, and 2, respectively were used during the growth. Figures 3.16 (a) and (b) show the XRD FWHM and surface morphology of the three ZnTe(100) layers as a function of

the Zn/Te flux ratio. These results lead to the conclusion that the ZnTe(100) layers need to be grown with a Zn/Te flux ratio of 2 (Zn-rich condition), in line with other reports for ZnTe(100) layers grown on other III-V substrates.<sup>11,13</sup>

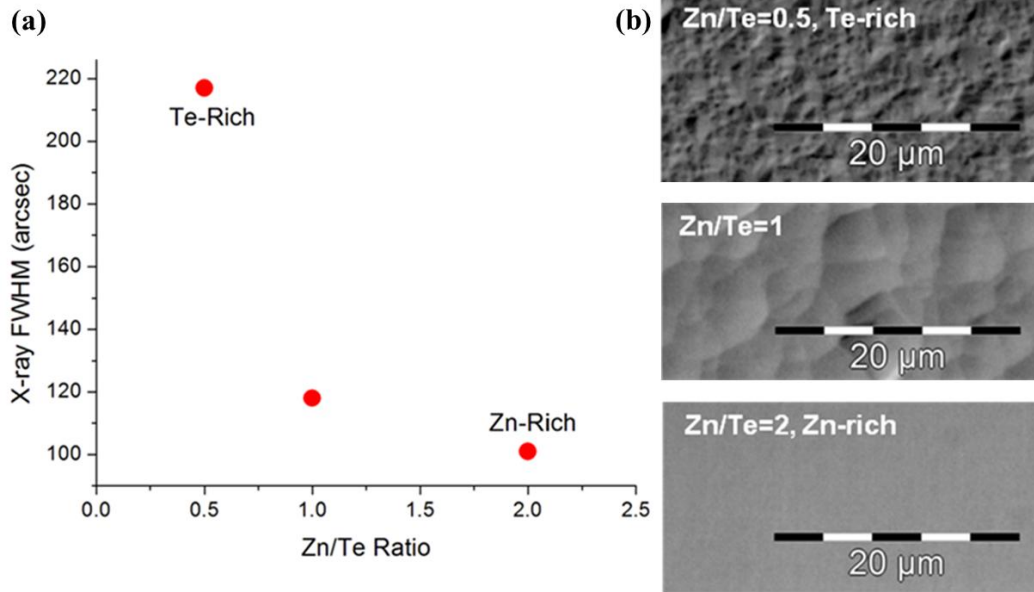


Figure 3.16. (a) XRD FWHM; and (b) Nomarski optical micrographs, of as-grown ZnTe(211)/ Si(211) layers nucleated and grown at 300 °C under with different Zn/Te flux ratios of 0.5, 1, and 2.<sup>1</sup>

### 3.3.4. TEM characterization of ZnTe(100)/Si(100)

#### 3.3.4.1. Impact of Zn/Te flux ratio on ZnTe(100)/Si(100)

Cross-sectional electron micrographs, as shown in Figure 3.17, were used to investigate the impact of the Zn/Te flux ratio on ZnTe(100)/Si(100). All micrographs from three different Zn/Te flux ratio conditions showed that the misfit dislocation density due to the large lattice mismatch (12.3 %) between ZnTe and Si was high near the ZnTe/Si interface. They revealed that the ZnTe(100)/Si(100) samples grown under Te-rich conditions, as shown in Figures 3.17 (a) and (b), seemed to have much higher dislocation density than those grown under the other conditions, as shown in Figure 3.17 (c) to (f). Furthermore, the density of these misfit dislocations decreased moving toward the ZnTe top surface for the ZnTe(100)/Si(100) samples grown under the Zn/Te flux ratio of 1 and 2, while some of those dislocations even reached as far as the top surface for the ZnTe(100)/Si(100) samples grown under the Zn/Te flux ratio of 0.5. The higher defect density observed from the TEM results confirms that the Te-rich ZnTe(100)/Si(100) have poor crystallinity and rough surface morphology, as had been suggested by the XRD and optical micrograph investigations.



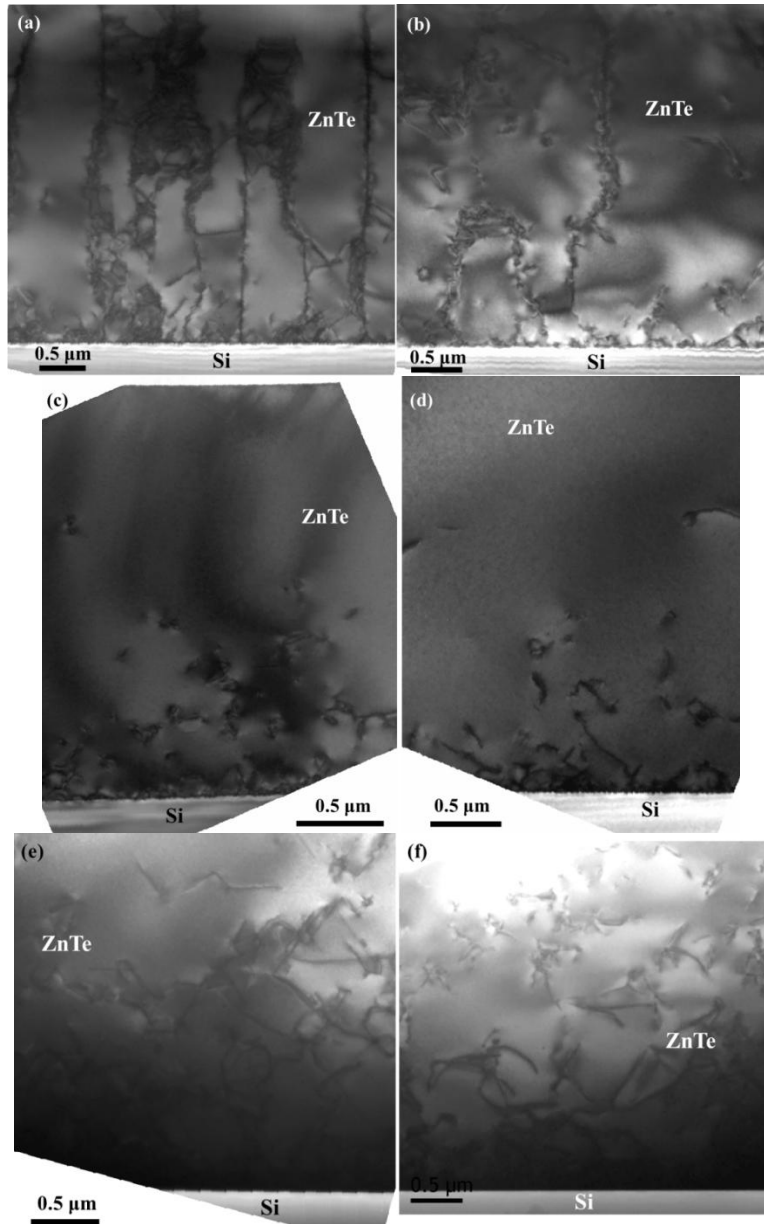


Figure 3.17 Cross-sectional electron micrographs of as-grown ZnTe(100)/Si(100) layers nucleated and grown at 300 °C with different Zn/Te flux ratios; (a) & (b) Zn/Te = 0.5 (Te-rich), (c) & (d) Zn/Te = 1 (equal Zn and Te fluxes), and (e) & (f) Zn/Te = 2 (Zn-rich).

### 3.3.4.2 Characterization of ZnTe(100)/Si(100) interface

Figure 3.18 compares high-resolution electron micrographs of the ZnTe(100)/Si(100) interfaces grown under Zn/Te flux ratios of 0.5 [(a) and (b)], 1 [(c) and (d)], and 2 [(e) and (f)], respectively. Figures 3.18 (a), (c), and (e) illustrate that some regions of the interface seem free of any defects, while Figures 3.18 (b), (d), and (f) show parallel stacking faults visible just above the ZnTe/Si interface, originating at the Si substrate and typically terminating within less than 50nm. These defects accommodate strain at the interface, caused by the large misfit between ZnTe and Si. Furthermore, compared with the results of the ZnTe(211)/Si(211) interface, as shown in Figure 3.9 through Figure 3.13, the interface between ZnTe(100) and Si(100) seems more disordered meaning that the ZnTe(211)/Si(211) interface is more abrupt than the ZnTe(100)/Si(100) one. However, it is difficult to determine distinctive characteristics of ZnTe(100)/Si(100) interfaces grown under three different Zn/Te flux ratio conditions by using only high-resolution electron micrographs, as shown in Figure 3.18.

Figure 3.19 (a) is an HAADF image for the interface of ZnTe(100)/Si(100) grown under Zn-rich condition, showing brighter ZnTe epilayer compared with Si substrate due to the Z-contrast difference. Figure 3.19 (b) shows an EDXS line profile from the arrowed region. It is again apparent that a small amount of As is present at the ZnTe/Si interface, and that As does not diffuse into ZnTe epilayer.

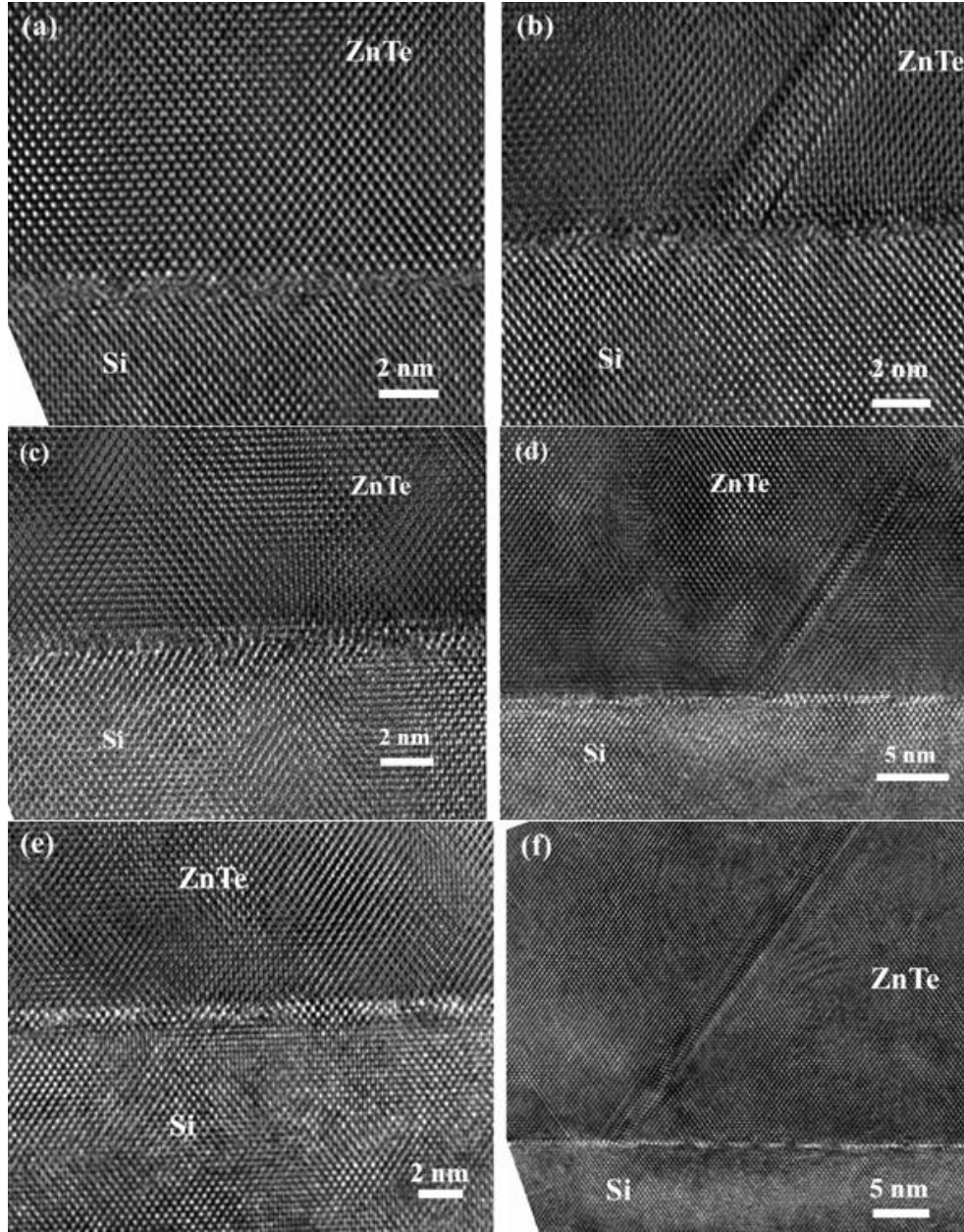


Figure 3.18 High-resolution electron micrographs of ZnTe(100)/Si(100) interface grown under the Te-rich condition in (a) and (b), one grown under the condition of equal Zn and Te flux ratio in (c) and (d), and one grown under the Zn-rich condition in (e) and (f).

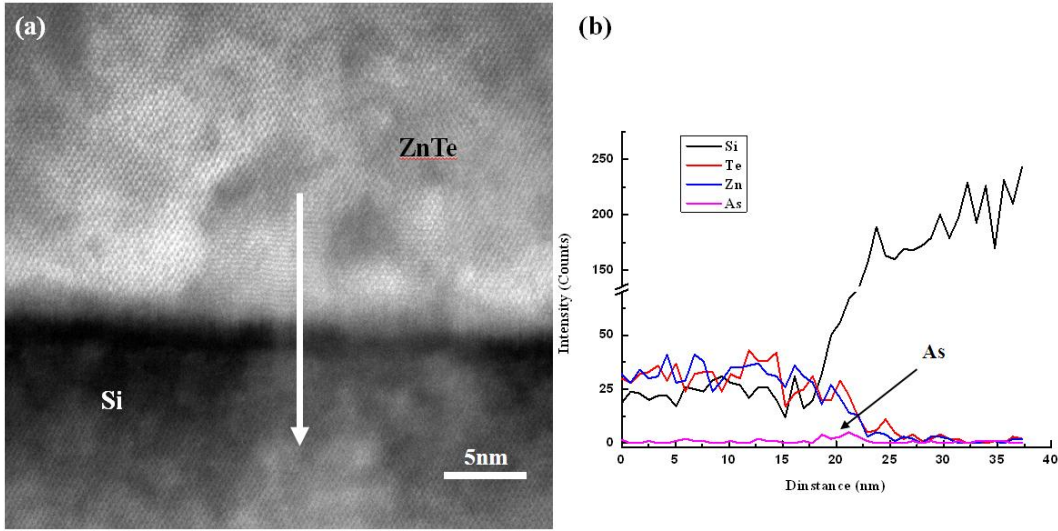


Figure 3.19 (a) HAADF image showing region used for EDXS analysis; (b) elemental profile along line indicated in (a).

### 3.4 Conclusions

This systematic study of MBE growth for both ZnTe(211) on Si(211) and ZnTe(100) on Si(100) demonstrates that these composite substrates should be considered as promising candidates for lattice-matched, large-area, and low-cost composite substrates for growth of II-VI and III-V compound semiconductors with lattice constants near  $6.1 \text{ \AA}$ . The highest crystal quality of ZnTe(211) layers on Si(211) substrates was obtained under conditions of nucleation and growth temperatures at  $300^\circ \text{C}$  with a Zn/Te flux ratio of 0.5 during the growth of ZnTe(211) epilayers, while that of ZnTe(100) layers on Si(100) substrates was

achieved under the conditions of pre-nucleation treatment of Te before the nucleation of ZnTe and a Zn/Te flux ratio of 2 during growth of the ZnTe(100) epilayers. Using these MBE growth conditions, XRD FWHMs for ZnTe(211)/Si(211) and ZnTe(100)/Si(100) were as low as 70 and 100 arcsec, respectively. Moreover, TEM results confirmed that the ZnTe(100)/Si(100) interface was more disordered, compared with the ZnTe(211)/Si(211) interface, and that a small amount of As was present at both interfaces. Further work is needed to determine the degree of Zn-rich conditions, as well as optimized growth temperature for ZnTe(100) on Si(100), in order to achieve the highest possible quality of ZnTe(100)/Si(100) and eventually ZnSeTe(100)/Si(100) wafers.

## REFERENCES

- <sup>1</sup> Y. Chen, S. Simingalam, G. Brill, P. Wijewarnasuriya, N. Dhar, J. J. Kim, and D. J. Smith, *J. Electron. Mater.* 41, 10(2012).
- <sup>2</sup> A. Rogalski, *Rep. Prog. Phys.* 68, 2267 (2005).
- <sup>3</sup> H. S. Kim, E. Plis, J. B. Rodriguez, G. D. Bishop, Y. D. Sharma, L. R. Dawson, S. Krishna, J. Bundas, R. Cook, D. Burrows, R. Dennis, K. Patnaude, A. Reisinger, and M. Sundaram, *Appl. Phys. Lett.* 92, 183502 (2008).
- <sup>4</sup> G. Brill, Y. Chen, and P. Wijewarnasuriya, *J. Electron. Mater.* 40, 1679 (2011).
- <sup>5</sup> G. Brill, Y. Chen, P. Wijewarnasuriya, and N. Dhar, *Proc. SPIE* 7419 74190L-1 (2009).
- <sup>6</sup> Y. P. Chen, G. Brill, and N. K. Dhar, *J. Cryst. Growth*, 252, 270 (2003).
- <sup>7</sup> W. Kern, and D. A. Poutinen, *RCA Rev.* 31 (1970).
- <sup>8</sup> N. K. Dhar, C.E.C. Wood, A. Gray, H. Y. Wei, L. Salamanca-Riba, and J. H. Dinan, *J. Vac. Sci. Technol. B* 14, 2366 (1996).
- <sup>9</sup> J. D. Benson, P. J. Smith, R. N. Jacobs, J. K. Markunas, M. Jaime-Vasquez, L. A. Almeida, A. J. Stoltz, L. O. Bubulac, M. Groenert, P. S. Wijewarnasuriya, G. Brill, Y. Chen, and U. Lee, *J. Electron. Mater.* 38, 1771 (2009).
- <sup>10</sup> H. Nishino, T. Saito, and Y. Nishijima, *J. Cryst. Growth* 165, 227-232 (1996).
- <sup>11</sup> H. Nishino, T. Saito, Y. Nishijima, *J. Cryst. Growth* 165, 27 (1996).
- <sup>12</sup> A. Y. Lew, E. T. Yu, Y. H. Zhang, *J. Vac. Sci. Technol. B*, 14, No. 4, 2940 (1996).

- <sup>13</sup> J. Fan, L. Ouyang, X. Liu, D. Ding, J. K. Furdyna, D. J. Smith, Y.-H. Zhang, J. Cryst. Growth, 323, 127 (2011).

## Chapter 4

MICROSTRUCTURAL CHARACTERIZATION OF  
HgCdTe/CdTe GROWN ON GaAs(211)B SUBSTRATES

This chapter describes the microstructural study of HgCdTe/CdTe/GaAs (211)B and CdTe/GaAs(211)B heterostructures as part of ongoing research into the development of improved HgCdTe detectors and devices. This investigation was carried out in collaboration with Dr. Randy Jacobs and colleagues at U.S. Army RDECOM, CERDEC Night Vision and Electronic Sensors Directorate (Fort Belvoir, VA) who provided the materials. Results from this collaborative research have recently been submitted for publication.<sup>1</sup>

## 4.1 Introduction

HgCdTe is the dominant material for infrared sensing and imaging, and is usually grown on bulk lattice-matched CdZnTe (CZT) substrates. There have been significant efforts over the past several decades to identify substrate materials alternative to lattice-matched CZT because of several drawbacks including lack of large substrate areas and high fabrication costs.<sup>2-9</sup> As a result, composite substrates consisting of CdTe epilayers grown on Si,<sup>2-6</sup> Ge,<sup>7</sup> GaAs,<sup>8</sup> and InSb<sup>9</sup> substrates have been investigated because of their greater robustness, lower cost, higher thermal conductivity, greater lateral uniformity, and larger possible area compared with the bulk CZT substrates.



These alternative substrates have inherent material properties that introduce significant obstacles for subsequent HgCdTe growth. The most challenging problem for Si, Ge, and GaAs substrates is their lattice mismatch with HgCdTe or CdTe layers, as shown in Table 4.1. These lattice mismatches lead to two orders of magnitude higher threading dislocation density in HgCdTe layers, compared with that of HgCdTe grown on bulk CZT substrates.<sup>10</sup> Their thermal mismatch with HgCdTe or CdTe layers is also largely responsible for the residual stress during growth, although they appear to have little effect on threading dislocation density.<sup>11</sup> It seems possible that InSb is an excellent choice, because of its near-perfect lattice and thermal matching to HgCdTe or CdTe layers. However, obstacles for InSb substrates are poor IR transmission properties, limited size, and difficult surface preparation.<sup>12</sup> Moreover, since In is used as an *n*-type dopant in HgCdTe devices, there could be possible In diffusion into the HgCdTe layer.

Material	Lattice parameter (Å)	Lattice misfit % from CdTe	CTE (e <sup>-6</sup> /K)	CTE % from CdTe
CdTe	6.482	0	5.0	0
Si	5.431	19.35	2.6	-92.3
Ge	5.646	-14.81	5.9	15.3
GaAs	5.653	-14.66	6.9	27.5
InSb	6.479	-0.05	5.4	7.4

Table 4.1 Lattice constants and coefficients of thermal expansion (CTE) of selected semiconductor materials.<sup>10</sup>

The CdTe/GaAs system is being revisited due to the availability of epi-ready GaAs(211)B wafers, and recent progress in HgCdTe devices grown on GaAs substrates.<sup>13</sup> In this present study, samples of HgCdTe/CdTe/GaAs(211)B and CdTe/GaAs(211)B were grown using molecular beam epitaxy (MBE), and their microstructure was investigated using a wide range of TEM imaging and analytical techniques, including high-resolution electron microscopy (HREM), high-angle annular-dark-field (HAADF) imaging, and energy-dispersive X-ray spectroscopy (EDXS). In addition, interfacial misfit dislocations for CdTe/GaAs(211)B were analyzed using strain relaxation estimation, and in the case of HgCdTe/CdTe/ GaAs(211)B, thin HgTe buffer layers between HgCdTe and CdTe were investigated to improve the crystal quality of HgCdTe layer.

#### 4.2 Experimental details

Commercially available 3-inch GaAs(211)B substrates were loaded into the MBE chamber and heated to the native oxide desorption temperature (580 °C) under an As<sub>4</sub> overpressure.<sup>4</sup> The substrates were then cooled for a low-temperature CdTe nucleation step followed by annealing. In an effort to encourage interaction and annihilation of threading dislocations, subsequent annealing cycles were implemented at regular intervals throughout the remainder of the CdTe growth. A typical growth cycle consisted of deposition of 1 μm of CdTe followed by Te-stabilized annealing for 5 min. Ramp rates were typically

0.5°C/min. The CdTe thickness typically ranged from 9  $\mu\text{m}$  to 13  $\mu\text{m}$ . After CdTe buffer growth, the CdTe/GaAs composite substrate was transferred *in vacuo* to a second MBE chamber for the HgCdTe growth.

Initiation of HgCdTe growth took place after a brief period of annealing at  $\sim 300^\circ\text{C}$ . The purpose of this step was to eliminate any species that might have adsorbed on the CdTe surface during vacuum transfer. A 1- $\mu\text{m}$ - to 1.5- $\mu\text{m}$ -thick HgCdTe buffer layer was then grown, followed by a  $\sim 6\text{-}\mu\text{m}$ - to 8- $\mu\text{m}$ -thick  $\text{Hg}_{0.77}\text{Cd}_{0.23}\text{Te}$  absorber layer. The intent of the HgCdTe buffer layer was to provide a material with an intermediate lattice parameter between the CdTe buffer and  $\text{Hg}_{0.77}\text{Cd}_{0.23}\text{Te}$  absorber layers. Finally, a 0.5- $\mu\text{m}$ -thick protective cap layer ( $x \approx 0.3$ ) was grown. Spectroscopic ellipsometry was used during HgCdTe growth for control of composition and temperature. The nominal HgCdTe growth temperature was  $185^\circ\text{C}$ .

Samples suitable for transmission electron microscope observation were prepared in the cross-sectional geometry using standard mechanical polishing to thicknesses of about 5-10  $\mu\text{m}$ , followed by argon-ion-milling at liquid nitrogen temperature to avoid any ion-milling-induced artefacts.<sup>14</sup> Low-angle, low-voltage (approximately 1.8 keV) milling was used for final thinning to minimize the formation of any amorphous surface or interfacial layers. The electron microscopy observations were mostly carried out using a JEOL JEM-4000EX high-resolution electron microscope (HREM), operated at 400keV and equipped

with a double-tilt, top-entry-type specimen holder. HAADF or “Z-contrast” imaging and EDXS analysis were carried out using a JEOL 2010F, equipped with a field-emission electron gun and operated at 200keV. Samples were usually oriented for TEM observation along the common  $\langle 110 \rangle$  projection.

## 4.3 Results and discussion

### 4.3.1 TEM characterization of CdTe/GaAs(211)B

Figure 1 (a) illustrates a cross-sectional electron micrograph of a 9.6- $\mu\text{m}$ -thick CdTe film grown on a GaAs(211)B substrate, showing excellent crystallinity and a relatively flat top surface. Misfit dislocation density is high near the interface, and then decreases dramatically over  $\sim 2 \mu\text{m}$  moving away from the interface. Figure 1 (b) reveals high defect density just above the CdTe/GaAs(211)B interface with strain-related contrast caused by misfit dislocations at the interface because of lattice mismatch between CdTe and GaAs (14.66%). The small black spots in the CdTe layer are from ion-milling damage.

High-resolution electron micrographs of the CdTe/GaAs interface, as shown by the example in Figure 2, confirm that high quality CdTe epitaxial growth can be achieved on GaAs substrates. The GaAs(211) surface is composed of (111) terraces and (100) edges that allow a step-flow growth mechanism, leading to reduced twinning and antiphase domain formation.<sup>15</sup> Moreover, many of the vertical (111) fringes across the interface are continuous but slightly bent. Using

fast Fourier Transform (FFT) techniques, it was determined that the rotation angle between the CdTe epilayer and the GaAs substrate was  $\sim 2.6^\circ$ .

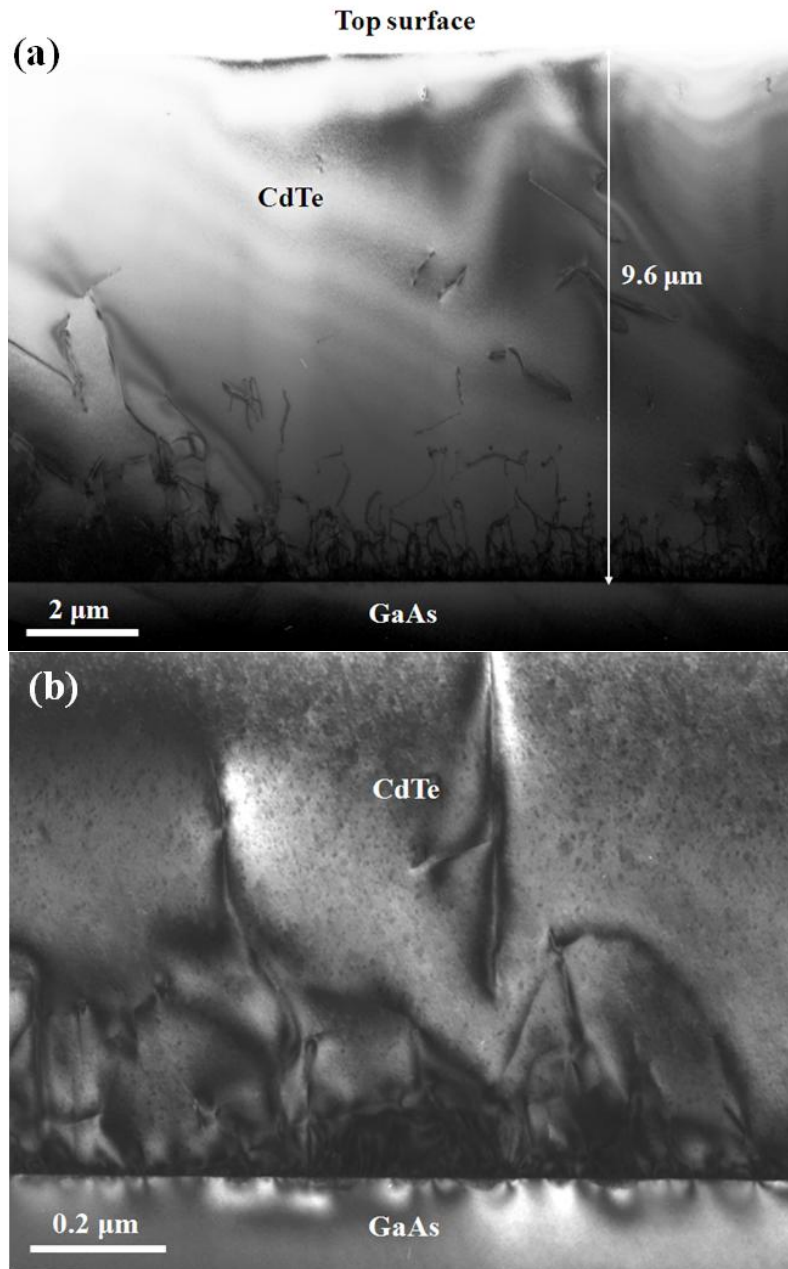


Figure 4.1 Cross-sectional electron micrographs: (a) entire CdTe layer grown on GaAs(211)B; and (b) region close to CdTe/GaAs(211)B interface.

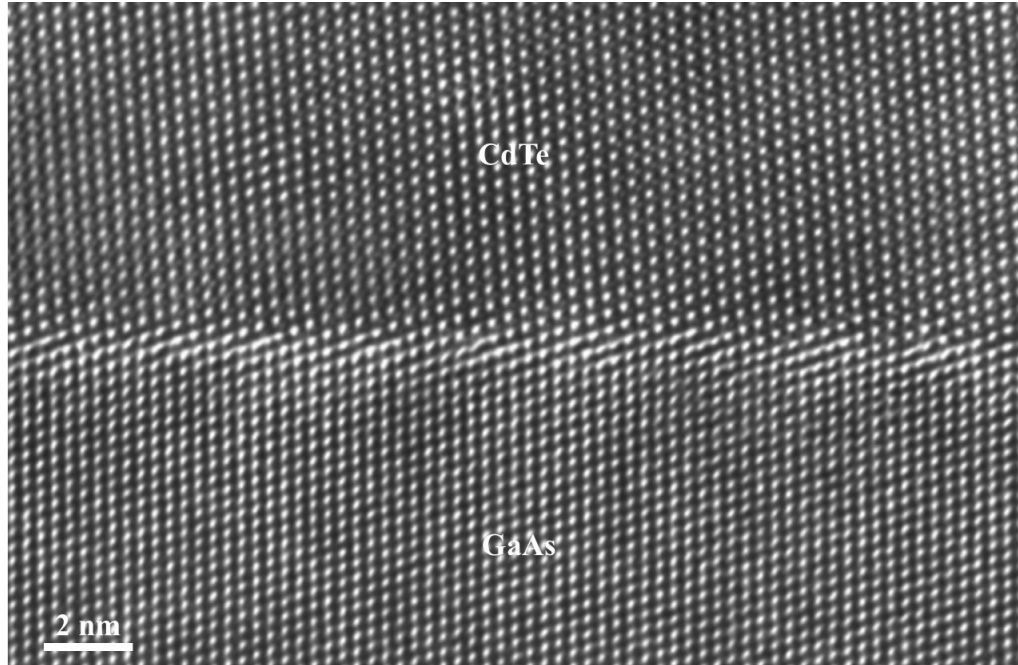


Figure 4.2 High-resolution electron micrograph of CdTe/GaAs(211)B interface.

In order to gain more insight into relaxation of interfacial strain, a quantitative analysis of the distribution of misfit dislocations at the CdTe/GaAs(211)B interface was carried out. Lattice images of the CdTe/GaAs(211)B were digitized and subjected to FFT processing. The FFT patterns were then appropriately filtered by selecting only specific  $\{111\}$  diffraction spots for the inverse FFT images. These filtered images contained information about the location and type of the interfacial misfit dislocations. A  $60^\circ$  dislocation is identified when only one  $\{111\}$  plane terminates at the interface, whereas a Lomer edge dislocation is found when two corresponding  $\{111\}$  planes terminate at the same position.<sup>16</sup>

The inset in Figure 4.3 (a) shows the FFT pattern of the digitized lattice image of CdTe/GaAs(211)B interface, as shown in Figure 4.3 (a). When only the  $\{111\}$  diffraction spots marked by the circles are selected for the inverse FFT image, Figure 4.3 (b) is obtained; and Figure 4.3 (c) is obtained by selecting only diffraction spots marked by the triangles. These inverse FFT images identify five  $60^\circ$  dislocations and no Lomer edge dislocation in this interface region because only one  $\{111\}$  plane terminates at the interface. Using this identification method for about  $0.11\mu\text{m}$  of the CdTe/GaAs(211)B interface, the ratio of Lomer edge dislocations to total number of dislocations is found to be only 2.4 %.

The magnitude of the residual interface strain ( $\epsilon_r$ ) present after relaxation can be estimated from the distribution and the type of misfit dislocations, using  $\epsilon_r = \epsilon_{||} + \delta$ . In case of a pseudomorphic strained layer, the biaxial compressive strain ( $\epsilon_{||}$ ) in CdTe epilayer would be equal to lattice mismatch ( $f$ ) which is  $(a_{\text{GaAs}} - a_{\text{CdTe}})/a_{\text{CdTe}}$ , where  $a_{\text{GaAs}}$  and  $a_{\text{CdTe}}$  are the lattice constants of GaAs and CdTe, respectively. If an array of misfit dislocation is created, the elastic strain ( $\delta$ ) is reduced by  $\delta = \mathbf{b} \cdot \mathbf{e} <111>/d$ , where  $\mathbf{b}$  is the Burgers vector of the misfit dislocation,  $\mathbf{e} <111>$  is the unit vector along the  $<111>$  direction, and  $d$  is the average separation between the misfit dislocations.<sup>17-19</sup> The length of the Burgers vector is  $\frac{1}{2} a_{\text{GaAs}} <110>$  which is  $3.9974 \text{ \AA}$ , and the average separation between dislocations is determined to be  $24.9 \text{ \AA}$  by counting the number of dislocations along about  $0.11\mu\text{m}$  of the CdTe/GaAs(211)B interface. Based on these numbers,

the residual interfacial strain can then be estimated to be about 0.01 % for the CdTe/GaAs(211)B interface, meaning that the interface can effectively be considered as being fully relaxed.

Figure 4.4 (a) shows a high-resolution electron micrograph of a region of the CdTe/GaAs(211)B interface with a small pit. The image confirms high quality epitaxial CdTe growth on the GaAs substrate, although {111}-type stacking faults are visible, originating at the interface and typically terminating within 30 nm.

Using FFT techniques, a quantitative analysis of the distribution of misfit dislocations for the ~ 65-nm region of the interface shown in Figure 4.4 (a) was carried out. Figures 4.4 (b) and (c) display inverse FFT images obtained by selecting only the {111} diffraction spots. Three Lomer edge dislocations and no 60° dislocations are identified because two corresponding {111} planes terminate at the same position. Using this identification method for ~ 65-nm length of the interface shown in Figure 4.4 (a), the ratio of Lomer edge dislocations to total number of dislocations is found to be 73 %, much higher than that in the flat region shown in Figure 4.3 (a). Moreover, the average distance between the misfit dislocations is 16.7Å, much shorter than that of the previous flat region. With these numbers, the estimated remaining residual strain for the pit interface region is only 6.7%. Even though there are more Lomer edge dislocations, which are regarded as more efficient for reducing strain across the interface because of



having two  $60^\circ$  equivalent dislocations components, the pit interface region still contains a significant amount of residual strain.

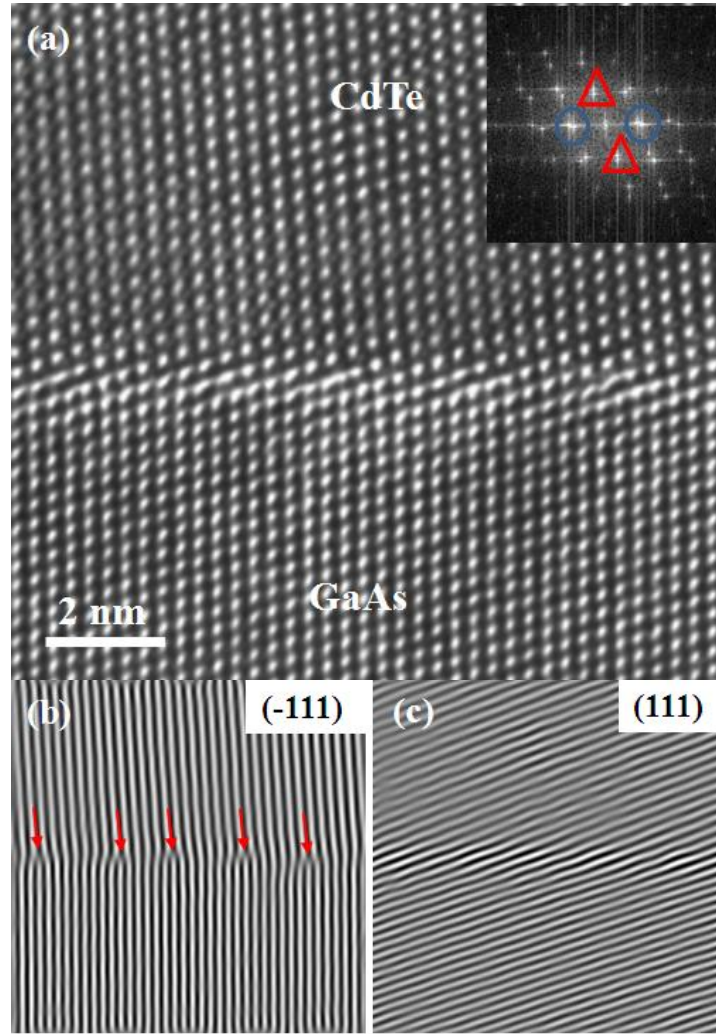


Figure 4.3 (a) Digitized lattice image of the CdTe/GaAs(211)B interface: inset shows FFT pattern of image; (b) Inverse FFT image obtained by selecting  $\{111\}$  diffraction spots marked by circles; (c) Inverse FFT image obtained by selecting  $\{111\}$  diffraction spots marked by triangles.

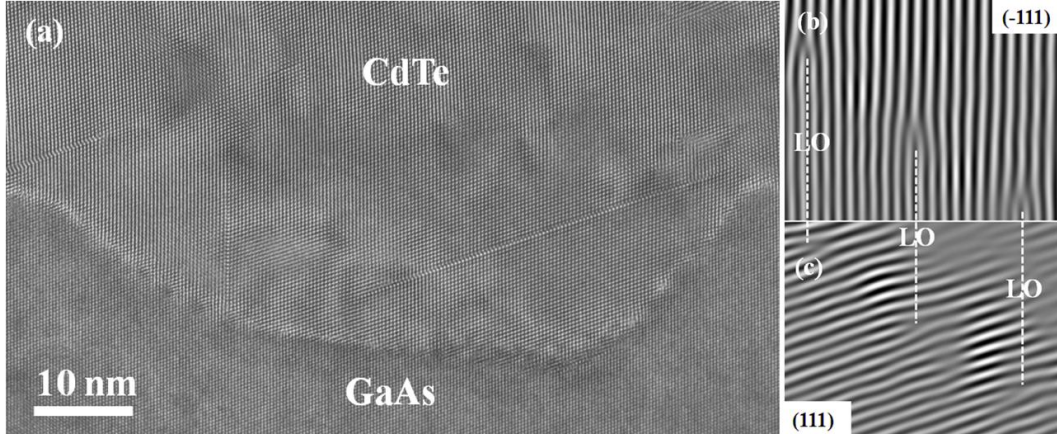


Figure 4.4 (a) High-resolution electron micrograph of pit region of the CdTe/GaAs(211)B interface; (b) Inverse FFT image obtained by selecting  $(\bar{1} 11)$  and  $(1\bar{1}\bar{1})$  diffraction spots; (c) Inverse FFT image obtained by selecting  $(111)$  and  $(\bar{1}\bar{1}\bar{1})$  diffraction spots.

The quality of the CdTe top surface is very important because CdTe/GaAs composite substrates are being considered to serve as a platform for HgCdTe growth. The epoxy region above the CdTe top surface, which holds two cross-sectional specimens, is shown in Figures 4.5 (a) and (b). Figure 4.5 (b) shows an enlargement of the boxed region shown in Figure 4.5 (a), indicating high CdTe crystallinity near the top surface. Moreover, there are no signs of any precipitates or stacking faults near the top surface, which could affect the quality of any HgCdTe epilayer grown on CdTe/GaAs(211)B.<sup>20</sup>

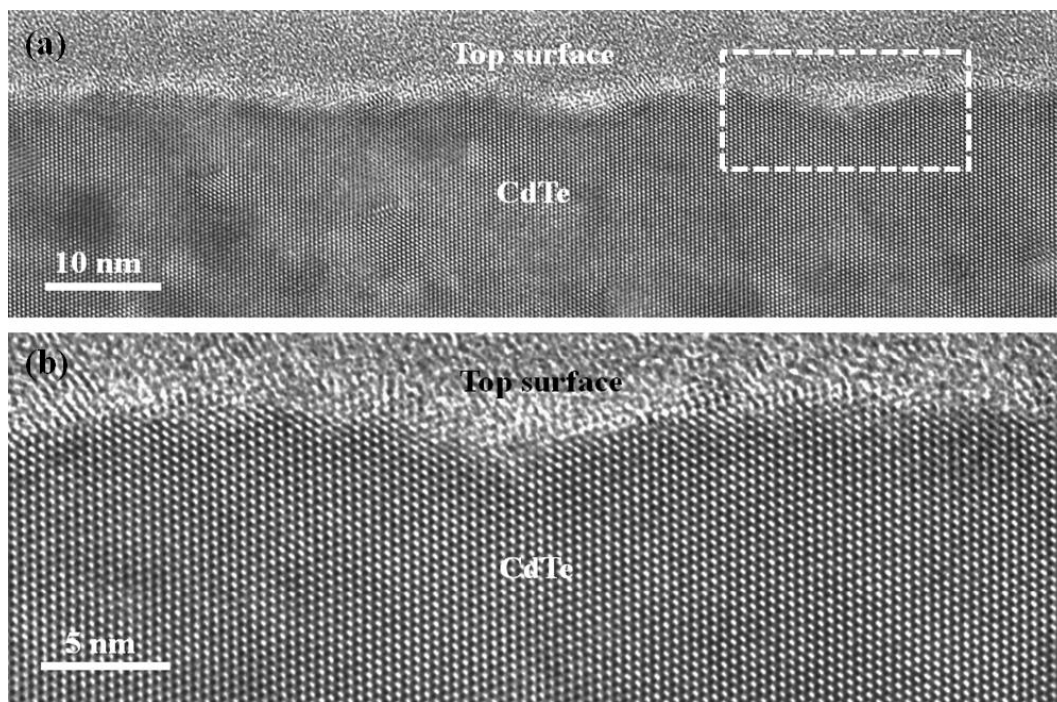


Figure 4.5 (a) High-resolution electron micrograph near the top surface of CdTe layer, and (b) enlargement of CdTe layer from the boxed region indicated in (a).

Compositional analysis was also used to determine elemental profiles. Figure 4.6 (a) is a HAADF image of the CdTe/GaAs(211)B interface, showing the stepped nature of the interface and a much brighter CdTe epilayer compared with GaAs substrate because of the Z-contrast difference. Figure 4.6 (b) shows an EDXS line profile from the arrowed region, and Figure 4.6 (c) displays individual EDXS spectra taken from the CdTe and GaAs regions. The Z-contrast image was obtained using a small probe ( $\sim 0.2$  nm), while a relatively large probe size ( $\sim 1$  nm) was used for acquiring the EDXS analysis. From these HAADF and EDXS

results, it is clear that the interface is reasonably abrupt chemically as well as structurally.

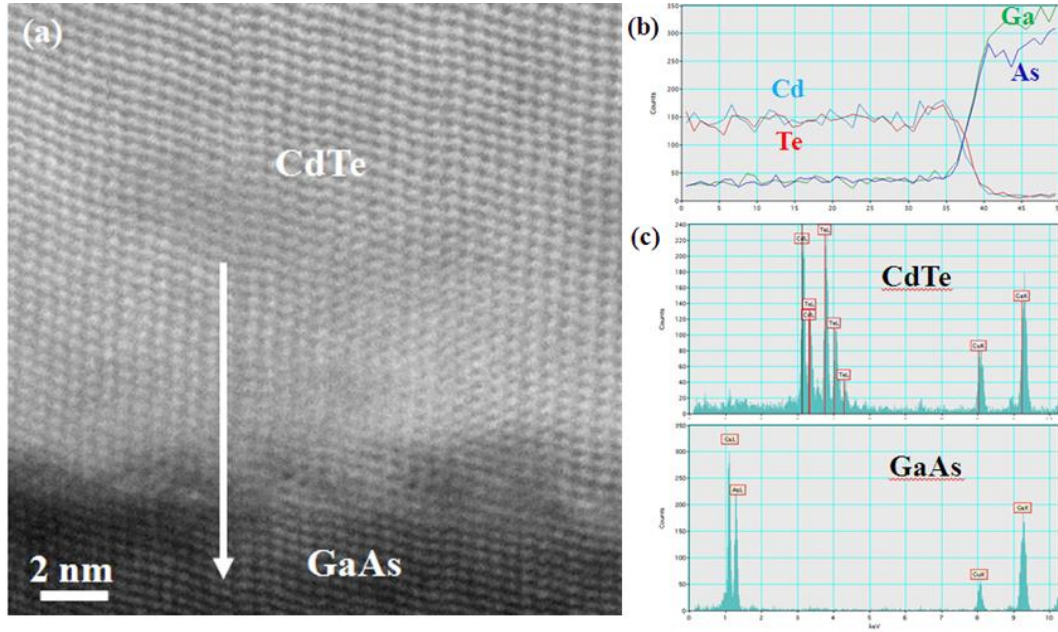


Figure 4.6 (a) HAADF image showing region used for analysis; (b) EDXS elemental profile along the arrow region indicated in (a); (c) individual spectra taken at CdTe and GaAs.

#### 4.3.2 TEM characterization of HgCdTe/CdTe/GaAs(211)B

HgCdTe layers grown on high quality of CdTe/GaAs(211)B composite substrates were characterized using TEM. The cross-sectional electron micrographs shown in Figure 4.7 (a) confirmed that high quality HgCdTe could be achieved on CdTe/GaAs(211)B composite substrate and that the top surface of

HgCdTe layer and the HgCdTe/CdTe interface were reasonably flat. Meanwhile, the CdTe layer, as shown in Figure 4.7 (b), was heavily damaged by ion milling, compared with the HgCdTe layer, because of the greater susceptibility of some II-VI materials to ion-milling damage even when liquid-nitrogen cooling is used during the milling process.<sup>14</sup>

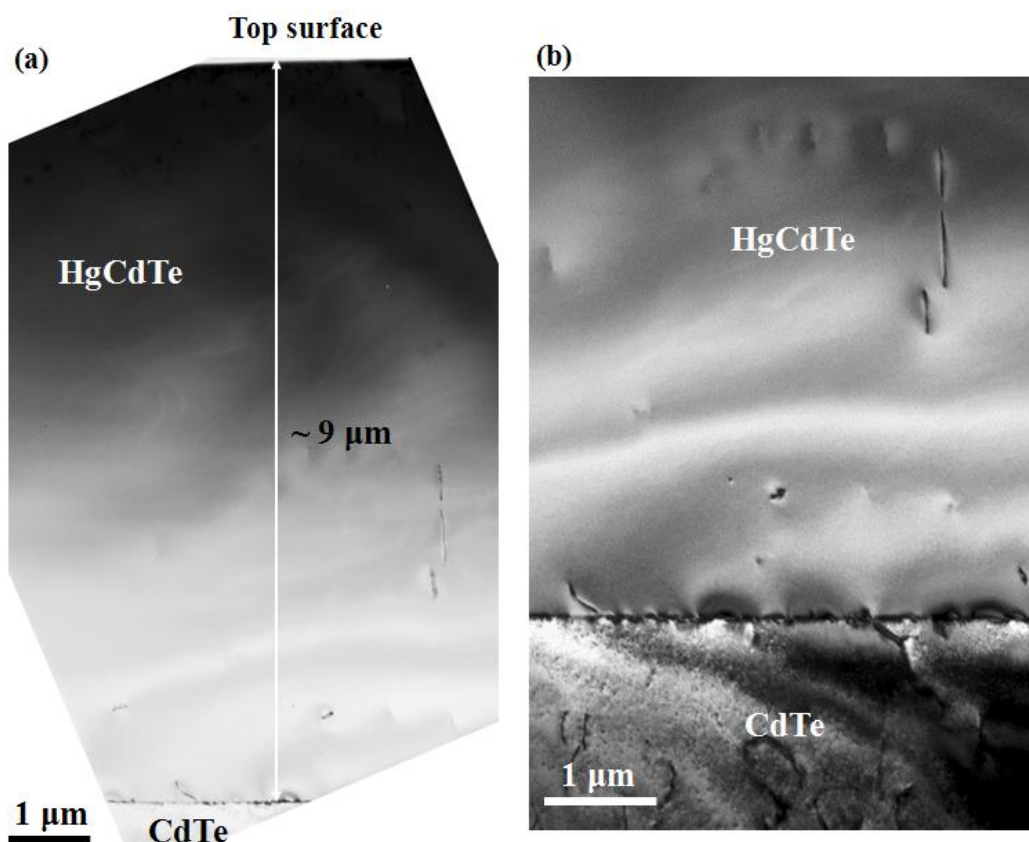


Figure 4.7 Cross-sectional electron micrographs showing: (a) whole HgCdTe layer on CdTe; and (b) HgCdTe/CdTe interface.



Figure 4.8 is a cross-sectional electron micrograph taken near the top surface of the HgCdTe. In general, the bulk HgCdTe material was found to be of high quality, whereas the region near the top surface, which corresponds to material with a slightly different composition, was observed to be quite defective.

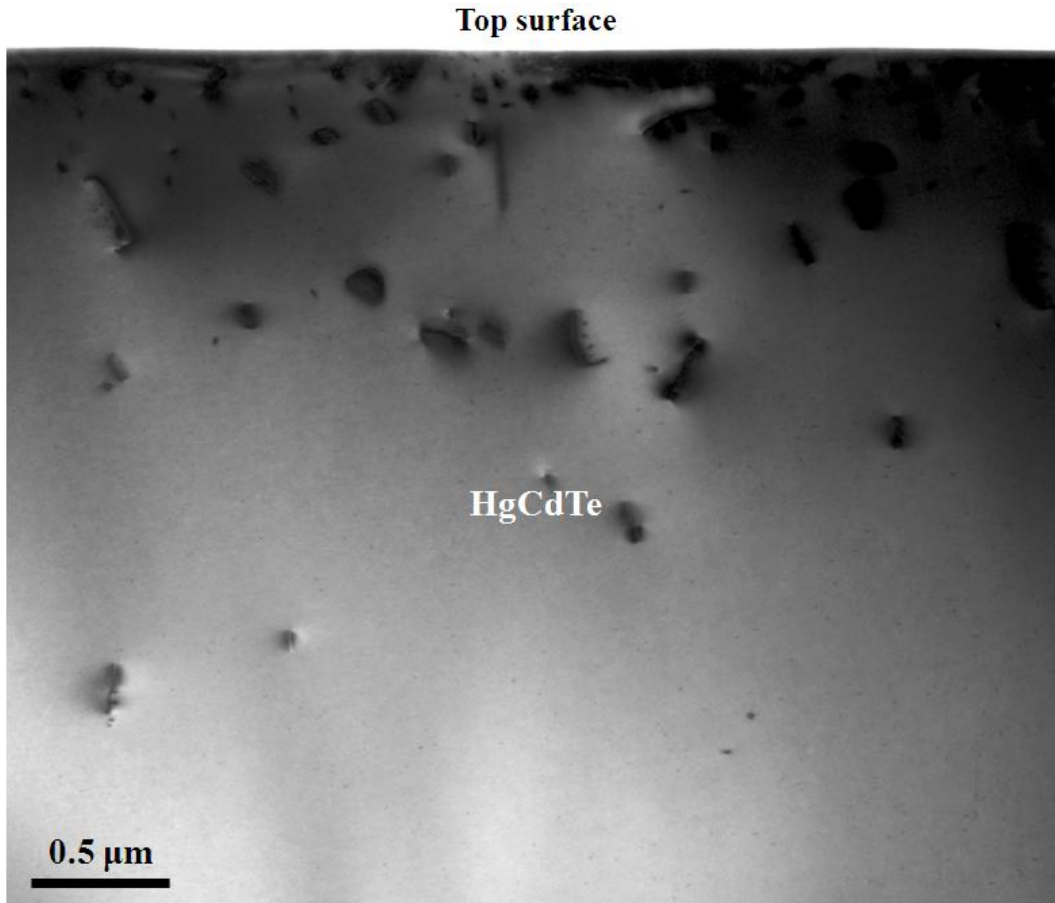


Figure 4.8 Cross-sectional electron micrograph showing microstructure near the top surface of HgCdTe epilayer grown on CdTe/GaAs(211)B composite substrate.

Figures 4.9 (a) and (b) respectively show cross-sectional electron micrographs demonstrating the high quality of the HgCdTe/CdTe heterostructure without any signs of precipitates at the interface, and an example of a dislocation that originates at the HgCdTe/CdTe interface and terminates during the early stages of HgCdTe growth. With closer observation of these figures, a very thin darker region is visible just above the HgCdTe/CdTe interface.

A cross-sectional electron micrograph taken at higher magnification than Figures 4.9, as shown in Figure 4.10 (a), and an HAADF image shown in Figure 4.10 (b) confirmed that there was a buffer layer of about 30-nm thickness between the HgCdTe and CdTe layers. It seems likely that this buffer layer contains higher Z elements compared with HgCdTe and CdTe because of its darker contrast in the bright-field image and its brighter appearance in the Z-contrast image.

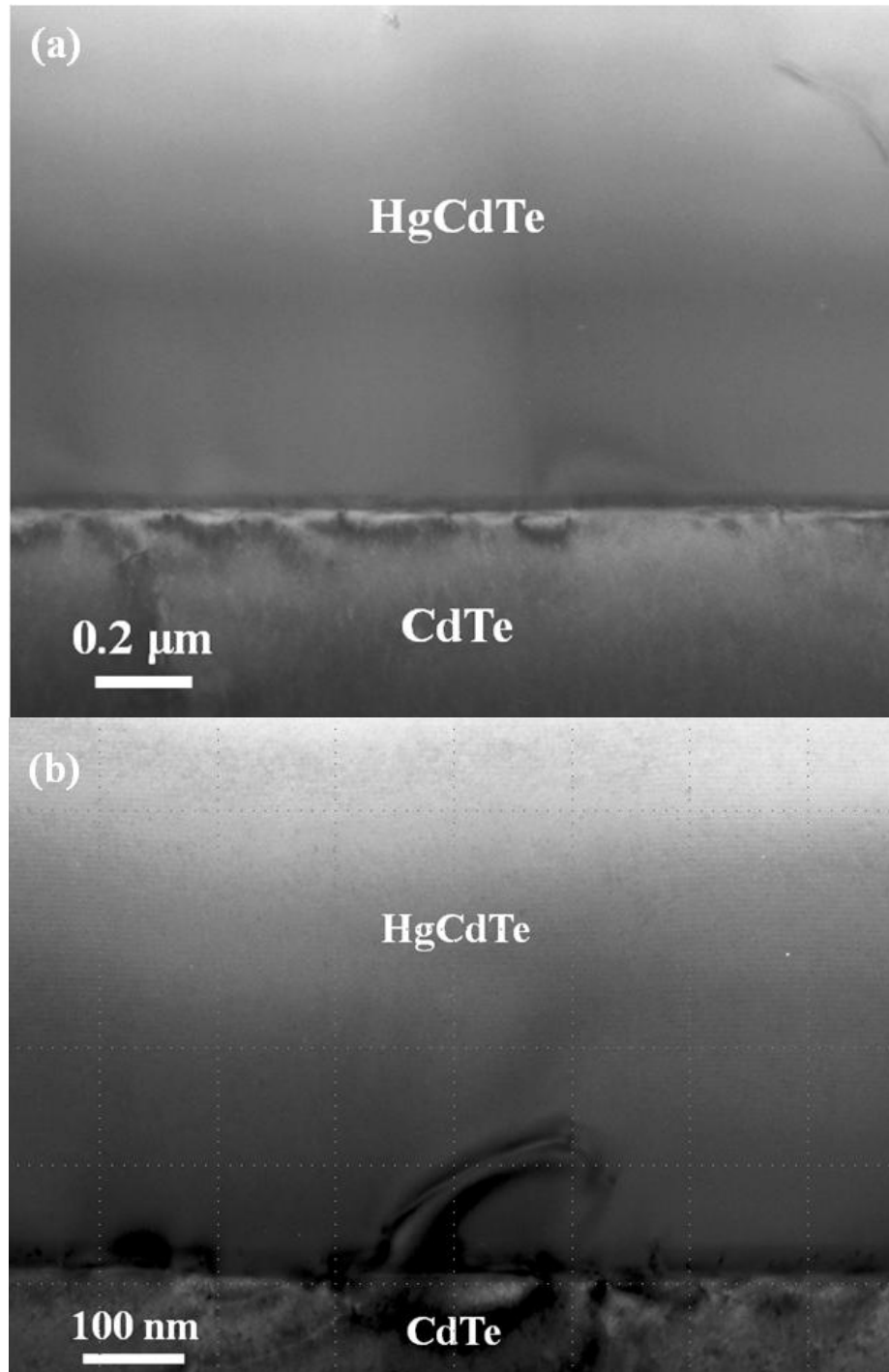


Figure 4.9 Cross-sectional electron micrographs showing HgCdTe/CdTe heterostructure.



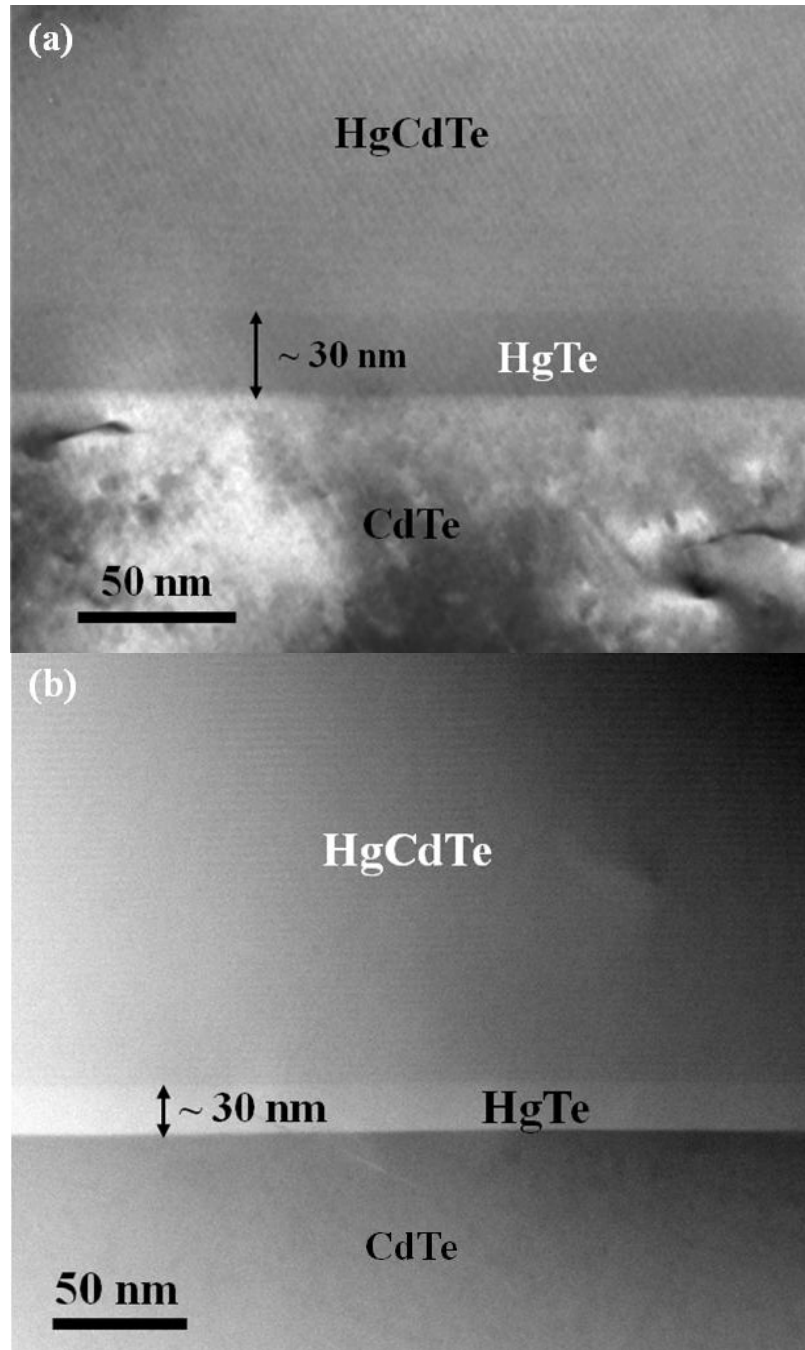
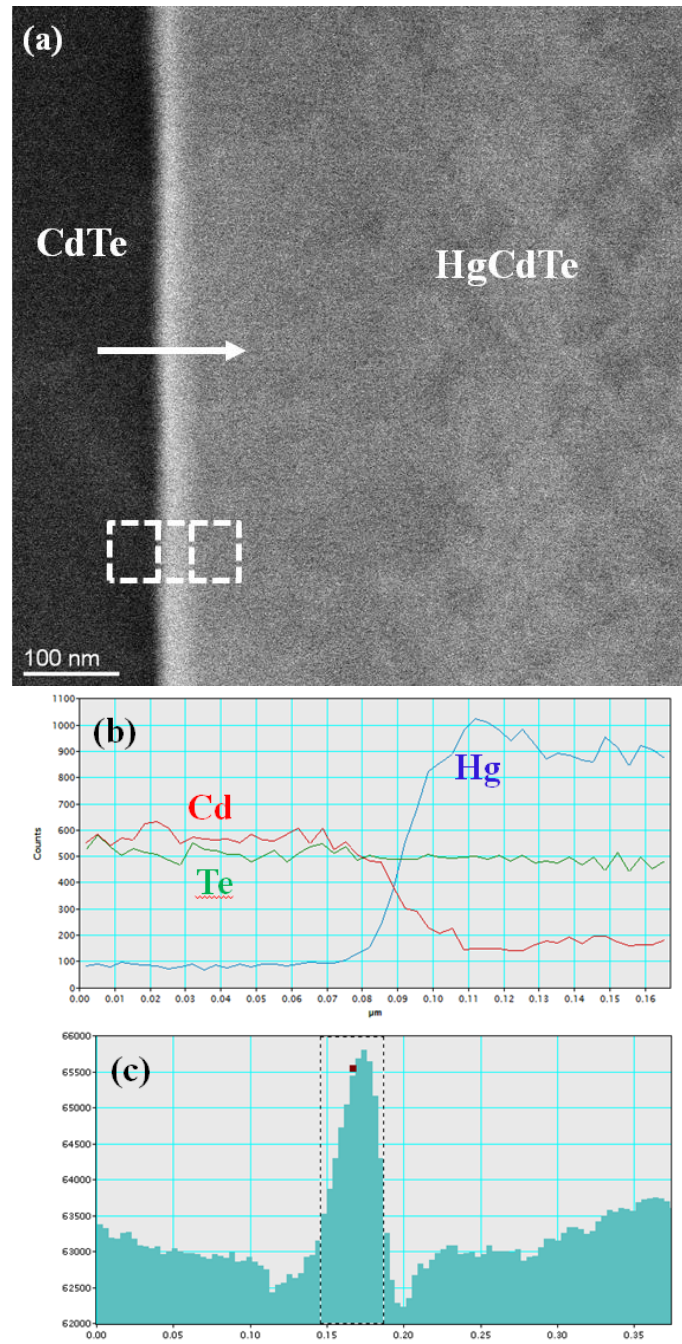


Figure 4.10 Cross-sectional electron micrograph (a) and HAADF image (b), showing thin HgTe buffer layer between HgCdTe and CdTe.

In addition, compositional analysis across the HgCdTe/CdTe interface was used to map out the corresponding elemental profiles, including the HgTe buffer layer. Figure 4.11 (a) is an HAADF image showing the region used for the EDXS analysis and intensity profile. The HgTe buffer layer between HgCdTe and CdTe shows the brightest contrast because of its higher Hg content, compared with the HgCdTe or CdTe layers. Using the EDXS line scan profile, as shown in Figure 4.11 (b), along the arrowed region indicated in Figure 4.11 (a), an Hg hump just above the CdTe layer is observed. The length of the Hg hump region is about 30 nm. The intensity profile in Figure 4.11 (c), along the box indicated in Figure 4.11(a), also shows that there is higher intensity region of about 30 nm in length. These results confirm that there is a thin HgTe buffer layer of about 30 nm between HgCdTe and CdTe. It is assumed that this HgTe buffer layer between HgCdTe and CdTe is intended to assist in achieving in higher quality MBE-grown HgCdTe.



Figures 4.11 (a) HAADF image showing region used for EDXS analysis; (b) elemental profile along line indicated in (a); (c) intensity profile along the box indicated in (a).

#### 4.4 Conclusions

In summary, samples of HgCdTe/CdTe/GaAs(211)B and CdTe/GaAs(211)B were grown using MBE, and their microstructure was investigated using a wide range of TEM imaging and analytical techniques. High quality MBE-grown CdTe on GaAs(211)B substrate is demonstrated as a viable composite substrate platform for HgCdTe growth. Analysis of interfacial misfit dislocations and residual strain estimation show that although most of the elastic strain at the CdTe/GaAs interface is relaxed, a pit region near a GaAs surface still contains significant strain. TEM examination also revealed a thin HgTe buffer layer between HgCdTe and CdTe, which is presumed to assist in achieving higher quality material for MBE-grown HgCdTe using the CdTe/GaAs(211)B composite substrates.

## REFERENCES

- <sup>1</sup> J. J. Kim, R. N. Jacobs, L. A. Almeida, M. Jaime-Vasquez, C. Nozaki, J. K. Markunas, J. D. Benson, and D. J. Smith, J. Electron. Mater. (2012). *submitted*.
- <sup>2</sup> R. Sporken, S. Sivananthan, K. K. Mahavadi, G. Monfroy, M. Boukerche, and J.P. Faurie, Appl. Phys. Lett. 55, 1879(1989).
- <sup>3</sup> N. K. Dhar, P. R. Boyd, M. Martinka, J. H. Dinan, L. A. Almeida, and N. Goldsman, J. Electron. Mater. 29, 748(2000).
- <sup>4</sup> M. Carmody, J.G. Pasko, D. Edwall, R. Bailey, J. Arias, M. Groenert, L.A. Almeida, J. H. Dinan, Y. Chen, G. Brill, and N. K. Dhar, J. Electron. Mater. 35, 1417 (2006).
- <sup>5</sup> L. A. Almeida, L. Hirsch, M. Martinka, P. R. Boyd, and J. H. Dinan, J. Electron. Mater. 30, 608 (2001).
- <sup>6</sup> J. D. Benson, R.N. Jacobs, J. K. Markunas, M. Jaime-Vasquez, P. J. Smith, L. A. Almeida, M. Martinka, M. F. Vilela, and U. Lee, J. Electron. Mater. 37, 1231 (2008).
- <sup>7</sup> J. P. Zanatta, G. Badano, P. Ballet, C. Langeron, J. Baylet, O. Gravrand, J. Rothman, P. Castelein, J. P. Chamonal, A. Million, G. Destefanis, S. Mibord, E. Brochier, and P. Costa, J. Electron. Mater. 35, 1231 (2006).
- <sup>8</sup> M. Krishnamurthy, P. M. Petroff, and J. M. Arias, Appl. Phys. Lett. 73, 7952 (1993).

- <sup>9</sup> T. J. de Lyon, R. D. Rajavel, B. Z. Nosho, S. Terterian, M. L. Beliciu, P. R. Patterson, D. T. Chang, M. F. Boag-O'Brien, B. T. Holden, R. N. Jacobs, and J. D. Benson, *J. Electron. Mater.* 39, 1058 (2010).
- <sup>10</sup> G. Brill, Y. Chen, P. Wijewarnasuriya, and N. Dhar, *Proc. SPIE* 7419 74190L-1 (2009).
- <sup>11</sup> R. N. Jacobs, J. Markunas, J. Pellegrino, L. A. Almeida, M. Groenert, M. Jaime-Vasquez, N. Mahadik, C. Andrews, and S. B. Qadri, *J. Cryst. Growth* 310, 2960 (2008).
- <sup>12</sup> M. Jaime-Vasquez, M. Martinka, A. J. Stoltz, R. N. Jacobs, J. D. Benson, L. A. Almeida, and J. K. Markunas, *J. Electron. Mater.* 37, 1247 (2008).
- <sup>13</sup> P. Abbott, L. Pillans, P. Knowles, R. K. McEwen, *Infrared Technology and Applications XXXVI*, *Proc. SPIE* 7660, 766035 (2010).
- <sup>14</sup> C. Wang, D. J. Smith, S. Tobin, T. Parodos, J. Zhao, Y. Chang, and S. Sivananthan, *J. Vac. Sci. Technol. A* 24, 995 (2006).
- <sup>15</sup> M. Jaime-Vasquez, M. Martinka, R. N. Jacobs, and M. Groenert, *J. Electron. Mater.* 35, 1455 (2006).
- <sup>16</sup> S. Bauer, A. Rosenauer, J. Skorsetz, W. Kuhn, H. P. Wagner, J. Zweck, and W. Gebhardt, *J. Cryst. Growth* 117, 297 (1992).
- <sup>17</sup> J. W. Matthews, *J. Vac. Sci. Technol.* 12, 126 (1975).
- <sup>18</sup> A. F. Schwartzman and R. Sinclair, *J. Electron. Mater.* 20, 805 (1991).

- <sup>19</sup> X. J. Wang, Y. Chang, C. R. Becker, C. H. Grein, S. Sivananthan, and R. Kodama, J. Electron. Mater. 40, 1860 (2011)
- <sup>20</sup> W. F. Zhao, R. N. Jacobs, M. Jaime-Vasquez, L. O. Bubulac and D. J. Smith, J. Electron. Mater. 40, 1733 (2011).

## Chapter 5

CRITICAL THICKNESS OF ZnTe/GaSb(211)B  
GROWN BY MOLECULAR BEAM EPITAXY

This chapter describes the microstructural study of a set of ZnTe samples grown on GaSb(211)B substrates as part of an investigation into critical thickness for defect formation. My role has been the microstructural characterization using electron microscopy. This research was carried out in collaboration with Professor Tom Myers and colleagues from Texas State University-San Marcos who were responsible for sample growth. Results from this study have recently been published and submitted for publication.<sup>1,2</sup>

## 5.1 Introduction

ZnTe is a direct-band semiconductor with a band gap of 2.26 eV (529nm) at room temperature, and it is a material of much current interest for various optoelectronic devices such as pure-green light-emitting diodes, green laser diodes, and UV-green photodetectors.<sup>3,4</sup> ZnTe is also considered as a possible buffer layer for growth of HgCdTe or HgCdSe.<sup>5</sup> Various substrates such as Si, InP, InAs, GaAs, and GaSb have been used for the growth of ZnTe.<sup>5-7</sup> It has been reported that thick ( $\sim 2.5 \mu\text{m}$ ) films of ZnTe grown on GaSb(100) substrates have better crystal quality compared with ZnTe grown on other substrates (Si, InP, InAs, and GaAs), and also have the highest photoluminescence intensity.<sup>6</sup>



Moreover, the ZnTe/GaSb heterostructure itself is of potential interest for cascade solar cells.<sup>6</sup> Thus, different approaches geared towards optimizing the epitaxial growth of high quality ZnTe/GaSb are under active investigation.

The critical thickness ( $h_c$ ) for defect formation in heteroepitaxial systems is an important parameter that must be taken into account when designing device structures. Below  $h_c$ , the epitaxial layer grows pseudomorphic to the substrate without any misfit dislocations. Above  $h_c$ , misfit dislocations and threading segments are formed to relieve strain and the epilayer assumes close to its bulk lattice parameter. In the specific case of ZnTe layers deposited on GaSb(100) substrates using organic-metallic vapor phase epitaxy, upper limits for  $h_c$  of either 180 nm or 800 nm have previously been derived based on optical and x-ray diffraction measurements.<sup>8,9</sup> However, there is no information yet available about the critical thickness of ZnTe/GaSb grown by MBE in the (211) orientation. The (211)B orientation is of particular interest for the subsequent growth of HgCdTe because the stepped (211) surface, which is composed of (111) terraces and (100) edges, allows a step-flow growth mechanism that leads to reduced twinning and antiphase domain formation compared with the (100) orientation.<sup>10</sup> The (211)B orientation is also of interest because the ZnTe/GaSb system is considered as a possible composite substrate for MBE-grown HgCdSe for infrared detector applications.<sup>11</sup> In this present study, a set of ZnTe layers grown on GaSb(211)B substrates has been investigated using HRXRD measurements and TEM

characterization. A wide range of TEM imaging and analytical techniques, including high-resolution electron microscopy (HREM), high-angle annular-dark-field (HAADF) imaging, and energy-dispersive X-ray spectroscopy (EDXS) were used.

## 5.2 Experimental details

The ZnTe layers were deposited on GaSb(211)B substrates using a DCA MBE system after removal of the surface oxides from the GaSb wafer by exposure to atomic hydrogen for 20 min at 400 °C. Migration-enhanced epitaxy was employed to nucleate the ZnTe epilayers. With the substrate temperature at 320 °C, the surface was exposed to Zn for 60 s followed by a sequence of ten periods of alternating exposures of Zn and Te simultaneously for 5 s and followed by Zn exposure for 60 s. The purpose of the initial Zn pre-exposure was to minimize the possible formation of any  $\text{Ga}_2\text{Te}_3$  phase at the GaSb and ZnTe interface.<sup>14</sup> The alternating sequence of Zn with Te and Zn only was chosen because a similar sequence was shown previously to result in high-quality ZnSe on GaAs(100).<sup>15</sup>

The ZnTe layers were subsequently deposited to thicknesses in the range from 50 nm to 2,000 nm by conventional MBE where both the Zn and Te shutters were simultaneously opened for the remaining growth time. HRXRD measurements were made using a Bede D1 system under the triple-crystal

configuration and Cu  $K_{\alpha 1}$  x-ray line with wavelength of 1.54056 Å. There is an instrumental broadening of  $\sim 18$  arcsec in the XRD system. All HRXRD measurements were performed with the sample at room temperature. Bede RADS software was used to simulate the HRXRD data. In the HRXRD measurements, the full-width at half maximum (FWHM) of 422 reflections from ZnTe as well as the separation between ZnTe and GaSb peaks were analyzed to yield an estimated value for  $h_c$ .

Samples suitable for TEM observation were prepared in the cross-sectional geometry using standard mechanical polishing and dimpling to thicknesses of about 10  $\mu\text{m}$ , followed by argon-ion-milling at liquid nitrogen temperature to minimize any ion-milling-induced artefacts.<sup>12</sup> Low-angle, low-voltage (approximately 1.8 keV) milling was used for final thinning to minimize the formation of any amorphous surface or interfacial layers. The electron microscopy observations were mostly carried out using a JEOL JEM-4000EX high-resolution electron microscope (HREM), operated at 400keV and equipped with a double-tilt, top-entry-type specimen holder. HAADF or “Z-contrast” imaging and EDXS analysis were carried out using a JEO-2010F, equipped with a field-emission electron gun and operated at 200keV. Samples were usually oriented along the common  $\langle 110 \rangle$  projection for TEM observation.

### 5.3 Results and discussion

#### 5.3.1 Calculation of theoretical thickness

Several authors have developed models to estimate the critical thickness in heteroepitaxial systems. The model of Matthews–Blakeslee has been applied extensively to mismatched systems.<sup>13-15</sup> It assumes that there are pre-existing threading dislocations from the substrate which can elongate to form misfit dislocations in the epilayer. The force balance model then assumes that the critical thickness occurs when the misfit strain force (which elongates the threading dislocation) matches the tension force (which opposes the elongation) found in a pre-existing line dislocation. Above the critical thickness, the force of the misfit strain exceeds that of the tension force, destroying the coherency that previously existed at the interface and creating additional dislocations. In this model, the critical thickness is given by

$$h_c = \frac{b(1-\nu\cos^2\alpha)}{8\pi f_m \nu \cos\beta} \left[ \ln\left(\frac{h_c}{b}\right) + 1 \right], \quad (1)$$

$$b = \frac{1}{2} a_l < 110 >, \quad (2)$$

$$f_m = \frac{a_l - a_s}{a_s}, \quad (3)$$

where  $h_c$  is the critical thickness (Å),  $\mathbf{b}$  is the Burgers vector (Eq. 2),  $\nu$  is the Poisson's ratio,  $\alpha$  and  $\beta$  are the angles between the dislocation line and the Burgers vector,  $f_m$  is the misfit parameter (Eq. 3),  $a_l$  is the epilayer lattice parameter, and  $a_s$  is the substrate lattice parameter. Assuming that the misfit

dislocations are of the  $60^\circ$  type ( $\alpha = \beta = 60^\circ$ ), and taking lattice parameters  $a_{\text{ZnTe}} = 6.1039\text{\AA}$  and  $a_{\text{GaSb}} = 6.0959\text{\AA}$ ,<sup>8</sup> then the value of critical thickness is calculated to be 115 nm.

A simpler model was chosen by Cohen-Solal et al.,<sup>16</sup> with the misfit at the heteroepitaxial interface being accommodated by a combination of misfit strain and misfit dislocations. The energy can be calculated using Keating's valence force approximation to yield the following semi-empirical expression:<sup>16,17</sup>

$$h_c = A^* f_m^{-3/2} \quad (4)$$

where  $A^*$  is an adjustable parameter. It was determined that  $A^*$  would be approximately 0.15 for zincblende semiconductor systems with misfit of less than 8%. Since the ZnTe/GaSb system has a misfit of only 0.13%, then  $A^*$  is taken to have the value of 0.15, and substitution into Eq. 4 then yields a value of  $h_c = 316$  nm.

Instead of energy-minimization arguments, an alternative geometrical model has also been proposed to estimate the critical thickness.<sup>18</sup> It was assumed that a misfit dislocation will not form if the strain is less than  $\mathbf{b}/md$ , where  $\mathbf{b}$  is the Burgers vector,  $d$  is the film thickness, and  $m$  is between 1 and 2. In this model, the critical thickness is given by the expression

$$h_c = \frac{b}{f_m} \quad (5)$$

which would yield a value of 329 nm for the ZnTe/GaSb system.

### 5.3.2 Critical thickness determination using HRXRD

Figure 5.1 shows HRXRD spectra for four ZnTe layers grown on GaSb(211)B substrates, with thicknesses ranging from 100 nm to 2100 nm.<sup>1</sup> The peaks of highest intensity at 0 arcsec are from the GaSb substrates, and the peaks adjacent to the GaSb peak are from the ZnTe layers. As the thickness of the ZnTe layer increases, the intensity of the ZnTe peak increases. For ZnTe layer thicknesses of 100 nm and 350 nm, thickness fringes are clearly visible, indicating that the overall crystal quality of the layers is excellent. For those ZnTe layers thicker than 350 nm, the thickness fringes disappear, indicating that the crystal quality has decreased. Simulations performed on these spectra gave a best fit when the target thickness for the MBE deposition was used as a parameter.

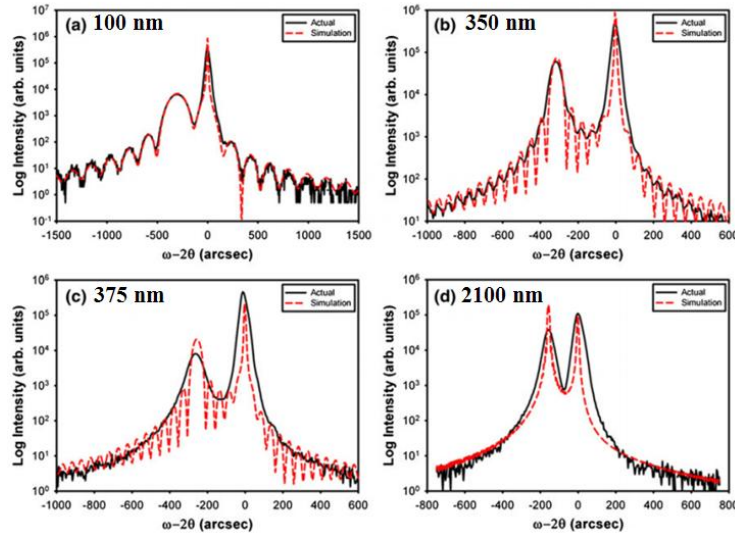


Fig. 5.1 HRXRD  $\omega$ - $2\theta$  measurements of ZnTe grown for (a) 100 nm, (b) 350 nm, (c) 375 nm, and (d) 2100 nm.<sup>1</sup>

Figure 5.2 plots FWHM values of ZnTe(422) peaks as a function of the ZnTe layer thickness. For thicknesses below 350 nm, there is a clear log–log relationship between FWHM values and the layer thickness as shown in the inset. This trend is consistent with a finite thickness analysis of pseudomorphic layers which yields a log to negative log relationship between FWHM value and layer thickness.<sup>19</sup> For thicknesses between 350 nm and 375 nm, the FWHM value increases abruptly from 57.7 arcsec to 71.7 arcsec. This change coincides with the disappearance of the HRXRD fringes from the spectra shown in Figure 5.1. From this abrupt change, it is concluded that the critical thickness value is between 350 nm and 375 nm. For thicknesses above 375 nm, the FWHM starts to decrease again but with reduced thickness dependence, with the lowest FWHM for the thickest layer measured being 43.6 arcsec.

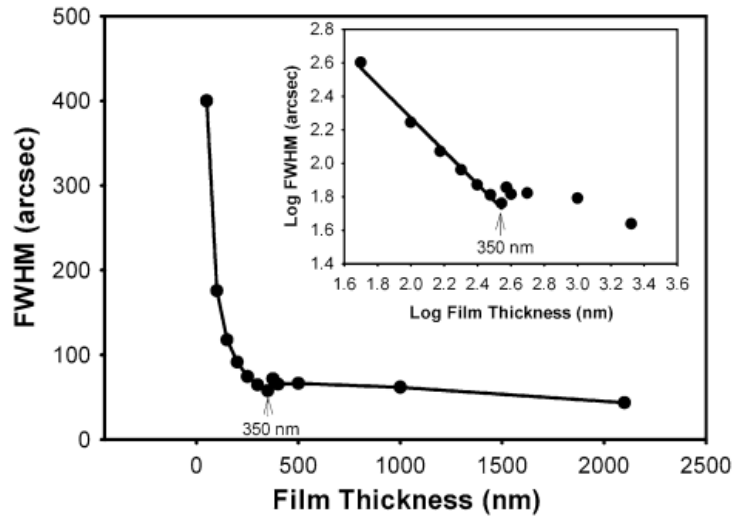


Fig. 5.2 FWHM of the  $\omega$ -2 $\theta$  ZnTe(422) peak at different thicknesses. Inset shows the same plot on a log–log scale.<sup>1</sup>

An independent estimate of  $h_c$  can be obtained by measuring the strain in the epilayer. Below the critical thickness, the layer is pseudomorphic to the substrate and the strain should be maximum. Above the critical thickness, the layer relaxes, and the strain is expected to decrease. The amount of out-of-plane strain is reflected in the separation between the epilayer and substrate peaks in the HRXRD spectrum. Figure 5.3 plots the separation between ZnTe and GaSb peaks as a function of layer thickness. With the exception of the 50-nm layer, the separation is at a maximum and fairly constant for layers with thicknesses below 350 nm. For thicknesses above 350 nm, the separation decreases rapidly, reaching a value of 170 arcsec at 2100 nm. These HRXRD results also suggest that the critical thickness of ZnTe on GaSb(211)B substrates is between 350 nm and 375 nm.

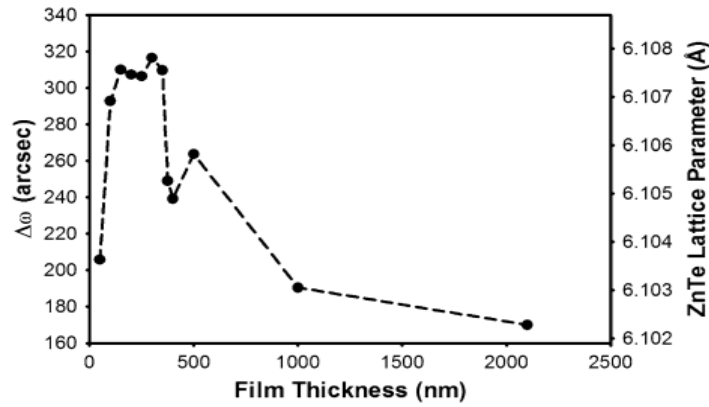


Fig. 5.3 Peak separation ( $\Delta\omega$ ) between ZnTe(422) and GaSb(422)  $\omega$ - $2\theta$  HRXRD peaks and the measured out-of-plane lattice parameter for ZnTe films of different epilayer thicknesses.<sup>1</sup>



### 5.3.3 TEM characterization

Low-magnification cross-sectional electron micrographs for the 350-nm-thick ZnTe layer grown on a GaSb(211)B substrate reveal very high quality ZnTe epilayers with very low density of interfacial defects, as shown in Figure 5.4. The interface is overall highly coherent, and very little strain-related contrast is visible away from the interface. The lateral separation between these interfacial defects is typically greater than 300 nm, being in agreement with the ideal value of dislocation separation ( $\sim 330$  nm) between ZnTe and GaSb based on the room temperature lattice parameters. This morphology is attributed to the very small lattice mismatch ( $-0.13\%$ ) between these two materials.

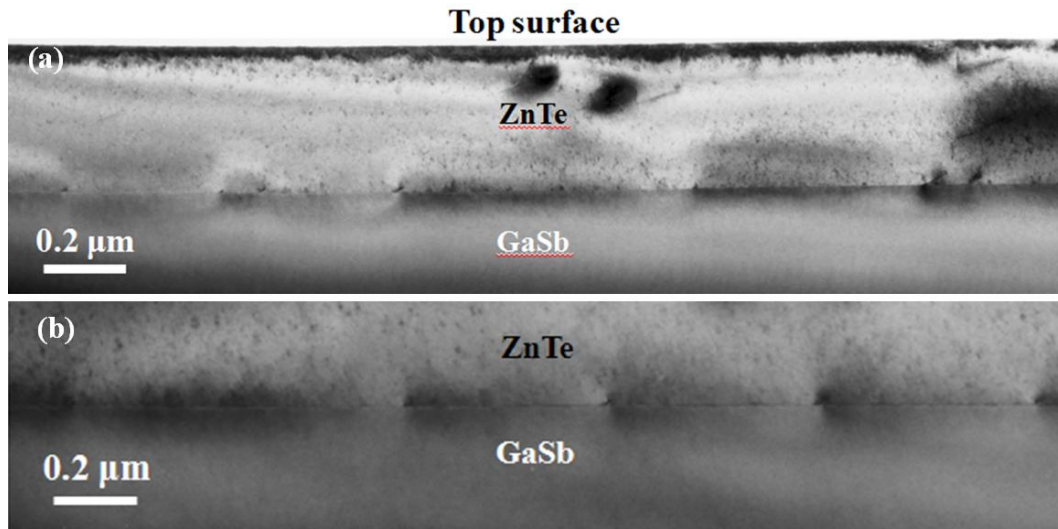


Figure 5.4 Low magnification cross-sectional TEM images, (a) and (b), showing highly-separately misfit dislocations at ZnTe/GaSb interface.

Figure 5.5 (a) shows a HREM image for the 350-nm-thick ZnTe layer grown on GaSb(211)B substrate. The exact position of the interface is extremely difficult to pinpoint in HREM images, due to the closely similar average atomic numbers of the two materials. The ZnTe/GaSb interface in this region is highly coherent consistent with the stepped nature of the (211) orientation. In addition, there is no rotational angle between ZnTe epilayer and GaSb substrates because the  $\{111\}$  planes continue along straight lines across the interface. It is demonstrated that there are no misfit dislocations at the interface region shown in Figure 5.5(a) by using the fast Fourier transform (FFT) technique in Figure 5.5(b).<sup>20</sup>

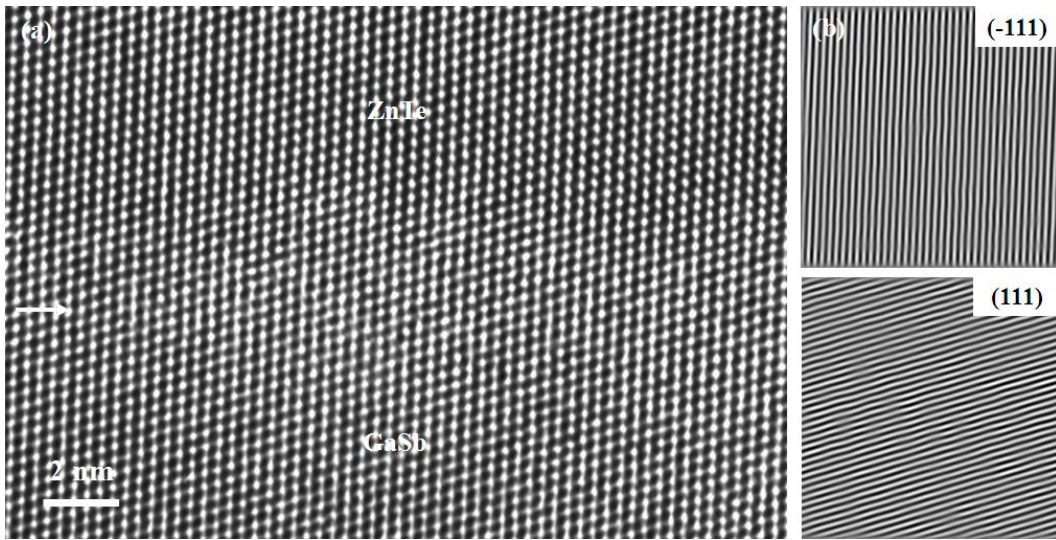


Figure 5.5 (a) HREM image establishing the highly coherent nature of the ZnTe/GaSb interface (arrowed); (b) inverse FFT images obtained by selecting pairs of  $\{111\}$  diffraction spots.

Likewise, it is very difficult to determine the position of the interface (arrowed) in the Z-contrast image shown in Figure 5.6 (a) because of the closely similar average atomic numbers of ZnTe and GaSb. A distinct feature visible near the interface in lower magnification images was typically used as a reference to track the exact location of the interface at higher magnification. Individual EDXS spectra taken from the ZnTe epilayer and the GaSb substrates, as shown in Figure 5.6(b), confirm that these regions are ZnTe epilayer and GaSb substrates, respectively.

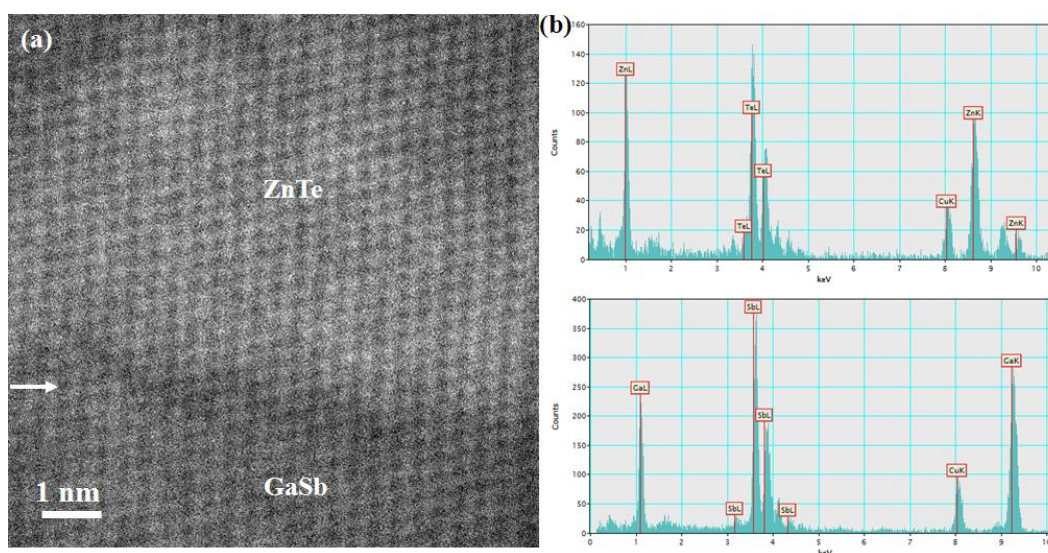


Figure 5.6 (a) HAADF image showing the region used EDXS analysis, and (b) individual EDXS spectra taken from the ZnTe epilayer and GaSb substrate, respectively.

Figure 5.7 (a) and (b) show low-magnification cross-sectional electron micrographs for 375-nm-thick and 400-nm-thick ZnTe layers on GaSb(211)B substrates, respectively. The thicknesses of these ZnTe epilayers were targeted to be 375 nm and 400 nm during MBE growth, but they were actually 380 nm and 410 nm, respectively, based on the magnification of the TEM images. These two layers are just above the critical thickness estimated by HRXRD measurement. Threading dislocations are generated from the interface: some terminate near the interface, while some reach as far as the top surface. These TEM results thus confirm that threading dislocations are indeed generated across the interface for samples just above the critical thickness to relieve the strain caused by lattice mismatch between ZnTe and GaSb.

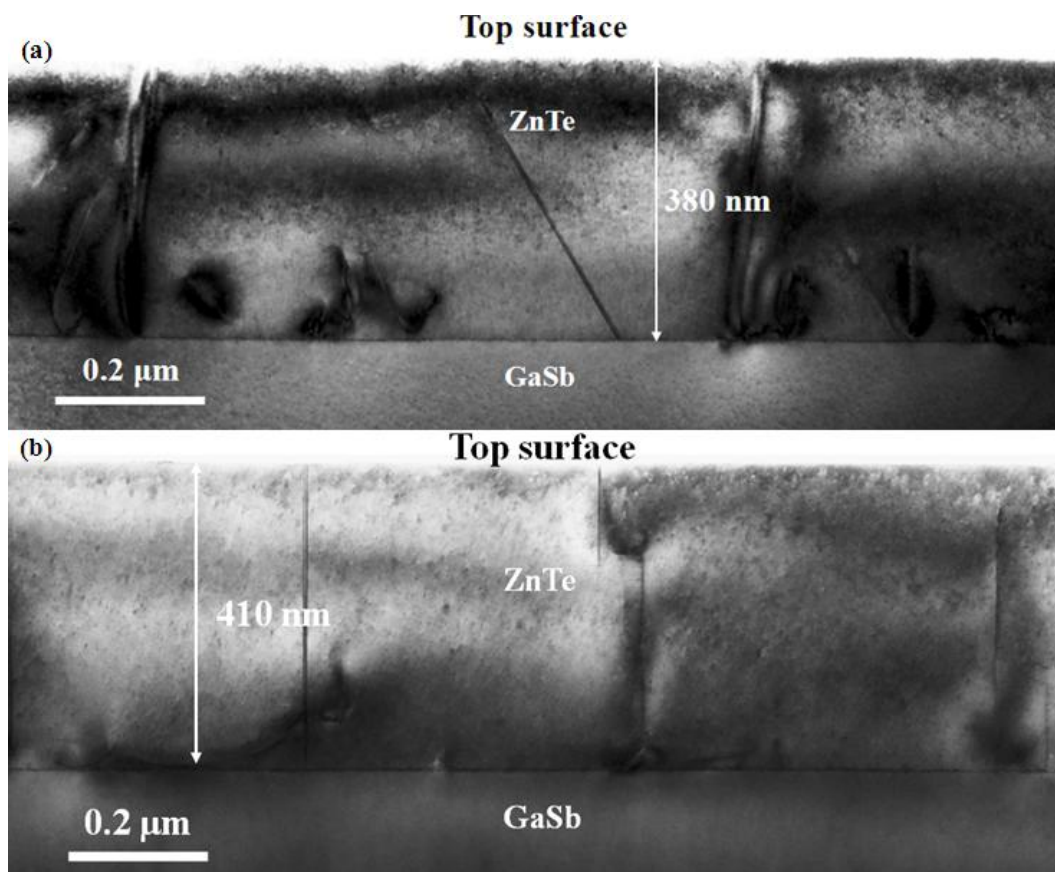


Figure 5.7 Low magnification cross-sectional TEM images for (a) 375 nm and (b) 400 nm ZnTe epilayers on GaSb substrates, respectively. Arrows indicates the thickness of ZnTe layer.

Low-magnification cross-sectional electron micrographs for 500 nm and 1,000 nm ZnTe layers grown on GaSb(211)B substrates are shown in Figures 5.8 (a) and (b), respectively. The high density of lattice defects does not decrease until about 400 nm along the growth direction, as shown in Figure 5.8 (a), and many threading dislocations are generated from regions of both interfaces shown

in Figures 5.8 (a) and (b), helping to reduce the strain across the interfaces caused by lattice mismatch. It seems clear that these films have much higher defect density than the 375 nm and 400 nm thick ZnTe layers.

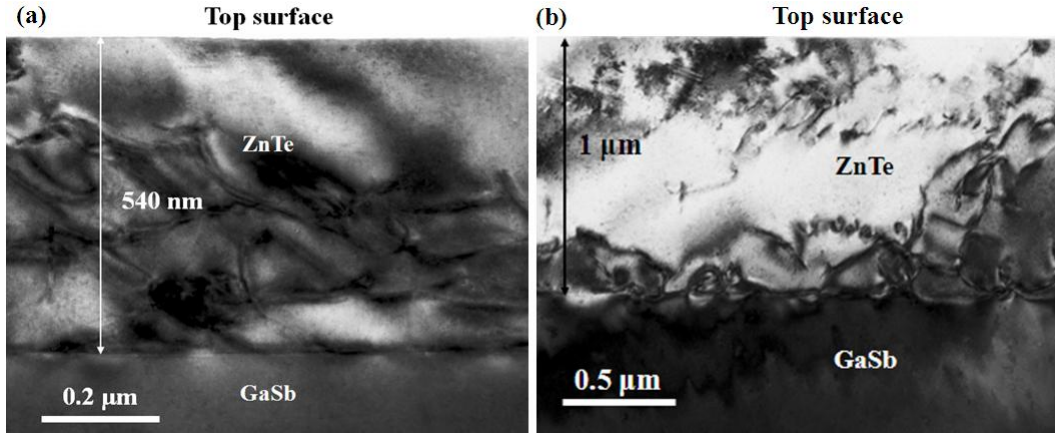


Fig. 5.8 Low magnification cross-sectional TEM images for (a) 500 nm and (b) 1,000 nm ZnTe epilayers on GaSb substrates, respectively.

#### 5. 4 Conclusions

During this study, the critical thickness of MBE-grown ZnTe on GaSb(211)B substrates has been investigated, using HRXRD as well as TEM. An analysis of HRXRD spectra for ZnTe/GaSb(211)B epilayers of different thickness gives  $h_c$  values between 350 nm and 375 nm, based either on FWHM values for the ZnTe epilayers or the separation of ZnTe and GaSb diffraction peaks. The  $h_c$  value is in good agreement with theoretical predictions of 316 nm and 329 nm, using Cohen-Solal and Dunstan models, respectively. Moreover, the TEM results



confirm that the ZnTe layers with thicknesses of 350 nm have highly coherent interfaces and very low densities of dislocations, unlike samples having the thicker ZnTe layers.

## REFERENCES

- <sup>1</sup> J. Chai, O. C. Noriega, J. H. Dinan, and T. H. Myers, J. Electron. Mater. 41, 3001(2012)
- <sup>2</sup> J. Chai, O.C. Noriega, J. H. Dinan, J. J. Kim, D. J. Smith, and T. H. Myers, J. Electron. Mater. (2012), submitted.
- <sup>3</sup> Y.-H. Zhang, S.-Q. Yu, S.R. Johnson, D. Ding, S.-N. Wu, in: Proceedings of the 33rd IEEE Photovoltaic, Energy Specialist Conference, 2008, p. 20.
- <sup>4</sup> S. Wang, S.-N. Wu, D. Ding, X. Liu, X.-B. Zhang, D.J. Smith, S.-Q. Yu, S.R. Johnson, J.K. Furdyna, Y.-H. Zhang, J. Cryst. Growth 311 (2009) 2116.
- <sup>5</sup> Y. Chen, S. Simingalam, G. Brill, P. Wijewarnasuriya, N. Dhar, J. J. Kim and D. J. Smith, J. Electron. Mater. 41, 10(2012).
- <sup>6</sup> J. Fan, L. Ouyang, X. Liu, D. Ding, J. K. Furdyna, D. J. Smith, and Y. Zhang, J. Cryst. Growth 323, 127 (2011).
- <sup>7</sup> N. Dhar, P. Boyd, M. Martinka, J. Dinan, L. Almeida, and N. Goldsman, J. Electron. Mater. 29, 748 (2000).
- <sup>8</sup> P. Tomasini, A. Haidoux, J. Domagala, J. Tedenac, M. Maurin, and B. Ducourant, J. Cryst. Growth 165, 203 (1996).
- <sup>9</sup> H. Leiderer, G. Jahn, M. Silberbauer, W. Kuhn, H. Wagner, W. Limmer, and W. Gebhardt, J. Appl. Phys. 70, 398 (1991).
- <sup>10</sup> M. Jaime-Vasquez, M. Martinka, R. N. Jacobs, and M. Groenert, J. Electron. Mater. 35, 1455 (2006).



- <sup>11</sup> W. F. Zhao, G. Brill, Y. Chen, and D. Smith, *J. Electron. Mater.* 41, 2852(2012)
- <sup>12</sup> C. Wang, D. J. Smith, S. Tobin, T. Parodos, J. Zhao, Y. Chang and S. Sivananthan, *J. Vac. Sci. Technol. A* 24, 995 (2006).
- <sup>13</sup> J. Matthews and A. Blakeslee, *J. Cryst. Growth* 27, 118 (1974).
- <sup>14</sup> E. Fitzgerald, *Mater. Sci. Rep.* 7, 91 (1991).
- <sup>15</sup> X. Liu, A. Hopgood, B. Usher, H. Wang, and N. Braithwaite, *Semicond. Sci. Technol.* 14, 1154 (1999).
- <sup>16</sup> G. Cohen-Solal, F. Bailly, and M. Barbe, *J. Cryst. Growth* 138, 68 (1994).
- <sup>17</sup> K. Pinardi, U. Jain, S. Jain, H. Maes, R. Van Overstraeten, and M. Willander, *J. Appl. Phys.* 83, 4724 (1998).
- <sup>18</sup> D. Dunstan, S. Young, and R. Dixon, *J. Appl. Phys.* 70, 3038 (1991).
- <sup>19</sup> X. Zhang, P. Li, D. Parent, G. Zhao, J. Ayers, and F. Jain, *J. Electron. Mater.* 28, 553 (1999).
- <sup>20</sup> S. Bauer, A. Rosenauer, J. Skorsetz, W. Kuhn, H. P. Wagner, J. Zweck, and W. Gebhardt, *J. Cryst. Growth* 117, 297 (1992).

## Chapter 6

## SUMMARY AND FUTURE WORK

## 6.1 Summary

Mercury cadmium telluride ( $\text{HgCdTe}$  or  $\text{Hg}_{1-x}\text{Cd}_x\text{Te}$ ) has been the dominant material for infrared sensing and imaging for several decades. In this dissertation, a wide range of transmission electron microscopy (TEM) imaging and analytical techniques has been used to characterize epitaxial  $\text{HgCdTe}$  and related materials and related substrates for third generation IR detectors.

The systematic study of molecular beam epitaxy (MBE) growth for both  $\text{ZnTe}(211)$  on  $\text{Si}(211)$  and  $\text{ZnTe}(100)$  on  $\text{Si}(100)$  demonstrates that these composite substrates should be considered as promising candidates for lattice-matched, large-area, and low-cost composite substrates for growth of II-VI and III-V compound semiconductors with lattice constants near  $6.1 \text{ \AA}$ .<sup>1</sup> The highest crystal quality of  $\text{ZnTe}(211)$  layers on  $\text{Si}(211)$  substrates was obtained under conditions of nucleation and growth temperatures at  $300^\circ\text{C}$  with a  $\text{Zn/Te}$  flux ratio of 0.5 during the growth of  $\text{ZnTe}(211)$  epilayers, while that of  $\text{ZnTe}(100)$  layers on  $\text{Si}(100)$  substrates was achieved under the conditions of pre-nucleation treatment of Te before the nucleation of  $\text{ZnTe}$  and a  $\text{Zn/Te}$  flux ratio of 2 during growth of the  $\text{ZnTe}(100)$  epilayers. Using these MBE growth conditions, X-ray diffraction (XRD) full-width at half-maxima for  $\text{ZnTe}(211)/\text{Si}(211)$  and

ZnTe(100)/Si(100) were as low as 70 and 100 arcsec, respectively. Moreover, the TEM studies showed that the ZnTe(100)/Si(100) interface was more disordered, compared with the ZnTe(211)/Si(211) interface, and that a small amount of As was present at both interfaces.

Samples of HgCdTe/CdTe/GaAs(211)B and CdTe/GaAs(211)B were grown using MBE, and their microstructure was investigated using a wide range of TEM imaging and analytical techniques.<sup>2</sup> High quality MBE-grown CdTe on GaAs(211)B substrate was demonstrated as a viable composite substrate platform for HgCdTe growth. Analysis of interfacial misfit dislocations and residual strain estimation showed that although most of the elastic strain at the CdTe/GaAs interface was relaxed, a pitted region of the GaAs surface contained significant strain. TEM studies also revealed a thin HgTe buffer layer between HgCdTe and CdTe, which is presumed to assist in achieving higher quality material for MBE-grown HgCdTe using CdTe/GaAs(211)B composite substrates.

The critical thickness ( $h_c$ ) of MBE-grown ZnTe on GaSb(211)B substrates was investigated, using high-resolution X-ray diffraction (HRXRD) as well as TEM.<sup>3</sup> An analysis of HRXRD spectra for ZnTe/GaSb(211)B epilayers of different thickness gave  $h_c$  values between 350 nm and 375 nm, based either on FWHM values for the ZnTe epilayers or the separation of ZnTe and GaSb diffraction peaks. The  $h_c$  value was in good agreement with theoretical predictions of 316 nm and 329 nm, using Cohen-Solal<sup>4</sup> and Dunstan<sup>5</sup> models,

respectively. Moreover, the TEM results confirmed that the ZnTe layers with thickness of 350 nm had a highly coherent interface and very low dislocation densities, unlike samples with thicker ZnTe layers.

## 6.2 Future work

### 6.2.1 Improvement of MBE-grown HgCdTe and substrates

HgCdTe has successfully overcome major challenges from alternative materials such as PbSnTe, type-II superlattices, quantum-well infrared photodetectors, and Hg-based materials for infrared applications over more than a half century. It has also been predicted that HgCdTe technology will continue to expand its range of applications well into the future because of its excellent properties.<sup>6</sup> However, further study on MBE-grown HgCdTe on CdTe/Si, CdTe/GaAs, or other possible composite substrates is still necessary in order to reduce dislocation density, and thereby improve HgCdTe device performance. Samples provided by colleagues at Army Research Laboratory and Night Vision Laboratory are currently undergoing extensive investigation for this purpose.

### 6.2.2 MBE growth of HgCdSe and HgSe as alternatives to HgCdTe

The HgCdSe system is a possible alternative material for IR detector applications. However, the first TEM characterization of HgCdSe epitaxial

material was only recently reported.<sup>7</sup> It is still necessary to establish proper growth conditions for obtaining high-quality HgCdSe on either ZnTe/Si(211) or lattice-matched GaSb(211) substrates. Moreover, although MBE growth of epitaxial HgSe film was reported for the first time in 1993,<sup>8</sup> there has been very little since reported in the literature. Hence, it seems worthwhile to attempt to optimize the MBE growth conditions for HgSe epilayers and study the microstructural characteristics in order to improve overall film quality.

Figure 6.1 shows preliminary TEM observations of HgCdSe and HgSe. For HgCdSe, as shown in Figure 6.1 (a), some regions show good quality material with relatively few dislocations, whereas other regions show {111}-type stacking faults originating at the interface, and sometimes there are very long threading defects, as shown in Figure 6.1 (b). Moreover, what appear to be voids associated with the {111}-type stacking faults are visible at the interface in Figure 6.1 (c). In the case of HgSe, there are many growth defects in the HgSe layer, as shown in Figure 6.1 (d), and it was also found using EDXS line scan profiles that there was a significant amount of Zn in the HgSe layer.

From these preliminary TEM observations, considerable improvement to the growth parameters appears to be necessary before material suitable for detector applications can be produced.

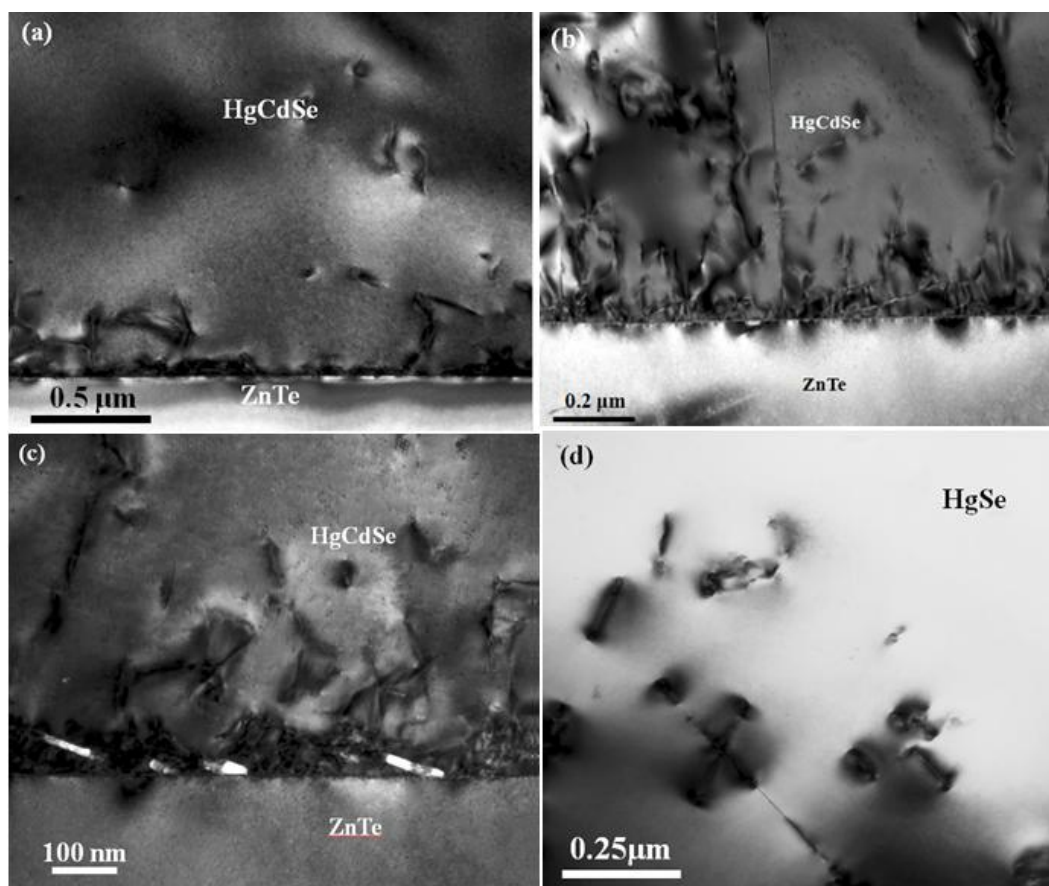


Figure 6.1 Cross-sectional electron micrographs of HgCdSe/ZnTe [(a), (b), and (c)] and HgSe (d).

### 6.2.3 Column-by-column analysis for the ZnTe/Si and ZnTe/GaSb interfaces

Modern transmission electron microscopes, already equipped with energy-dispersive X-ray spectroscopy and/or electron-energy-loss spectroscopy systems, are nowadays being fitted with state-of-the-art aberration correction technology to minimize probe size and maximize spatial resolution of images and spectroscopic

data. Column-by-column structural *and* chemical identification at high spatial resolution should soon become possible using this technology.<sup>9</sup> All atoms located at the interfaces of the IR detector materials, including As in the case of As-passivated Si substrates, could be identified structurally as well as chemically.

## REFERENCES

- <sup>1</sup> Y. Chen, S. Simingalam, G. Brill, P. Wijewarnasuriya, N. Dhar, J. J. Kim, and D. J. Smith, J. Electron. Mater. 41, 10(2012).
- <sup>2</sup> J. J. Kim, R. N. Jacobs, L. A. Almeida, M. Jaime-Vasquez, C. Nozaki, J. K. Markunas, J. D. Benson, and D. J. Smith, J. Electron. Mater. (2012). *submitted*.
- <sup>3</sup> J. Chai, O.C. Noriega, J. H. Dinan, J. J. Kim, D. J. Smith, and T. H. Myers, J. Electron. Mater. (2012), submitted.
- <sup>4</sup> G. Cohen-Solal, F. Bailly, and M. Barbe, J. Cryst. Growth 138, 68 (1994).
- <sup>5</sup> D. Dunstan, S. Young, and R. Dixon, J. Appl. Phys. 70, 3038 (1991).
- <sup>6</sup> A. Rogalski, Rep. Prog. Phys. 68, 2267 (2005).
- <sup>7</sup> W.F. Zhao, G. Brill, Y. Chen, and D. J. Smith, J. Electron. Mater. (2012). (In press)
- <sup>8</sup> Y. Lansari, J. W. Cook and J. F. Schetzina, J. Electron. Mater. 22, 809 (1993).
- <sup>9</sup> O. L. Krivanek, M. F. Chisholm, V. Nicolosi, T. J. Pennycook, G. J. Corbin, N. Dellby, M. F. Murfitt, C. S. Own, Z. S. Szilagy, M. P. Oxley, S. T. Pantelides, and S. J. Pennycook, Nature, 464, 571-571, (2010).